Detectability of transboundary air pollution pathway variations associated with climate change using anthropogenic aerosols

人為起源エアロゾルを用いた気候変動に伴う

越境大気汚染経路変動の検出可能性

February 2025

YING CAI

Graduate School of

Science and Engineering

CHIBA UNIVERSITY

(千葉大学審査学位論文)

Detectability of transboundary air pollution pathway variations associated with climate change using anthropogenic aerosols

人為起源エアロゾルを用いた気候変動に伴う

越境大気汚染経路変動の検出可能性

February 2025

YING CAI

Graduate School of

Science and Engineering

CHIBA UNIVERSITY

Contents

Abstract

There is an urgent need to accurately detect the effects of climate change, which causes a significant threat to human life. As climate change progresses, transboundary air pollution pathways are expected to change globally. However, observational evidence to support this remains limited. In this study, we analyzed long-term satellite observations of aerosols, using anthropogenic aerosols as traces to capture long-term changes in transboundary air pollution pathways associated with climate change. The analysis focused on the Pacific region in the downwind area of China, which is a major source of aerosol emissions. To offset the temporal changes in China's emissions, we proposed a new metric named R_{AOD}, which is defined as the normalization of Aerosol Optical Depth (AOD) data by the AOD over coastal regions of China. Our analysis revealed a clear exponential decrease in R_{AOD} values from China towards the Pacific Ocean. Furthermore, the seasonal variations in atmospheric transport fields are consistent with the slope of R_{AOD}. These findings indicate that it is possible to detect long-term changes in the atmospheric transport fields by utilizing anthropogenic aerosols as tracers. Additionally, we found the eastward transport distance of aerosols has been shortened in recent decades. This trend can be explained by a slight northward shift in transboundary air pollution pathways as climate change progresses. Based on these findings, to enhance the detectability of variations in transboundary air pollution pathways associated with climate change, we proposed the continued use of long-term satellite observations and the R_{AOD} data derived from those observations.

要旨

人類の存続可能性までも脅かしている気候変動の影響の正確な検出が急務となっている。気候変動の進行に伴い越境大気汚染経路が変動すると考えられる。しかしながら、そのことを示す観測的証拠は限られている。本研究では、気候変動に伴う越境大気汚染経路の長期変化を捉えるために、人為起源エアロゾルをトレーサーとみなす斬新な視点で長期のエアロゾル衛星観測データを解析した。解析するにあたり、エアロゾルの大発生源の中国の風下域である太平洋域に着目した。そのうえで、中国からのエミッションの影響を相殺するために、AOD データを中国沿岸域の AOD で規格化した新しいメトリクス（R_{AOD}） を導出した。R_{AOD} の経度分布は東に向かって指数関数的に減少することを明らかにした。また、R_{AOD} の季節変動は大気輸送場の季節変動とよく対応した。これらの結果から、人為起源エアロゾルをトレーサーとみなすことで大気輸送場の変動を検出できることを明らかにした。さらには、中国沿岸域から真東に運ばれる越境大気汚染経路の距離が短くなる長期傾向を見出した。これは気候変動の進行に伴い、越境大気汚染経路が北にわずかにシフトしたことで説明される。気候変動に伴う越境大気汚染経路の変動の検出可能性を高めるために、さらなる継続的な長期のエアロゾル衛星観測とそれに基づいて導出される R_{AOD} の利用を提案した。

Chapter 1. Introduction

Climate change is one of the most significant environmental challenges that profoundly impact on our lives and leads to the severity of abnormal weather events such as heatwaves, droughts, hurricanes, forest fires and floods. According to the Sixth Assessment Report (AR6) of the Intergovernmental Panel on Climate Change (IPCC), there is unequivocal evidence that human activities are the primary driver of climate change (IPCC, 2021).

Climate change is leading to an increase in extreme weather events, including more frequent and severe heatwaves, storms, and irregular precipitation patterns. Heatwaves are becoming more intense and longer, posing increasing health risks. Heavy rainfall leads to floods that can devastate communities, destroy infrastructure, and disrupt local economies. Conversely, areas with reduced rainfall face prolonged drought conditions that threaten agriculture, water supplies, and biodiversity. Patz et al. (2014) also discussed how climate change directly affects health through increased frequency of heat waves and extremes in the global hydrologic cycle, such as droughts (Douville et al., 2015), floods, and heavy rainfalls. The IPCC AR6 (IPCC, 2021) reports that human-caused climate change has driven detectable changes in the global water cycle since the mid-20th century, increasing precipitation intensity and evapotranspiration, which contribute to drought conditions (Douville et al., 2015).

Aerosols, tiny particles suspended in the atmosphere, play a crucial role in climate systems by influencing cloud formation, weather patterns (Ramanathan and Carmichael, 2008), and the Earth's radiation balance. Meanwhile, many studies focused not only on the effects of aerosols on human health, but also

on the effects on the Earth's climate through the absorbing and scattering of sunlight and changes in cloud properties in atmospheric chemistry.

The interaction between aerosols and atmospheric transport is complex, as climate change can modify both the sources of aerosols and the mechanisms that transport them. For example, increased frequency and intensity of wildfires due to higher temperatures can elevate aerosol concentrations, while changing wind patterns can redistribute these particles over vast regions. Investigating these interactions through satellite remote sensing and other observational tools provides valuable insights into the broader impacts of climate change and informs strategies for adaptation and mitigation. Among these, changes in temperature, precipitation, and wind patterns alter the distribution and movement of aerosols in the atmosphere, which in turn affects air quality, weather patterns, and climate feedback mechanisms (Boucher, 2015). Understanding how climate change influences these dynamics is essential for predicting future environmental conditions and mitigating adverse effects on human health and ecosystems (Mushtaq et al., 2022).

As climate change increases the frequency and intensity of extreme weather events such as heatwaves, floods, and droughts, monitoring and analyzing these changes not only helps assess threats to ecosystems and human health but also reveals the complex roles of atmospheric components like aerosols in the climate system. Therefore, there is an urgent need to detect the effects of climate change quickly and accurately.

1.1. Scientific background

1.1.1. Climate change and global warming

Climate change refers to long-term changes in temperatures and weather patterns. While these changes can occur naturally, influenced by factors such as solar activity or major volcanic eruptions, human activities have become the dominant cause since the 19th century. This is largely attributed to the extensive use of fossil fuels, including coal, oil, and gases. According to the IPCC AR6, the global average surface temperature has increased by an estimated 0.8°C to 1.3°C, with a best estimate of 1.07°C, since the pre-industrial period (1850–1900) illustrated in Fig. 1.1(c) (IPCC, 2021). This warming is predominantly driven by human activities, particularly the emission of well-mixed greenhouse gases (GHGs), which alone contributed approximately 1.0°C to 2.0°C of warming. About other human drivers, such as aerosol emissions, contributing to a cooling effect of 0.0°C to 0.8°C. In contrast, natural drivers and internal variability had comparatively minor effects to changed global surface temperature, ranging from -0.1°C to +0.2°C.

If human activities and greenhouse gas emissions continue to rise at current rates, global warming is projected to reach 1.5°C above pre-industrial levels between 2030 and 2052. Such an increase would likely result in more severe climate impacts, including heightened heatwaves, more frequent and intense extreme precipitation events, and accelerated sea level rise, further exacerbating the risks to ecosystems and human societies.

In this study, we discuss climate change as significant alterations in the global climate resulting from the progression of global warming. Unlike natural fluctuations, it is a phenomenon driven by human activities, leading to a rise in the average temperature near the Earth's surface.

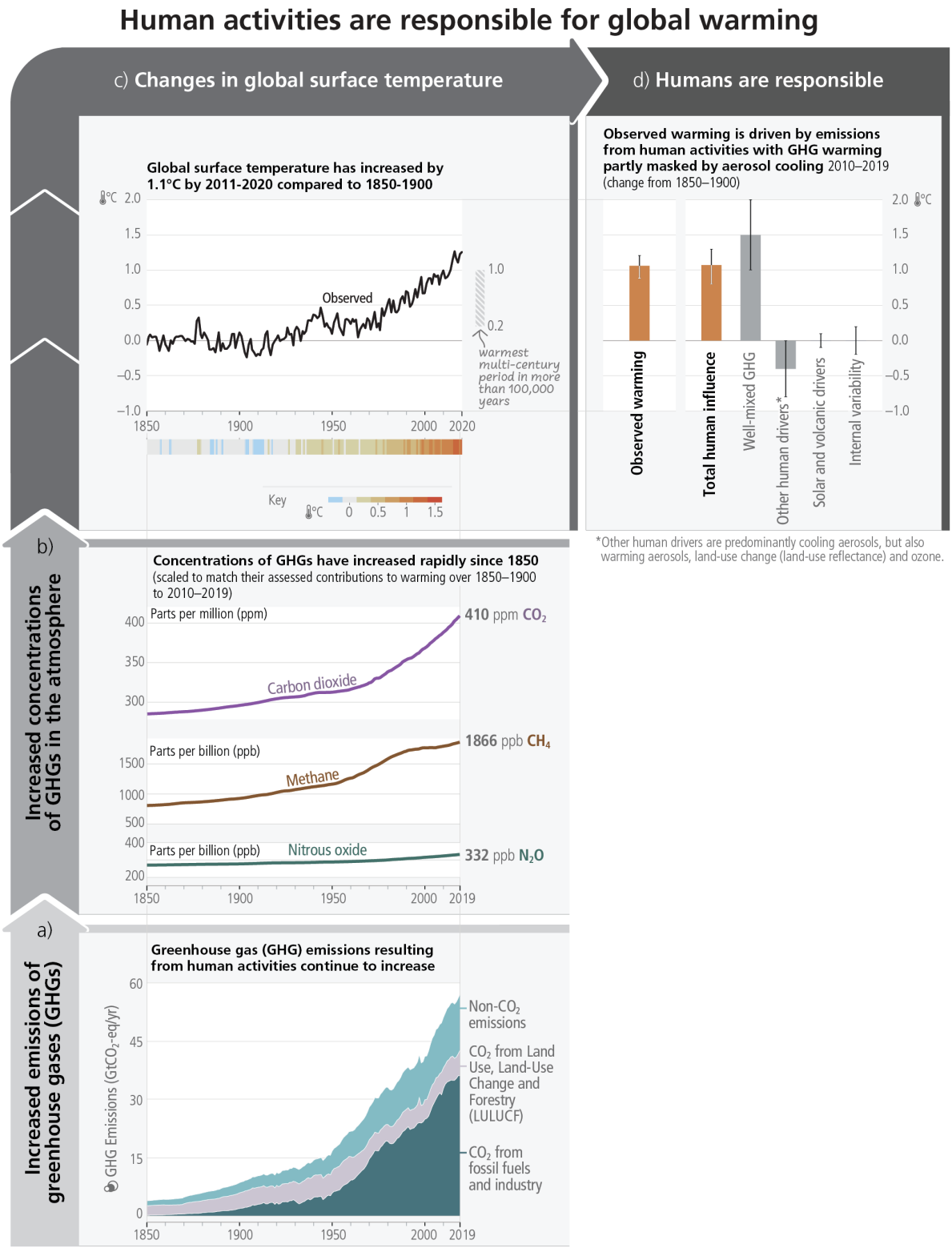

Fig. 1.1 The causal chain from emissions to resulting warming of the climate system. Emissions of GHG have increased rapidly over recent decades (panel (a)). Global net anthropogenic GHG emissions include CO_2 from fossil fuel combustion and industrial processes (CO_2-FFI) (dark green); net CO_2 from land use, land-use change and forestry (CO_2-LULUCF) (green); CH_4; N_2O; and

fluorinated gases (HFC_S, PFC_S, SF_6, NF_3) (light blue). These emissions have led to increases in the atmospheric concentrations of several GHG_S including the three major well-mixed GHG_S CO_2, CH_4 and N_2O (panel (b), annual values). To indicate their relative importance each subpanel's vertical extent for CO_2, CH_4 and N_2O is scaled to match the assessed individual direct effect (and, in the case of CH_4 indirect effect via atmospheric chemistry impacts on tropospheric ozone) of historical emissions on temperature change from 1850–1900 to 2010–2019. This estimate arises from an assessment of effective radiative forcing and climate sensitivity. The global surface temperature (shown as annual anomalies from a 1850–1900 baseline) has increased by around 1.1°C since 1850–1900 (panel (c)). The vertical bar on the right shows the estimated temperature (very likely range) during the warmest multi-century period in at least the last 100,000 years, which occurred around 6500 years ago during the current interglacial period (Holocene). Prior to that, the next most recent warm period was about 125,000 years ago, when the assessed multi-century temperature range [0.5°C–1.5°C] overlaps the observations of the most recent decade. These past warm periods were caused by slow (multi-millennial) orbital variations. Formal detection and attribution studies synthesise information from climate models and observations and show that the best estimate is that all the warming observed between 1850–1900 and 2010–2019 is caused by humans (panel (d)). The panel shows temperature change attributed to: total human influence; its decomposition into changes in GHG concentrations and other human drivers (aerosols, ozone and land-use change (land-use reflectance)); solar and volcanic drivers; and internal climate variability. Whiskers show likely ranges. Cited from IPCC (2021a, 2021b): {WGI SPM A.2.2, WGI Figure SPM.1, WGI Figure SPM.2, WGI TS2.2, WGI 2.1; WGIII Figure SPM.1, WGIII A.III.II.2.5.1}

1.1.2. Climate change and aerosols

Aerosols, microscopic particles suspended in the atmosphere, play a significant role in both weather and climate systems. These particles can originate from natural sources such as volcanic eruptions, sea sprays, and dust storms, or from human activities, referred to as anthropogenic sources, including industrial emissions and vehicle exhausts (Li et al., 2017). Aerosols vary widely in size, composition, and origin, influencing their interaction with sunlight and their lifespan in the atmosphere. Aerosols are a key component of the atmospheric system, influencing both weather and climate. The study of aerosols and their effects on atmospheric radiation and climate is crucial for understanding and predicting changes in the Earth's system. Research into anthropogenic aerosols and their management is particularly important in the context of global climate change and environmental sustainability (Satheesh & Moorthy, 2005), highlighting the need for continued and detailed investigation into these complex interactions.

Aerosols directly affect the climate by scattering and absorbing sunlight, which can either cool or warm Earth's surface depending on their properties. Indirectly, they influence the formation and properties of clouds. Aerosols act as cloud condensation nuclei around which water vapor can condense to form cloud droplets (Yu et al., 2013). This relationship between aerosols and clouds alters cloud reflectivity, stability, and lifetime, impacting precipitation patterns and climate (Lohmann, 2017). Understanding atmospheric radiation is another essential aspect of studying aerosols. Atmospheric radiation involves absorption, emission, and scattering of electromagnetic radiation by gases, aerosols, and clouds in the atmosphere (Kushta et al., 2014). The radiation balance is a critical component in climate models, as it involves the calculation of incoming solar radiation and outgoing infrared radiation. This balance determines the Earth’s temperature and climate. Aerosols complicate this

balance by affecting both the scattering of incoming solar radiation back into space and the absorption of heat within the atmosphere (Che et al., 2022). Fig. 1.2 presents a depiction of Earth's radiation budget, expressed as percentages of the solar constant (342 W m^{-2}) at the atmosphere's upper boundary. Approximately half of the incoming solar radiation manages to pass through clouds and greenhouse gases to reach the Earth's surface. These same gases and clouds then re-radiate a significant portion (equivalent to 88 units) of this absorbed energy back towards the surface, which is a fundamental component of the greenhouse effect mechanism. The extent of the greenhouse effect is often gauged by the difference between the blackbody radiation emitted from the Earth's surface, which at an average temperature of 288 K amounts to 390 W m^{-2}, and the longwave radiation leaving the top of the atmosphere, here depicted as 70 units or 239 W m^{-2}. Consequently, this difference is 151 W m^{-2}.

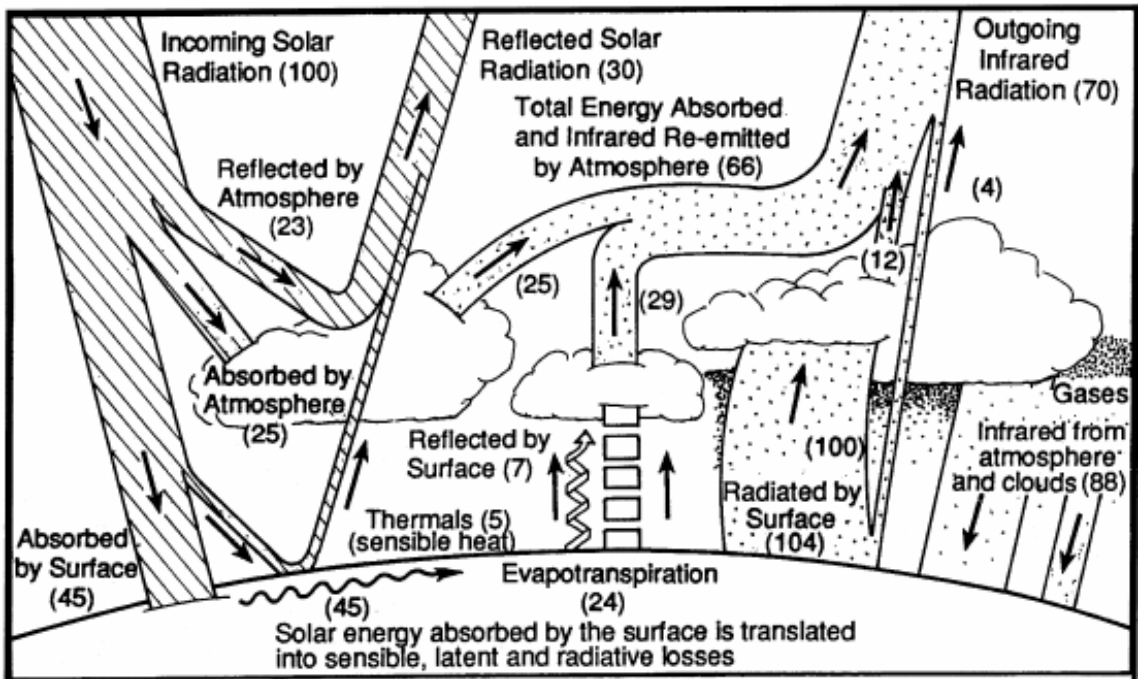

Fig. 1.2 Schematic of the Earth's energy budget. Units are expressed as a percentage of the total incident solar radiation, which is 342 W m^{-2}. Cited from SH Schneider et al. (1992) and McGuffie & Henderson-Sellers (2001).

1.1.3. Impacts of climate change on atmosphere, land, and oceans

Climate change has profound impacts on atmospheric dynamics and weather patterns. It intensifies extreme weather events such as heavy rainfall, hurricanes, and prolonged droughts, causing severe economic and social disruptions. Increased greenhouse gas emissions trap more heat in the atmosphere, leading to global warming, which enhances evaporation rates and alters precipitation patterns (Nica et al., 2019). Observations show that globally average precipitation over land has increased since the 1950s, with a sharper rise since the 1980s due to human influence (IPCC, 2021). Mid-latitude storm tracks have likely shifted poleward, altering weather systems and impacting pollutant transport (Zheng et al., 2024). These changes affect relative humidity, wind patterns, and precipitation variability, influencing aerosol distribution and atmospheric chemistry (Liu et al., 2020).

Climate change significantly impacts terrestrial ecosystems and land-use dynamics. Rising temperatures exacerbate soil dryness, intensify droughts, and reduce agricultural productivity (Trenberth, 2005). Altered precipitation patterns further stress water supplies, threatening food security and biodiversity. Deforestation, a drive of increased carbon dioxide levels, limits the Earth's capacity to sequester greenhouse gases, accelerating warming (IPCC, 2021). The poleward shift of climate zones, influenced by atmospheric circulation changes, redefines habitats and alters vegetation patterns, affecting ecosystems and human livelihoods (Mori et al., 2024). Land degradation, combined with rising temperatures, contributes to desertification in vulnerable regions and amplifies risks to human populations.

Climate change affects the ocean through increased temperatures, altered salinity, and rising sea levels. Warming oceans contribute to stronger and more frequent hurricanes and tropical storms, which devastate coastal areas and marine ecosystems (IPCC, 2021). Human influence has likely contributed to

observed changes in ocean salinity, with increased evaporation and altered precipitation redistributing water masses (IPCC, 2021). Coral reefs and mangroves, crucial for coastal protection and biodiversity, are at risk due to rising temperatures and acidification, reducing their ability to buffer storm surges (Guannel et al., 2016). Changes in ocean currents, driven by interactions with atmospheric processes, further disrupt marine ecosystems and fisheries, threatening food supplies for millions.

1.1.4. Variations in atmospheric transport fields under climate change

The atmospheric transport fields refer to the movement and redistribution of substances such as aerosols, water vapor, and pollutants within the atmosphere. Climate change significantly impacts the atmospheric transport fields through its influence on atmospheric circulation patterns. While atmospheric circulation refers to the large-scale patterns of air movement driven by differential heating, the Earth's rotation, and dynamic atmospheric processes (Lorenz et al., 1955), the atmospheric transport fields focus on how these movements govern the distribution and flow of substances. Climate changes directly impact on the transport of energy, moisture, and pollutants by altering key circulation features, such as wind speed, direction, and pressure gradients. For instance, wind patterns can dramatically influence the transport of pollutants across continents and oceans (Liu et al., 2020; Damiani et al., 2020). Shifts in jet streams or the weakening of polar vortices due to global warming (Holton et al., 2004) can significantly alter pollutant dispersion, long-range aerosol transport, and the frequency of transboundary pollution events.

Two key studies have explored how climate change influences atmospheric transport fields. Firstly, the shifting of mid-latitude storm tracks is a notable impact of climate change on atmospheric circulation patterns. The IPCC AR6 reports that since the mid-20th century, extratropical storm tracks have been

shifting poleward, particularly in both hemispheres since the 1980s, largely driven by human activities such as greenhouse gas emissions and ozone depletion (Shaw et al., 2016; Allan et al., 2020). For example, the Southern Annular Mode is closely related to these shifts in the Southern Hemisphere, with stratospheric ozone depletion and greenhouse gas increases being key contributors (Shaw et al., 2016). Fig. 1.3 shows a clear poleward shift in zonal wind speeds in the mid-latitudes (approximately 30° to 60°), indicating that the extratropical jets, which are high-speed wind bands, are progressively moving towards the poles. This shift is observed across different seasons in both the Northern and Southern Hemispheres, indicating a global trend. Additionally, previous studies by Manney et al. (2014) suggest a poleward shift of the tropospheric extratropical jets in all seasons (Fig. 1.4). This poleward shift of the Northern Hemispheres (NH) subtropical jet is broadly apparent over a wide longitude range but is weakly evident in the zonal mean. In the NH, over the eastern Pacific, the subtropical jet shifted equatorward in winter. Changes in NH high-latitude jet frequency are largely consistent with an equatorward shift of the polar jet. The NH subtropical jet shifts poleward in winter over Asia and in fall over the western Pacific, while a strong equatorward shift is observed in winter over the eastern Pacific.

Secondly, atmosphere-ocean coupling plays a significant role in amplifying atmospheric variability in mid to high-latitude regions which amplifies the meandering of the westerly jet stream in mid- to high-latitude regions. Fig. 1.5 shows that the interaction between the atmosphere and ocean intensifies wintertime variability, particularly in the Northern Hemisphere's key regions, such as the North Pacific, North Atlantic, and northern Eurasia. Mori et al. (2024) found that atmosphere-ocean coupling selectively enhances certain large-scale teleconnection patterns, such as the Pacific-North American pattern and the North Atlantic Oscillation, thereby amplifying their influence on atmospheric

variability. A large-scale numerical climate simulation revealed that atmosphere-ocean coupling explains approximately 13%, 11%, and 10% of the variability in the Pacific-North American pattern, the North Atlantic Oscillation, and the Arctic warming-midlatitude cooling pattern, respectively.

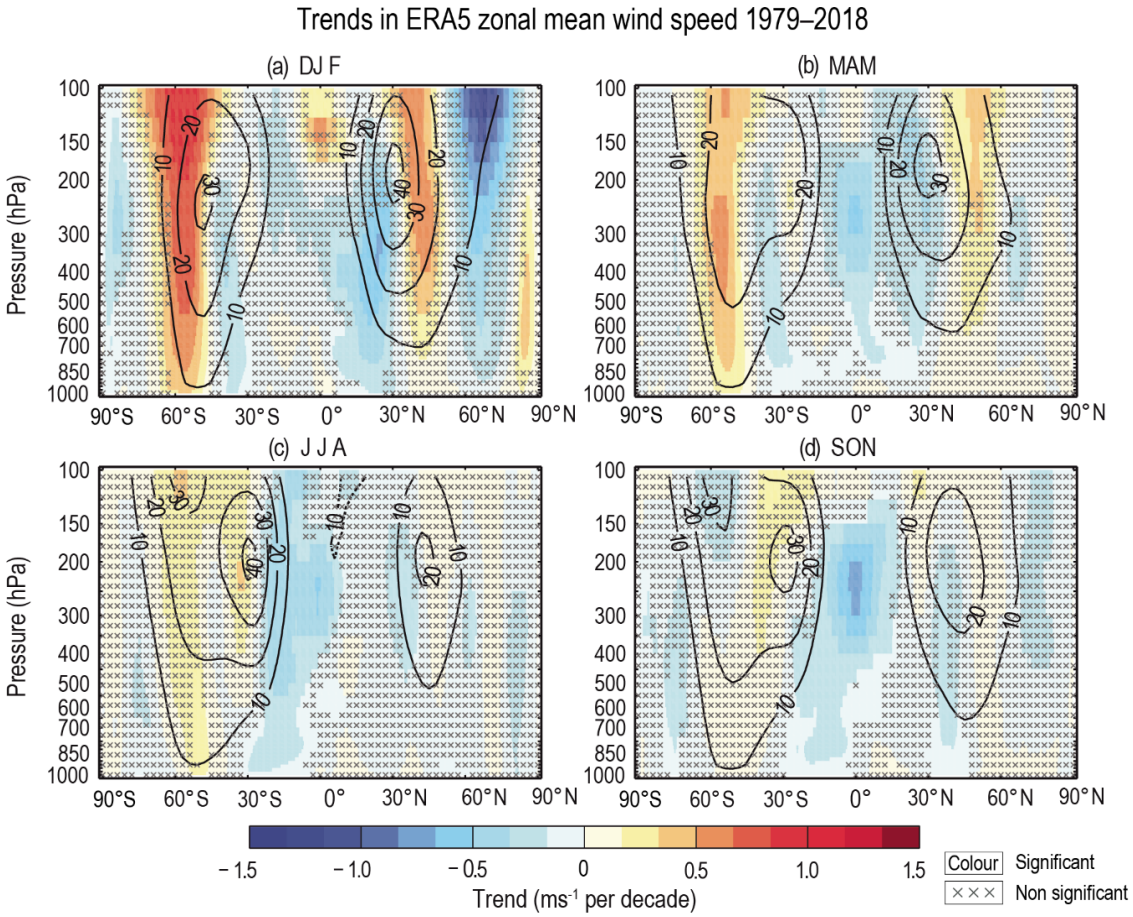

Fig. 1.3 Trends in ERA5 zonal-mean zonal wind speed. Shown are (a) DJF (December–January–February); (b) MAM (March–April–May); (c) JJA (June–July–August); and (d) SON (September–October–November). Climatological zonal winds during the data period are shown in solid contour lines for westerly winds and in dashed lines for easterly. Trends are calculated using OLS regression with significance assessed following AR (1) adjustment after Santer et al. (2008) ('×' marks denote non-significant trends). Cited from IPCC (2021a), Chapter 2, Figure 2.18.

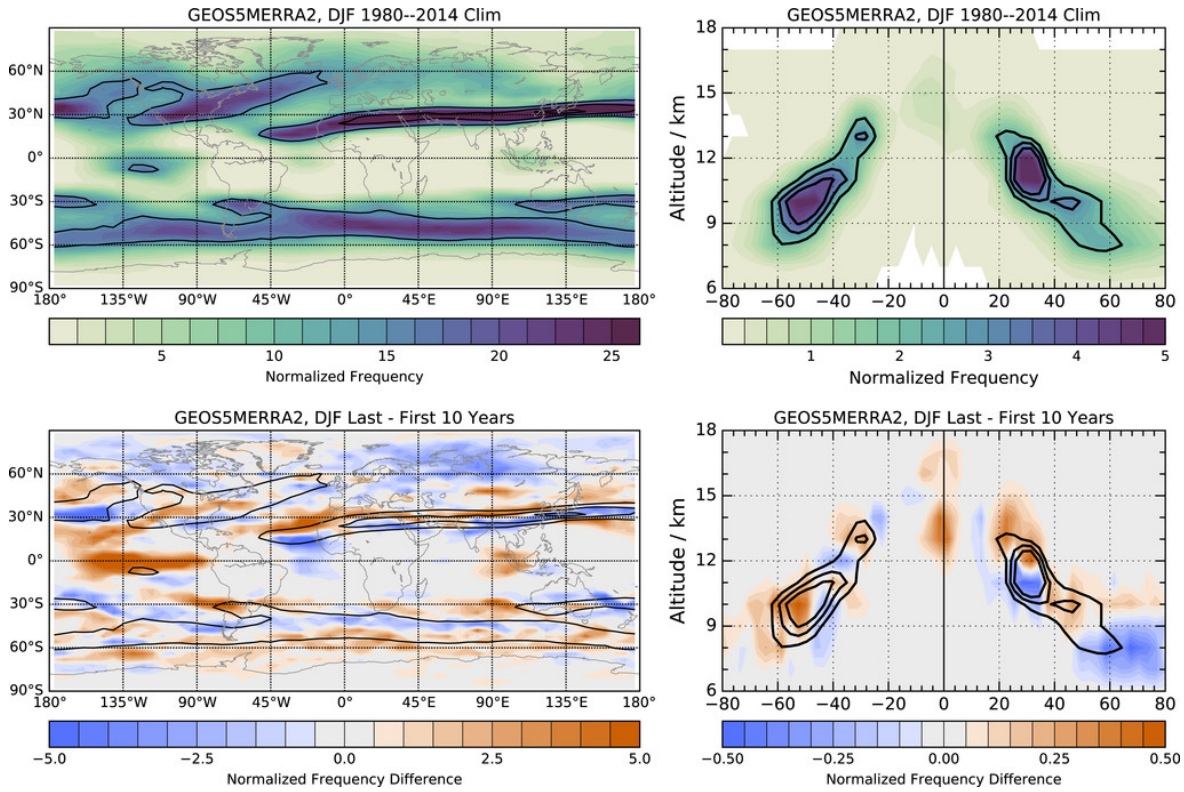

Fig. 1.4 Climatological jet frequency distributions are presented as percentages, with maps on the left and cross sections on the right. Differences between distributions in the first and last 10 years of the record are shown at the bottom of the figures, expressed in percentage points from the MERRA-2 reanalysis for DJF. Overlaid black contours indicate climatological frequency levels of 15%, 30%, and 45% on the maps, and 2%, 3%, and 4% on the cross sections. Cited from Manney et al. (2014).

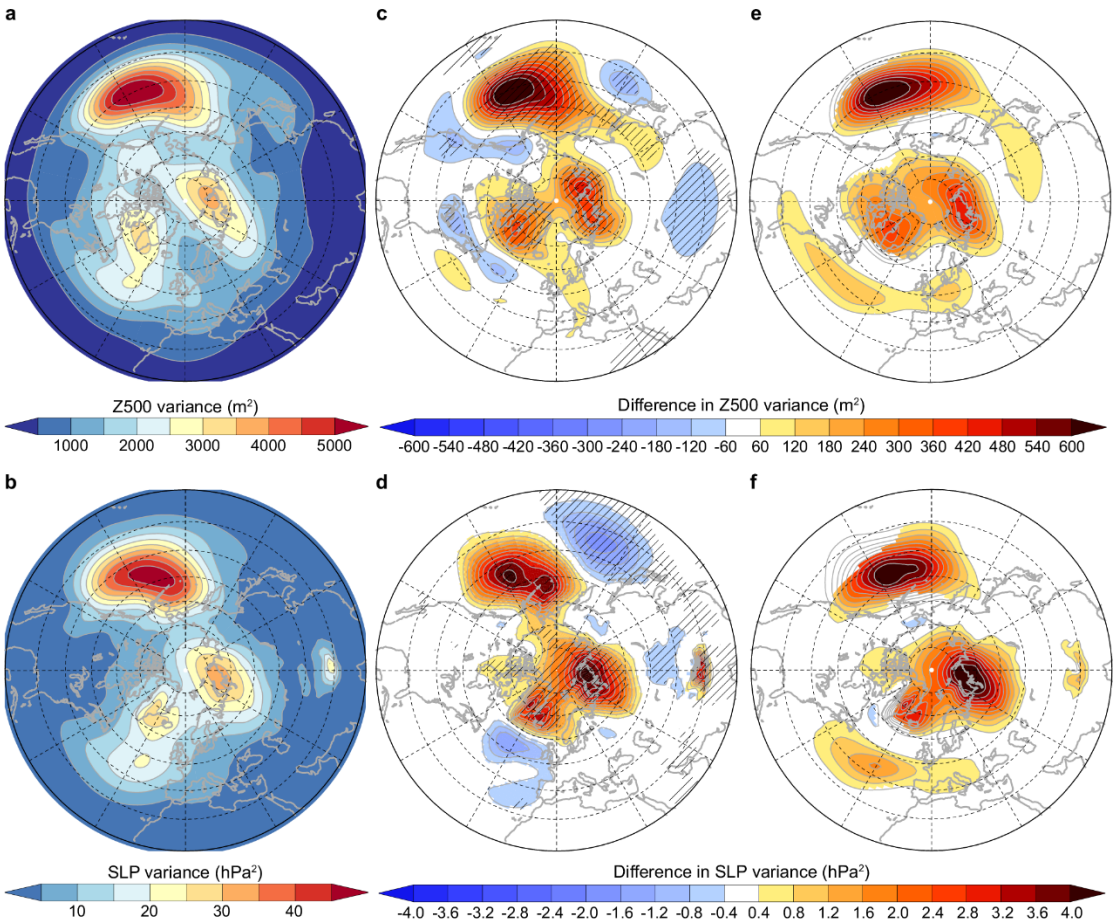

Fig. 1.5 Variance of DJF-mean anomalies for Z500 (a, in m²) and SLP (b, in hPa²) from the C-run. Panels (c) and (d) show the variance difference in Z500 and SLP between the C- and A-runs (C-run minus A-run), with hatched areas indicating statistical confidence exceeding the 95% level, based on a two-sided F-test. Panels (e) and (f) display the same differences as in (c) and (d) but reconstructed from the three leading EOT modes of Z500 variability, with color shading applied only where statistical confidence surpasses the 95% threshold according to a two-sided F-test. Cited from Mori et al. (2024).

1.1.5. Changes in transboundary air pollution pathway associated with climate change

1.1.5.1. Transboundary air pollution

Transboundary air pollution is a process where airborne pollutants cross national borders and impact distant regions (Narita et al., 2019; Keeley & Yisheng, 2011; Gu et al., 2024). This issue is a growing concern globally, with profound health and environmental effects. East Asia is a classic example, where pollutants from China are transported by winds to nearby nations, including Japan (Lu et al., 2011; Jion et al., 2023). Oanh et al. (2012) have confirmed the transboundary air pollution to Japan through trajectory analysis.

Japan, especially the city Fukuoka which located in western Japan regularly encounters transboundary pollution chiefly due to its closeness to China, a major source of industrial pollutants (Hosono et al., 2022; Jafari et al., 2021; Yim et al., 2019; Yoshino et al., 2021). Fig. 1.6 shows the variation of NO_2 and O_3 over time, distinguishing between local pollution levels in Fukuoka and contributions from transboundary pollution. The study examined the impact of transboundary air pollution and local air pollution on Fukuoka's air quality during the winter of 2018. During the period of transboundary air pollution, concentrations of most pollutants, including NO_x and particulate matter, were elevated, while during the period of local air pollution, these pollutants were lower. However, ozone levels were higher during the transboundary air pollution period, suggesting that it was transported from outside the city, primarily from the Asian continent.

Several factors contribute to the significant transboundary pollution from China to Japan. The East Asian monsoon and prevailing westerlies are crucial in carrying pollutants across the region (Hosono et al., 2022; Zhong et al., 2013). The prevailing westerlies from the China continent towards Japan, most prominently from late winter to early spring (Hosono et al., 2022). The Pacific

region between China and Japan serves as a unique open-source pathway for transboundary pollution, providing insight into using anthropogenic aerosols as tracers to detect changes in atmospheric transport patterns associated with climate change.

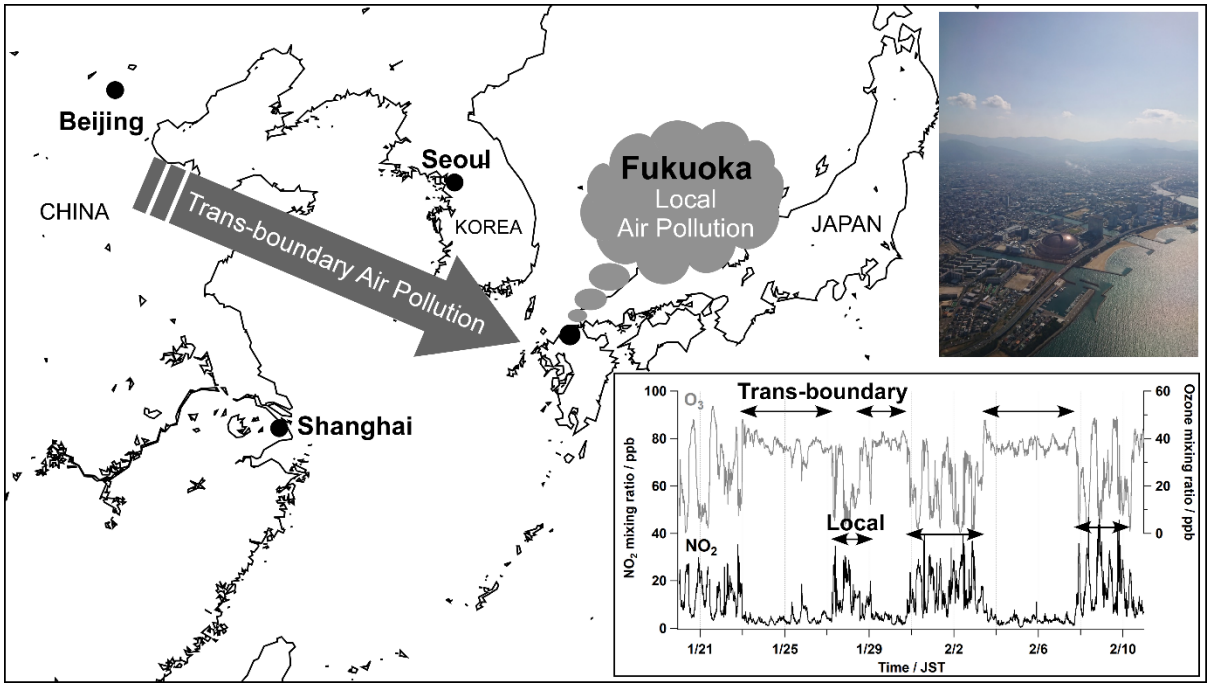

Fig. 1.6 Transboundary air pollution impacts on Fukuoka, Japan. Cited from Yoshino et al. (2021).

1.1.5.2. Air pollution and China’s emission

Air pollution is the introduction of harmful substances into the atmosphere that are detrimental to living organisms and the environment (Li et al., 2023; Xu et al., 2023). This issue has become more prevalent with the rise of industrial activities and increased numbers of vehicles on the road (Epstein et al., 2011). Key pollutants include particulate matter, nitrogen oxides, sulfur dioxide, volatile organic compounds, and carbon monoxide, arising from multiple sources including industrial activities, vehicle emissions, burning fossil fuels, and farming practices. The consequences of air pollution are widespread and significant. It can harm human health, leading to respiratory problems, cardiovascular disease, and early mortality (Babu and Aravinth, 2022). Ecologically, it may result in acid rain, nutrient overload in water systems, and damage to wildlife habitats (Sutton et al., 2019; Pereira et al., 2021). Economically, the health impacts of pollution lead to greater medical expenses and reduced worker productivity (Zhou et al., 2024). Air pollution levels in major cities worldwide for the year 2022. The average concentration of $PM_{2.5}$, which serves as an indicator of air quality, in comparison to the World Health Organization (WHO)'s guidelines. Cities such as Cairo, Dubai, and Mumbai are highlighted for their notably high $PM_{2.5}$ levels, which surpass WHO guidelines several times.

In East Asia, China is a major contributor to air pollution, a consequence of its swift industrial expansion and urbanization. Large Chinese cities frequently endure heavy smog incidents that present significant health hazards to their populous (Vennemo et al., 2009). Many research efforts have been undertaken to analyze the air quality in China, exploring pollutant sources, how economic growth influences air quality, and how pollution moves between countries (Gardner, 2018). Studies on air pollution in China have prompted various initiatives and changes in policy, aiming to enhance air quality. These include

enacting more rigorous emission regulations, encouraging the adoption of renewable energy, and investing in technologies to control pollution.

China is a major contributor of air pollution over East Asian, primarily driven by rapid economic growth and anthropogenic activities, including fossil fuel combustion and long-range transboundary of air pollutants, including sulfur dioxide (SO_2), nitrogen oxides (NO_x), and particulate matter ($PM_{2.5}$), adversely affecting air quality both within the country and in neighboring regions (Shi et al., 2022; Huang et al., 2020; Jyethi, 2016). Recognizing the serve situation of air pollution, the Chinese government implemented the Clean Air Action in 2013, aimed at drastically reducing pollutant emissions. Anthropogenic emissions from China were reduced by 62 % for SO_2, 17 % for NO_x, and 35 % for $PM_{2.5}$ from 2010 to 2017. These rates of emission reduction significantly accelerated after 2013, largely due to China's Clean Air Action (Zheng et al., 2018).

These substantial reductions in aerosol emissions have notable climatic implications. According to a study by Samset et al. (2018), globally and in three selected aerosol emission regions (Europe, East Asia, and the U.S.), the temperature change over land due to GHG warming is 30% stronger than the global mean. However, aerosol emission reductions result in a 50% stronger land temperature increase than the global average, consistent with previous findings (Shindell, 2014). The major aerosol emission regions exhibit even higher ratios under aerosol removal, primarily due to significant reductions in local sulfate-induced cooling. East Asia shows a much stronger response to aerosol reductions. The study found that precipitation in East Asia increases by 15% per °C of warming due to aerosol reductions (Samset et al., 2018). This indicates that East Asia is a region where extreme precipitation is particularly sensitive to reductions in aerosol emissions. Given the substantial reduction in anthropogenic emissions from China, our study focuses on anthropogenic

aerosols from China to further investigate this phenomenon and its climatic impacts.

Although air quality in China has improved since 2013, the country remains a significant source of anthropogenic emissions in East Asia. Japan, located downwind of China, frequently experiences air pollution that originate from its neighbor (Ryu et al., 2024). These transboundary pollution events are influenced by specific atmospheric conditions such as prevailing westerlies over the Pacific Ocean, which efficiently carry pollutants from China to Japan and other countries in East Asia (Li et al., 2016; Yamashita et al., 2017). The pathways of transboundary air pollution are particularly pronounced downwind of the Pacific from China. This region has been selected as our study area due to its unique open ocean area, which can effectively capture the transport phenomenon with minimal influence from human activities.

1.1.5.3. Impacts of climate change on transboundary air pollution pathway

Climate change is closely connected to the variation in transboundary air pollution. The atmosphere's ability to retain pollutants, such as aerosols, for extended periods increases due to global warming. Increased atmospheric stability allows pollutants to travel further before settling, worsening transboundary air pollution issues. The IPCC notes that this process is expected to intensify with continued global warming, facilitating the long-range transport of pollutants across borders and over vast regions (IPCC, 2021). Regions situated downwind of major pollution sources, especially industrial zones, are particularly vulnerable to the resulting air quality deterioration. Chakraborty et al. (2021) documented significant air quality decline in areas downwind from industrial emissions, where pollutants originating far away heighten local environmental health risks. This situation is becoming more common as

emissions from rapidly industrializing nations combine with those from established industrial regions (Abas et al., 2019), creating complex transboundary air pollution patterns.

Fig. 1.7 from the study provides an insightful visualization of the climatological distribution of column tracer mass during both winter (DJF) and summer (JJA) across different regions, including East Asia, Europe, and North America. The figure indicated the critical role of midlatitude jet stream variations in modulating the long-range transport of air pollutants into the Arctic. For example, panels (b) and (c) highlight the significant transport from East Asia (EA) and Europe (EUR) during winter. The white arrows in the DJF plots show that strong eastward winds and a southward shift of the jet stream facilitate the poleward transport of pollutants. The high tracer concentrations in the Arctic during winter (seen in panels a–g) are directly influenced by the position of the midlatitude jet stream. It has been revealed that the variability of the mid-latitude jet stream significantly affects the year-to-year fluctuations in the long-range transport of atmospheric pollutants to the Arctic, thereby impacting the Arctic climate.

As climate change progresses, the distribution of aerosols indirectly reflects the impact of climate change by affecting local and global air quality dynamics. Therefore, the study of aerosols is indispensable when studying the effect of climate change.

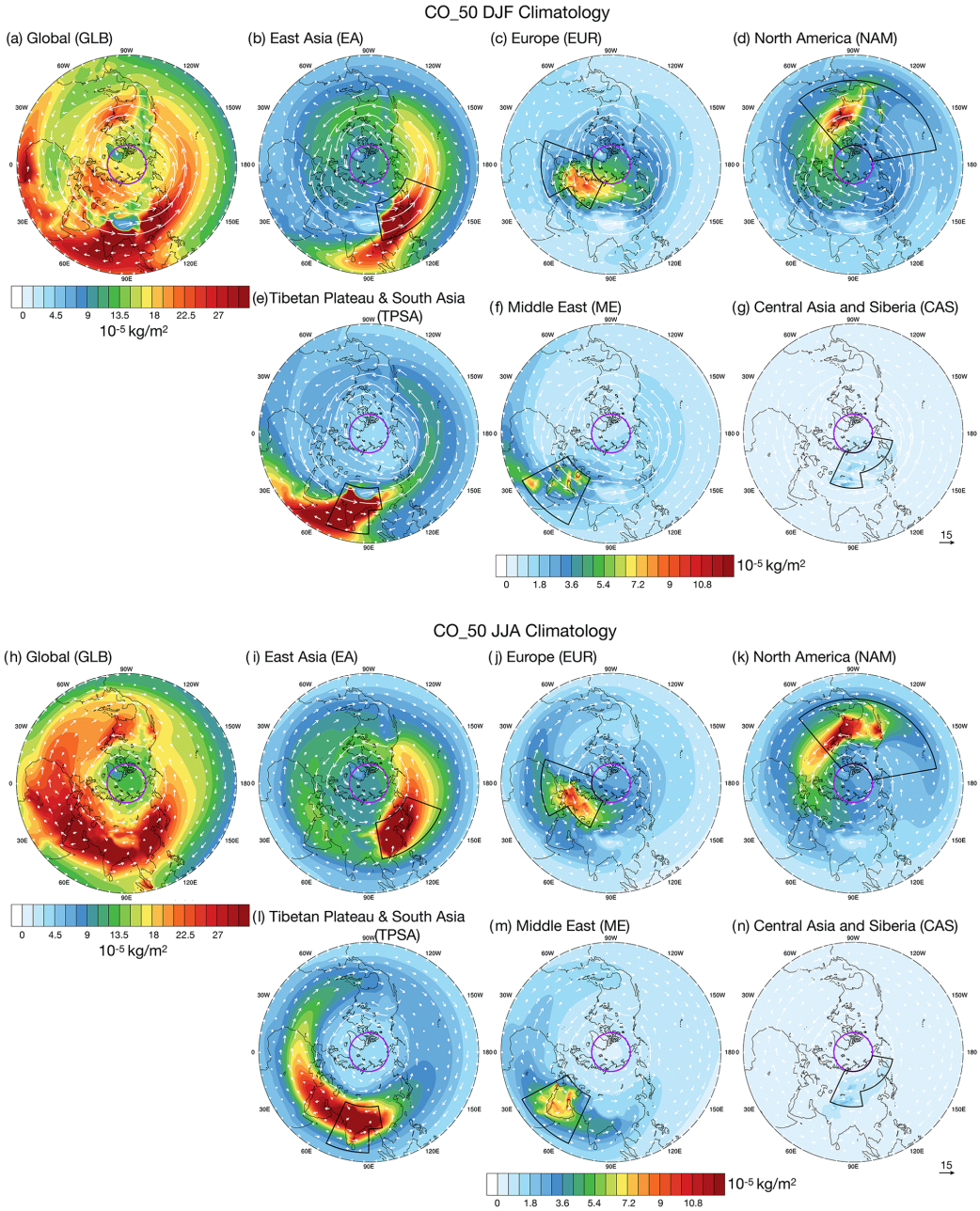

Fig. 1.7 Climatological distribution of column tracer mass (in kg m^{-2}) for both winter (a–g) and summer (h–n) across various regions: Global (GLB), East Asia (EA), Europe (EUR), North America (NAM), Tibetan Plateau & South Asia (TPSA), Middle East (ME), and Central Asia & Siberia (CAS). White arrows indicate the climatological wind patterns at the 500 hPa level, with the arrow scaling provided in the bottom right of panels (g) and (n) (units: m/s). The purple circle marks the Arctic boundary at 70°N latitude. Cited from Zheng et al. (2024).

1.2. Research challenges

Previous studies have shown that climate change impacts atmospheric circulation patterns. For instance, Fig. 1.3 from the IPCC AR6 analyzes westerly wind speed trends, with contour lines representing wind speed and the color bar indicating decadal trends. The horizontal axis represents latitude. The figure suggests that as climate change progresses, the mid-latitude jet stream is shifting poleward. Other research has shown that westerly meanders are amplified by air-sea interactions in mid-to-high latitudes (Fig. 1.5) and that changes in the mid-latitude jet stream significantly affect long-range transport of air pollutants to the Arctic (Fig. 1.7). As climate change progresses further, it is suggested that changes in atmospheric circulation patterns will alter atmospheric transport fields, consequently affecting the distribution of aerosols and transboundary air pollution.

By considering aerosols as tracers and observing changes in their distribution, we might be able to capture changes in atmospheric transport fields associated with climate change. This insight suggests that long-term aerosol data, such as AOD, could potentially be used as a tracer for observing the meteorological conditions.

However, previous studies have mainly relied on reanalysis data or models, with limited use of observation-based methods to evaluate the effects of climate change. While model simulations have been predominantly used, they have proven insufficient for understanding the complex interactions between aerosols and climate change (Wang et al., 2003; Wu et al., 2020). Observational data is vital for validating and improving these model outputs. Studies by Cao et al. (2023) and Park et al. (2023) have highlighted the critical role of observational data, including satellite-derived AOD measurements, in confirming and refining model predictions. Gao et al. (2022) similarly noted that models may fail to accurately capture the climate effects of aerosol mixing

states without integrating observational data. These studies highlight the necessity of observational data showing the impact of climate change on atmospheric phenomena clearly.

Due to the current lack of sufficient observational evidence showing the effects of climate change, this study aims to detect the transboundary air pollution variation associated with climate change using observational aerosol data as a tracer.

1.3. Purpose

Climate change is causing extreme weather events and posing serious threats to human life. According to the AR6 of the IPCC, there is unequivocal evidence that human activities are the primary driver of climate change, underscoring the urgent need for accurate detection of its impacts. The AR6 further reports that as climate change progresses, the mid-latitude temperate jet streams are shifting poleward. As climate change progresses, changes in atmospheric transport fields in the mid-latitude regions have been reported. Variations in atmospheric transport fields influence the distribution of aerosols and are expected to change transboundary air pollution pathways globally. Although future climate change predictions have been made, there is a possibility that climate change will become more severe than predicted, so it is essential to detect climate change quickly and accurately. However, observational evidence to support this remains limited.

In this study, we aim to clarify the detectability of transboundary air pollution pathway variations associated with climate change using anthropogenic aerosols.

1.4. Paper structure

Chapter 1 provides an introduction, highlighting the challenges caused by climate change and the purpose of the study, which aims to clarify the possibility of detecting climate change impacts using aerosol satellite remote sensing. Chapter 2 reviews the principles and methods of aerosol satellite observations, including satellite observations of aerosols, especially MODIS, and their limitations. It provides a comprehensive overview of AOD retrieval methods, the MODIS DT-ocean algorithm, and discusses future perspectives in satellite observation technologies. Chapter 3 describes the reanalysis and climate model datasets used in this study, focusing on MERRA-2 and SPRINTARS. Also, the algorithms applied to aerosol transport and AOD calculations in each dataset have been introduced. Chapters 4 to 6 of this thesis are based on the paper of Cai et al. (2024). These chapters include an analysis of AOD trends in East Asia, the proposal of a new metric, and an evaluation of atmospheric transport variability over 19 years. Chapter 7 examines the transboundary air pollution pathway variations in recent decades.

Chapter 2. Satellite observations of aerosols

This chapter introduces satellite-based aerosol monitoring, with a particular focus on Moderate Resolution Imaging Spectroradiometer (MODIS) onboard NASA's Terra and Aqua satellites. Additionally, the theory of Aerosol Optical Depth (AOD) is presented. The chapter highlights the MODIS aerosol retrieval methods, emphasizing the Dark Target (DT) algorithm for ocean observations. This algorithm utilizes spectral reflectance data to distinguish aerosols from surface and atmospheric signals. Key advancements include improved cloud masking, and a wind speed-dependent adjustment introduced in Collection 6 (C6).

2.1. Satellite observations of aerosols

Aerosol monitoring has greatly benefited from a range of satellite missions, each offering unique perspectives and techniques to observe aerosols in the atmosphere. Among these, NASA's Terra and Aqua satellites equipped with the MODIS are particularly notable for their contributions to long-term aerosol monitoring. MODIS provides AOD data, a dimensionless parameter that measures the extent to which aerosol particles in the atmosphere absorb or scatter solar radiation. This metric quantifies the attenuation of sunlight as it passes through the atmosphere and is essential for understanding the global distribution, variability, and trends in aerosol concentrations (Hao et al., 2023).

In addition to MODIS, several other satellite missions have advanced aerosol research. The European Space Agency's Sentinel-5P, equipped with the TROPOspheric Monitoring Instrument (TROPOMI), provides high-resolution data on aerosols and trace gases, enhancing our understanding of air quality and pollution sources. Similarly, NASA's Multi-angle Imaging

SpectroRadiometer (MISR) onboard the Terra satellite offers multi-angle observations, enabling detailed characterization of aerosol properties and vertical distributions (Hao et al., 2023).

The Cloud-Aerosol Lidar and Infrared Pathfinder Satellite Observation (CALIPSO), a joint mission by NASA and the French space agency CNES, employs lidar technology to provide vertical profiles of aerosols and clouds. Furthermore, CALIPSO's vertical profiling capabilities have enabled detailed studies of aerosol transport mechanisms, such as how pollution from Asia can be transported across the Pacific Ocean, affecting air quality and climate in North America (Kondragunta & Zhu, 2024). It also helps elucidate the interactions between aerosols and clouds. Similarly, MISR's multi-angle data has offered insights into aerosol size distribution and composition, enhancing the ability to distinguish between types of aerosols such as dust, smoke, and urban pollution (Schumacher et al., 2024; Zeydan & Yıldırım, 2024).

Among the diverse satellite missions, MODIS stands out for its longevity and data consistency. Since 2003, MODIS AOD data from the Terra and Aqua satellites have provided an unparalleled long-term record of aerosol observations. This extensive dataset allows for comprehensive analyses of the spatial and temporal variations in aerosol concentrations over the past two decades. It is particularly valuable for identifying trends linked to natural and anthropogenic factors, such as wildfires, dust storms, industrial emissions, and biomass burning (Hao et al., 2023).

Another major advantage of MODIS is its broad spatial coverage, offering near-daily global observations of aerosol distributions. The application of MODIS data in aerosol research has proven critical for climate modeling and air quality assessments. For example, researchers have used MODIS data to explore the impacts of aerosols on radiative forcing, cloud interactions, and climate feedback mechanisms (Hao et al., 2023).

Compared to other satellite missions, such as TROPOMI and MISR, which provide high-resolution or multi-angle observations, MODIS remains a cornerstone for long-term global aerosol monitoring due to its robust data continuity, wide spatial coverage, and well-documented data quality (Xia et al., 2023). These features make MODIS the preferred choice for studies requiring consistent, long-term datasets, particularly those focused on trends in aerosol concentrations and their effects on climate and air quality.

Given the long-term availability and consistency of MODIS AOD data, this study mainly used MODIS AOD data to detect the impacts of aerosols on climate change. By considering aerosols as tracers, this study aims to detect the impacts of climate change from observational data, providing crucial insights into climate variability and its broader environmental implications.

2.2. MODIS

MODIS is an instrument mounted on NASA's Terra and Aqua satellites. It plays a vital role in monitoring the Earth’s surface and atmosphere, delivering comprehensive data with global coverage. Specifically designed to capture the intensity of solar radiation that is reflected and emitted by the Earth, MODIS operates across a broad spectral range, from 410 nm to 14385 nm, divided into 36 bands (Table 2.1) and covering a vast 2330 km swath (Justice et al., 2002).

For aerosol monitoring, MODIS uses its capabilities to measure AOD at 550 nm with a spatial resolution of 10 ×10 km. The MODIS AOD 550 nm data for band 4 (Table 2.1) used in this study were obtained from the Level-2 monthly Atmospheric Aerosol Product, specifically the MOD04_L2 and MYD04_L2 collections, updated to Collection 6.1 for improved data processing and algorithm refinement. Each MOD04_L2 product file covers a five-minute time interval. These Level-2 AOD products were retrieved using the Dark Target (DT)

and Deep Blue (DB) algorithms (Hsu et al., 2004; Levy et al., 2013). In this study, we used only oceanic Level-2 AOD data retrieved with the DT algorithm. More details about the MODIS AOD retrieval method are provided in Section 2.3.2.

The long-term data collection from 2003 to 2021 by MODIS has indeed provided a rich dataset extensively utilized by researchers to analyze atmospheric aerosol concentrations and their effects on climate change, metrological fields condition. These studies reveal how human activities, and natural phenomena influence global atmospheric conditions. For instance, research has highlighted the influence of aerosols on climate change and their role in air quality degradation, impacting human health and the environment across regions like Australia (Yang et al., 2021) and Asia (Jin et al., 2023). By utilizing the value of MODIS data can enhance understanding of the spatial distribution and temporal evolution of aerosols, offering essential insights into the pattern of aerosol variation on a global scale.

Table 2.1 The main wavelength bands of the MODIS sensor. Cited from Remer et al. (2002).

Band	Primary use	Wavelength (nm)	Spatial resolution
1	Land / Cloud / Aerosol Boundaries	620–670 (Visible spectrum, red)	250m
2		841–876 (Near-infrared)	
3	Land / Cloud / Aerosol Properties	459–479 (Visible spectrum, blue)	500m
4		**545–565 (Visible spectrum, green)**	
5		1230–1250 (Short-wavelength infrared)	
6		1628–1652 (Short-wavelength infrared)	
7		2105–2155 (Short-wavelength infrared)	
8~36	Below, omitted		1000m

2.3. Aerosol retrieval methods

MODIS employs advanced algorithms to retrieve aerosol properties over diverse surfaces. The fundamental assumption is that in a clear-sky (cloud-free) scenario, the solar radiation backscattered by aerosols exhibits distinct spectral characteristics compared to the Earth's surface or atmospheric molecules. By analyzing multiple wavelength bands in the visible (VIS), near-infrared (NIR), and shortwave-infrared (SWIR) regions, it is possible to retrieve the aerosol signature and deduce their physical properties within the scene.

The MODIS AOD retrieval algorithm relies on the instrument's multi-spectral capabilities and precomputed lookup tables (LUTs) to infer aerosol properties

from top-of-atmosphere (TOA) reflectance measurements. Using data collected in clear-sky conditions, MODIS distinguishes aerosol signals based on spectral differences between the Earth's surface, atmospheric molecules, and aerosols. Two retrieval methods are implemented depending on surface types: the DT and DB algorithm. There are two DT algorithms for retrieving (1) over ocean (dark in visible and longer wavelengths) and (2) over vegetated/ dark-soiled land (dark in the visible). The DB algorithm is designed for bright surfaces, such as deserts and arid land. In this study, we only used the open ocean MODIS AOD data, so the DT-ocean algorithm will be introduced in detail. This section discusses the theory of AOD and DT-ocean algorithm of MODIS aerosol retrieval based on Levy et al. (2009b, 2013), Remer et al. (2005, 2008, 2012) and Martins et al. (2002).

2.3.1. AOD

AOD is a crucial physical parameter for characterizing aerosols and a key factor in evaluating transboundary air pollution and climatic change. Aerosols play a significant role in atmospheric science as they affect the earth's energy balance and can influence weather patterns and climate (Wang, J. 2003; Gu et al., 2018; Che et al., 2019).

Meteorological conditions, such as temperature, wind patterns, and humidity, are crucial in determining the distribution of aerosols within the atmosphere. Studies like those by Ratnam et al. (2021) have shown that these meteorological parameters significantly impact AOD variability. Moreover, research by Che et al. (2019) demonstrated that meteorological parameters accounted for a larger fraction of AOD variability (20.4%–72.8%) compared to emissions from human activities (0%–56%) during 1980-2014 (Fig. 2.1).

Horizontal gradients of aerosols significantly affect cloud formation and precipitation in the atmosphere. These gradients can lead to changes in weather patterns across different scales, from local to global. According to Leung et al. (2023), thermal circulation, driven by temperature differences, can further enhance the transportation of aerosols, altering their spatial distribution and movement.

Understanding the influence of aerosols on climate and weather is particularly important for studying horizontal AOD gradients, which can offer insights into how climate change is altering meteorological fields and affecting transboundary air pollution pathways. However, our current understanding of the impact of climate change on these meteorological fields is still limited. Future climate phenomena, such as El Niño, could significantly affect global weather patterns and, consequently, aerosol distributions (Gan et al., 2023).

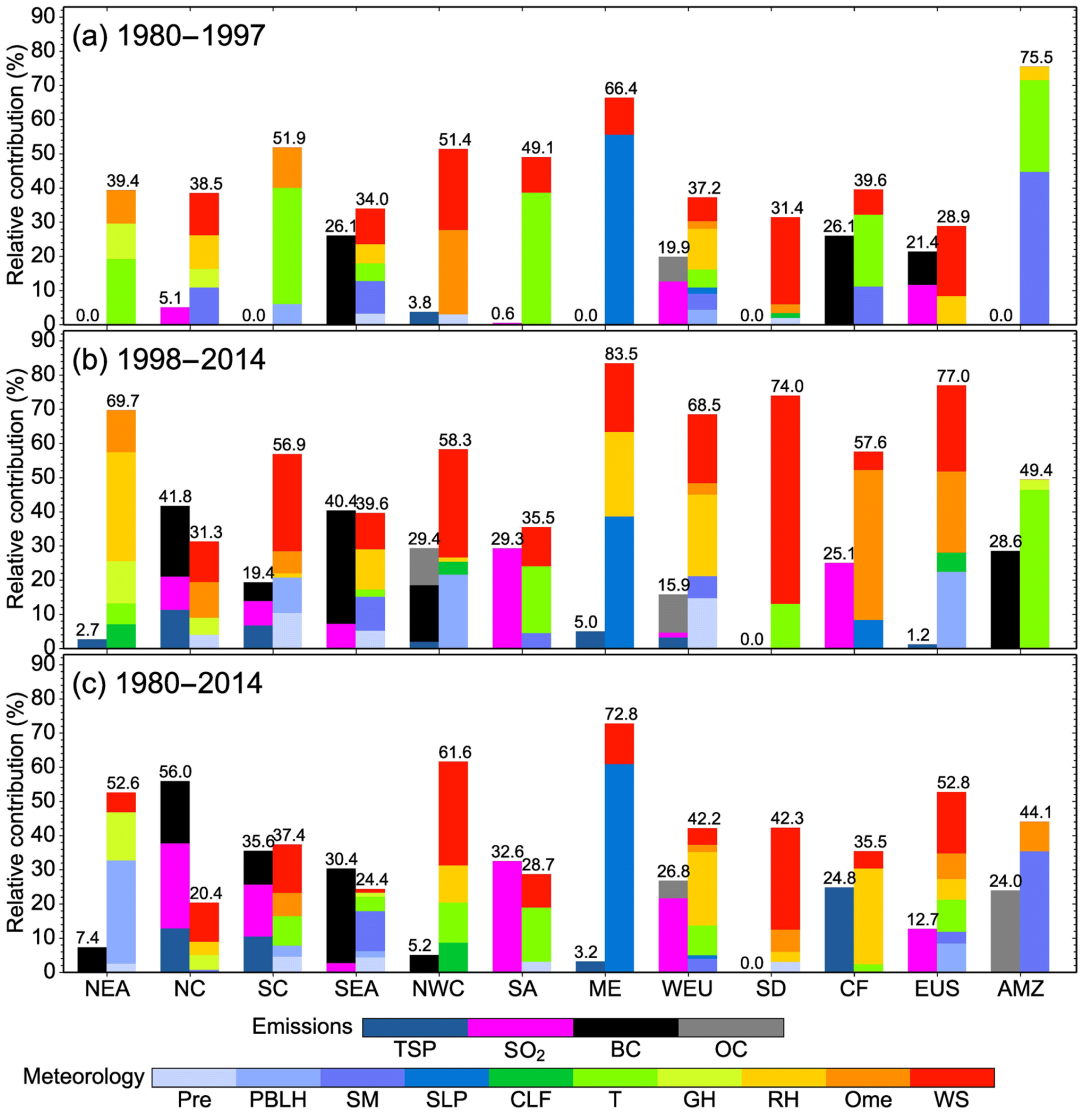

Fig. 2.1 The (Lindeman, Merenda and Gold) LMG method estimated the relative contributions (%) of total variances in a stepwise multiple linear regression model, comparing local emission factors (left bars) and meteorological variables (right bars) across 12 regions during three periods: (a) 1980–1997, (b) 1998–2014, and (c) 1980–2014. Meteorological parameters were grouped by temperature, geopotential height, relative humidity, vertical velocity, and wind speed. Cited from Che et al. (2019).

2.3.1.1. Extinction coefficient

To understand the theory of AOD, it is necessary to first introduce the concept of the extinction coefficient, which requires a clear understanding of the definitions of absorption and scattering cross-sections. The aerosol absorption coefficient ($\sigma_{a,a,\lambda}$) and the scattering cross-sections ($b_{s,a,i,\lambda}$) can be calculated as follow, according to (Bohren et al., 2008):

$$\sigma_{a,a,\lambda} = \sum_{i=1}^{N_B} n_i b_{a,a,i,\lambda} \tag{2.1}$$

$$\sigma_{s,a,\lambda} = \sum_{i=1}^{N_B} n_i b_{s,a,i,\lambda} \tag{2.2}$$

where $\sigma_{a,a,\lambda}$ is aerosol absorption coefficient, $\sigma_{s,a,\lambda}$ is aerosol scattering coefficient, n_i is the number concentration of aerosol of given size (particles cm $^{-3}$), N_B is number of aerosol sizes, $b_{a,a,i,\lambda}$ is effective absorption cross section of a single aerosol particle, and $b_{s,a,i,\lambda}$ is effective scattering cross section of a single aerosol particle.

The absorption and scattering coefficients are defined for spherical aerosol particles. The optical properties are integrated over the size distribution $n(r)$, and without normalization by the total volume or mass of particles, the scattering and absorption cross-sections are combined to obtain the scattering (α^{sca}) and absorption coefficients (α^{abs}) (unit m^{-1}) as follows (Boucher, 2015):

$$\begin{cases} \sigma^{sca} = \int_0^{\infty} \pi r^2 Q^{sca}(r) n(r) dr \\ \sigma^{abs} = \int_0^{\infty} \pi r^2 Q^{abs}(r) n(r) dr \end{cases} \tag{2.3}$$

where σ^{sca} is scattering coefficients, σ^{abs} is absorption coefficients, $n(r)$ is

size distribution, Q^{sca} is scattering cross-sections, and Q^{abs} is absorption cross-sections. Moreover, the extinction coefficient (σ^{ext}) is defined to encompass both absorption and scattering phenomena, thereby providing a comprehensive measure of the total attenuation of light by aerosol particles in the atmosphere as follow:

$$\sigma^{ext} = \sigma^{sca} + \sigma^{abs} \tag{2.4}$$

2.3.1.2. Lambert-Beer Law

Aerosols released into the atmosphere from both human activities (such as vehicles and industry) and natural events (like fires and sandstorms) impact human health, decrease visibility, and alter the Earth's radiation budget. AOD serves as a crucial parameter for assessing the impact of aerosols on the Earth's radiation balance and climate. Research indicates that atmospheric aerosols play a significant role in the Earth's radiative balance, both directly by scattering and absorbing solar radiation and indirectly by affecting cloud properties (Li et al., 2022). Additionally, aerosols influence global climate systems and are considered important in climate modeling and prediction due to their role in radiative forcing (IPCC, 2021). The radiative impact of aerosols in the atmosphere is indeed significant, as they alter the Earth's energy balance by scattering and absorbing sunlight. This scattering typically cools the climate by reflecting sunlight back into space, while absorption tends to warm it by retaining heat within the atmosphere. These interactions influence both the local and global climatic conditions and are crucial in the study of climate change. For instance, the scattering and absorbing properties of aerosols are crucial for understanding their direct radiative effects, which can directly change Earth’s surface and atmospheric temperature. These changes may lead to local

circulation alterations and influence convective activity (Myhre et al., 2013). Additionally, the aerosol scattering, absorption, and extinction coefficients, which describe these optical properties, are essential metrics in atmospheric science. The relationship between aerosol concentrations and their optical properties is often described by the Beer-Lambert Law. This law establishes a linear correlation between the concentration of a solution, its molar absorption coefficient, and the optical path length, which together determine the absorbance. This principle enables the determination of a solution's concentration by measuring its absorbance, highlighting a direct correlation between the amount of light absorbed and the properties of the solution through which it passes (Mamouei et al., 2021). For monochromatic light transmitted through a medium, with an incident intensity of I_0 and transmitted intensity of I (Fig. 2.2). The integral of the extinction coefficient (σ^{ext}) over the vertical column defines the AOD (τ_{ext}), following from the Lambert-Beer law:

$$ln\frac{I}{I_0} = -\int_{x_0}^{x} \sigma^{ext} dx = -\tau_{ext} \quad (2.5)$$

where I is transmitted light, I_0 is incident light, σ^{ext} is extinction coefficient, and τ_{ext} is AOD.

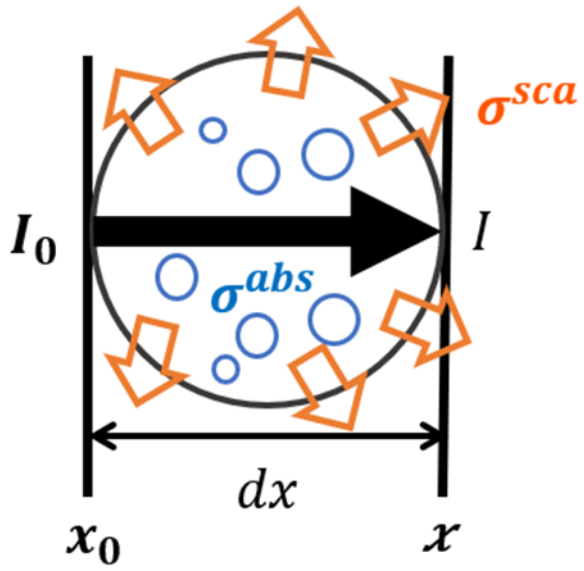

Fig. 2.2 Attenuation of the incident radiance I_0 due to absorption and scattering by a particle. I_0 is the initial light intensity, and I is the light intensity after transmission when passes through the particle at wavelength λ. The aerosol scattering and absorption are shown in orange arrows and blue circles, denoted by σ^{sca} (scattering coefficients) and σ^{abs} (absorption coefficients).

2.3.2. MODIS DT-ocean algorithm

The original MODIS file, called Level 0 (L0), represents raw sensor counts, which are organized into scans as Level 1A (L1A). Level 1B (L1B) contains calibrated data that provides geolocated radiances or reflectance. These L1B data identified as product MOD02 and MOD03 for Terra and MYD02 and MYD03 for Aqua (Levy et al., 2009). These L1B data serve as inputs for the DT algorithm, corrected for gaseous absorption and molecular scattering (Levy et al., 2013). Level 2 (L2) includes derived geophysical products in 5-minute granules, while Level 3 (L3) provides aggregated daily or monthly statistics on a 1°×1° latitude/longitude grid. Data processing follows a linear sequence (L0 → L1A → L1B → L2 → L3), with some L2 products used as inputs for others. All MODIS data are stored in HDF format and are labeled as MODXX (Terra) or MYDXX (Aqua).

The DT algorithm was designed to utilize the distinctive reflectance properties of aerosols and their interaction with "dark" surfaces in the blue channel (470 nm) and red channel (670 nm) of visible and NIR spectral range (2100 nm). Over oceans, the surface reflectance is minimal in these wavelengths, providing strong contrast for aerosol detection. The core assumptions of the DT algorithm include surface reflectance and aerosol signals have distinct spectral patterns, enabling differentiation and aerosol optical properties and size distributions are modeled within predefined LUTs.

2.3.2.1. Input data

The DT-ocean algorithm is a robust method for retrieving aerosol properties over ocean surfaces, utilizing the unique optical characteristics of aerosols and the inherently low reflectance of ocean surfaces in visible and SWIR wavelengths. The process begins with the preparation of input data, where MODIS L1B radiances are calibrated and geolocated to derive reflectance (Levy et al., 2013). These reflectance ($\rho\lambda$) are computed as follow (Levy et al., 2007) :

$$\rho\lambda = \frac{\pi L_\lambda}{F_{0,\lambda}\cos(\theta_0)} \tag{2.6}$$

where L_λ represents the measured spectral radiance, $F_{0,\lambda}$ is the solar irradiance, and θ_0 is the solar zenith angle. To improve the signal-to-noise ratio and reduce variability, the data are spatially aggregated from their native 1×1 km resolution into 10×10 km grids, which consist of 20×20 pixels. This aggregation not only ensures statistical robustness but also balances spatial coverage and retrieval precision. Ancillary data, such as atmospheric

profiles of water vapor and ozone from the National Centers for Environmental Prediction (NCEP) GDAS and MODIS cloud masks (MOD35_L2), are integrated to support the retrieval process.

2.3.2.2. Cloud masking

Cloud masking is implemented using a spatial variability approach, where the algorithm distinguishes clouds from aerosols based on their differences in spatial reflectance patterns. Clouds typically exhibit higher spatial variability in reflectance over small scales compared to the more uniform reflectance of aerosols. This distinction is quantified by calculating the standard deviation of reflectance over 3×3-pixel blocks (3×3-STD) and applying a threshold in VIS and SWIR channels (Martins et al.,2002) to separate clouds from aerosols.

For each 500 m resolution pixel, the algorithm evaluates two tests to determine its cloud status. One is VIS test (Levy et al., 2013), which include the reflectance at 0.47 μm ($\rho_{0.47}$) the standard deviation of reflectance across a 3×3-pixel box at 0.55 μm ($\sigma_{0.55}$), and the reflectance ratio of 0.47 μm to 0.65 μm ($\frac{\rho_{0.47}}{\rho_{0.65}}$). A pixel is classified as “cloudy” if it exhibits high reflectance ($\rho_{0.47} > 0.4$), significant spatial variability ($\sigma_{0.55} > 0.0025$), or does not display the spectral signature of brown dust ($\frac{\rho_{0.47}}{\rho_{0.65}} < 0.75$).

To detect high-altitude cirrus clouds, the algorithm applies SWIR tests (Levy et al., 2013) using data at 1 km resolution. These tests analyze the absolute reflectance at 1.38 μm ($\rho_{1.38}$) and its ratio to the reflectance at 1.24 μm ($\rho_{1.38}$ /$\rho_{1.24}$) to identify cirrus-specific spectral features, as described by Gao et al. (2002). The 1 km pixel (four 500m pixels) is considered as “cloudy” if $\rho_{1.38} > 0.03$). If ($0.005 < \rho_{1.38} \leq 0.03$), ratio test is applied. If ($\frac{\rho_{1.38}}{\rho_{1.24}} > 0.30$), the pixel is also considered cloudy. If the pixel is determined to be "not cloudy," the

algorithm performs an additional check for potential residual cirrus. Specifically, if ($0.005 < \rho_{1.38} \leq 0.03$ and $\frac{0.10 < \rho_{1.38}}{\rho_{1.24}} \leq 0.30$ and $\rho_{0.65} > 1.5\rho_{0.65}^{Rayleigh}$, the presence of cirrus is classified as ambiguous. In this situation, the pixel is retained, but the quality assurance confidence (QAC) value for the entire MODIS retrieval box is reduced.

Due to high water vapor levels over tropical oceans, the internal SWIR cirrus detection algorithm may fail to mask high and thin cirrus clouds. Thermal infrared (IR) tests (Levy et al., 2013) from the upstream MODIS cloud mask file (MxD35_L2) are utilized: the "Thin Cirrus (IR) Test" (Bit 11), the "High Cloud (6.7 μm) Test" (Bit 15), and the "IR Temperature Difference Test" (Bit 18). If any of these IR tests indicate cloud presence, a 2×2 grid of 500-meter pixels (corresponding to one 1-km MxD35 pixel) is marked as "cloudy," excluding it from aerosol retrieval. However, during the C6 of MODIS, the Bit 18 test was relaxed to reduce false cirrus detections. While this approach aimed to avoid targeting ambiguous cirrus clouds for cloud retrieval, it also led to increased cirrus contamination in aerosol retrieval.

The combined effect of a weakened MxD35 test and a strengthened internal NIR test is a slight reduction in aerosol coverage over mid-latitude oceans compared to Collection 5 (C5). As shown in a granule observed over the Pacific by Aqua on January 1, 2010 (Fig. 2.3), the AOD magnitude decreases slightly over the western tropical Pacific. Conversely, AOD increases slightly in regions with heavy aerosol plumes, such as dust from the Sahara, off Siberia's coast, and volcanic emissions from Hawaii.

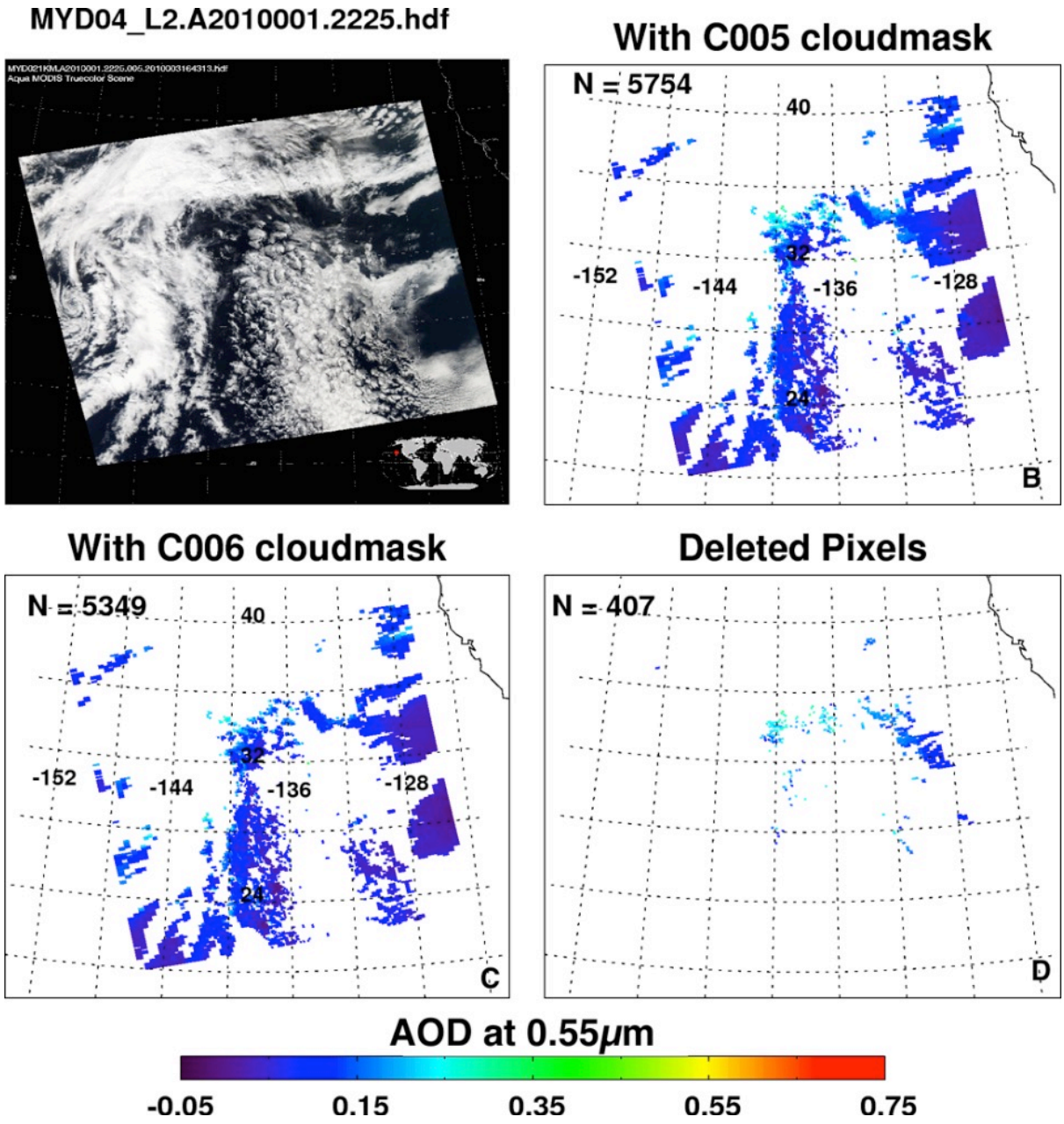

Fig. 2.3 Granule observed over the Pacific Ocean by MODIS/Aqua on January 1, 2010, at 22:25 UTC. The top left panel shows a true-color (RGB) image of the scene, sourced from modis-atmos.gsfc.nasa.gov. Panels (b) and (c) present the retrieved high-quality AOD at 0.55 μm (QAC ≥ 1 over ocean) without and with the updated 1.38 μm cloud mask test, respectively. Panel (d) highlights cirrus-contaminated pixels removed over the ocean. Cited from Levy et. (2013).

2.3.2.3. Sediment masking

For sediment masking, the algorithm uses reflectance thresholds to exclude shallow water regions and areas influenced by bottom sediments. These thresholds are informed by the distinctive optical properties of sediments, which typically exhibit higher reflectance than clear water. In addition, the process incorporates geographic land/sea masks to differentiate between oceanic and terrestrial regions. Supplementary tests, such as verifying the spectral consistency of aerosol signals, further refine the sediment masking process.

The integration of these methods ensures that only pixels representing clear atmospheric and surface conditions are used in the aerosol retrieval process. The selected pixels are then subjected to corrections for atmospheric gas absorption (e.g., water vapor, ozone), ensuring that the final reflectance values accurately represent the conditions required for reliable AOD inversion. By minimizing residual contamination from clouds and sediments, the algorithm achieves a robust framework for global aerosol monitoring.

2.3.2.4. Spectral reflectance fitting

The next phase involves comparing observed TOA reflectance with modeled reflectance stored in LUTs. These LUTs contain precomputed radiative transfer solutions that simulate atmospheric and surface optical properties under various conditions of aerosol types, concentrations, and viewing geometries. The modeled TOA reflectance (Levy et al., 2007) is expressed as:

$$\rho_{mod,\lambda} = \rho_{atm,\lambda} + T_{\lambda}\rho_{surf,\lambda} \tag{2.7}$$

where is the atmospheric path reflectance, T_{λ} is total transmittance, and $\rho_{surf,\lambda}$ is the surface reflectance. Nine aerosol models are employed, each

representing a distinct aerosol type and size distribution, categorized into fine and coarse modes. Observed reflectance at six wavelengths (0.55, 0.65, 0.86, 1.24, 1.63, and 2.11 μm) are matched to these LUTs, and the retrieval process involves an inversion of the spectral fitting. The algorithm iteratively adjusts AOD and fine mode fraction (FMF) to minimize the residual error (Remer et al., 2005 and Levy et al., 2007), defined as:

$$\epsilon = \sum_{\lambda}\left(\rho_{obs,\lambda} - \rho_{mod,\lambda}\right)^2 \quad (2.8)$$

where ϵ is squares spectral fitting error, $\rho_{obs,\lambda}$ is spectral reflectance of observations, and $\rho_{mod,\lambda}$ is modeled TOA reflectance. This process identifies the optimal combination of aerosol models and parameters that best represent the observed reflectance. The retrieved parameters include the total AOD at 0.55 μm, which quantifies the column-integrated aerosol extinction, and the FMF, indicating the proportion of AOD attributable to fine-mode aerosols.

2.3.2.5. Quality control and validation

The algorithm incorporates a rigorous quality control mechanism to assess the reliability of each retrieval. Quality Assurance (QA) confidence flags are assigned based on the residual error and consistency of the spectral fitting. The accuracy of the retrievals is validated against ground-based AERONET observations, ensuring that the retrieved AOD typically falls within the expected uncertainty of $\Delta\tau = \pm 0.03 \pm 0.05\tau$ over ocean (Remer et al., 2005). Validated products are then output at resolutions of 10×10 km for standard global coverage and 3×3 km for areas requiring higher spatial detail.

The DT algorithm has been refined over successive MODIS Collection 6, with improvements in cloud masking, aerosol modeling, and resolution. Its strengths

include high accuracy in retrieving AOD, with an uncertainty of $\pm(0.03 + 5\%\tau)$ over oceans and $\pm(0.05 + 15\%\tau)$ over land (Levy et al., 2013). Global daily coverage, supporting applications in climate research, air quality monitoring, and atmospheric correction for other remote sensing products.

2.3.2.6. Wind speed dependence over ocean

This section highlights improvements in aerosol retrieval accuracy over oceans by incorporating wind speed dependence into the MODIS DT-ocean algorithm. Previously, the C5 algorithm assumed a constant wind speed of 6 m/s, which led to systematic biases globally, particularly in regions with significant wind variability. Studies, such as those by Zhang and Reid (2010) and Kleidman et al. (2012), identified errors related to incorrect wind speed assumptions, especially near glint regions where the surface reflects sunlight directly to the sensor.

To address these issues, the C6 algorithm introduced wind speed variability into the retrieval process. It uses wind speed data from NCEP analyses and incorporates a dynamic interpolation step in the LUT to account for actual wind speeds ranging from 2 m/s to 14 m/s. The updates help capture the effects of wind-driven surface roughness, foam, and glint patterns. The new approach significantly reduces global AOD biases over oceans, particularly in high-wind regions like the Southern Ocean and near glint zones. By diffusing glitter patterns and adapting to local wind conditions, the C6 algorithm improves the accuracy and robustness of MODIS oceanic aerosol retrievals.

2.4. Future satellite observation plans

Future satellite observation plans aim to enhance our understanding of aerosols and their impact on the Earth system. Japan's major Earth observation satellites, such as the Global Change Observation Mission (GCOM) series, GOSAT series, Himawari series, and Advanced Land Observing Satellite (ALOS) series, will play a pivotal role in continuing Earth observations. Notably, the successful launch of the ALOS-4 satellite on July 1, 2024, represents a significant advancement in Earth monitoring. ALOS-4, equipped with advanced synthetic aperture radar (SAR) technology, provides high-resolution data on land deformation, vegetation, and disaster monitoring, further enriching the global satellite observation network. These satellites collectively contribute critical data on atmospheric composition, climate variability, and land-ocean interactions, aiding both scientific research and societal applications.

Complementing satellite observations, advanced methodologies like numerical simulations and data science techniques will be utilized to analyze and integrate diverse datasets. These approaches will enable a more comprehensive understanding of aerosol behavior and their interactions with climate and air quality. For example, integrating high-resolution satellite data with climate models can improve predictions of aerosol transport and their effects on regional weather patterns.

Additionally, future missions are expected to incorporate advanced instruments for higher-resolution and multi-dimensional observations. Such developments will further improve the detection and characterization of aerosols, including their vertical distribution, optical properties, and sources. By leveraging these advancements, including the enhanced capabilities of satellites like ALOS-4, researchers aim to address pressing environmental challenges and contribute to a safer and more sustainable Earth.

Chapter 3. Reanalysis and climate model data

This chapter provides a comprehensive overview of the reanalysis dataset Modern-Era Retrospective analysis for Research and Applications, Version 2 (MERRA-2) and the climate model dataset The Spectral Radiation-Transport Model for Aerosol Species, version 6.1.0 (SPRINTARS) utilized in this study. It introduces the theoretical foundations of AOD, including the Beer-Lambert Law, based on key texts by Bohren et al. (2008) and Boucher et al. (2015). The chapter further introduced the methodologies of AOD retrieval in each dataset in section 3.1.3 and section 3.2.3. And data sources, and processing techniques applied in the reanalysis and climate model, with specific focus on aerosol transport, assimilation processes, and AOD calculations.

3.1. Reanalysis datasets (MERRA-2)

MERRA-2, developed by NASA's Global Modeling and Assimilation Office (GMAO), combines observational data from various sources into a global atmospheric reanalysis that provides a comprehensive and consistent record of Earth's atmosphere. This MERRA-2 dataset was created using the Goddard Earth Observing System Model, Version 5 (GEOS-5), and enhanced by the Goddard Chemistry Aerosol Radiation and Transport model (GOCART), effectively simulates complex atmospheric processes (Chin et al., 2002; Gelaro et al., 2017). The spatial resolution of MERRA-2 is 0.625°×0.5° (Bosilovich et al., 2016).

The MERRA-2 system generates 3-hourly analyses and structured data outputs, including both directly observable parameters and complex aerosol diagnostics that are challenging to observe on a global scale. These outputs have a wide range of applications, from air quality predictions to research on

interactions between aerosols and climate or weather (Bocquet et al., 2015). The system utilizes an analysis splitting technique (Randles et al., 2017) for assimilating AOD at 550 nm, beginning with a two-dimensional analysis based on error covariances from innovation data. Subsequently, these horizontal increments are extended vertically and across different species using an ensemble approach. AOD data are derived from several platforms: 1) reflectance from AVHRR (Advanced Very High-Resolution Radiometer) covering ocean-only regions from 1979–2002 (Heidinger et al., 2002), 2) reflectance from MODIS on the Terra (since 2000) and Aqua (since 2002) (Table 3.1) satellites (Remer et al., 2005; Levy et al., 2007), 3) AOD retrievals from MISR for bright, desert regions from 2000–2014 (Kahn et al., 2005), and 4) direct AOD measurements from the ground-based AERONET from 1999–2014 (Holben et al., 1998). Particularly after 2002, MODIS contributes the majority of AOD observations used in MERRA-2, complemented by AVHRR reflectance prior to 2000. Both MODIS and AVHRR derive AOD from cloud-cleared reflectance, employing a neural net process trained with AERONET (Aerosol Robotics Network) data (Randles et al., 2017).

Since MERRA-2 incorporates observation data from various platforms, including MODIS sensors aboard the Terra and Aqua satellites starting from 2003 (Fig. 3.1), a well correspondence between MERRA-2 and MODIS AODs is expected (Che et al., 2019). MODIS provides clear-sky data and filters certain values (such as clouds) when retrieving AOD. Considering limitations in the amount of data and continuity, the AOD data from the MERRA-2 dataset was utilized in this study. Specifically, MERRA-2 AOD data for various components, including sea salt AOD, sulfate AOD, BC (Black Carbon) AOD, OC (Organic Carbon) AOD, and dust AOD were also utilized in this study. Additionally, to examine the spatial distribution and trend of AOD data, we adjusted the MODIS AOD data resolution to match the resolution of MERRA-2, which is 0.625°×0.5°

by using the "nearest neighbor method". Fig. 3.2 shows the time series of analyzed AOD from the MERRA-2 area averaged over (a) South and East Asia, (b) northern Africa, and (c) the Amazon basin in South America. The contribution of each aerosol species to the total AOD is indicated by the colored shading. The seasonal cycles of dust and biomass burning (carbonaceous) AOD are apparent. Large increases in sulfate aerosol occur in all regions after the El Chichón (1982) and Mount Pinatubo (1991) volcanic eruptions. The analysis captures high carbonaceous aerosol associated with the 2003 Siberian fires and the increasing trend in AOD between the late 1990s and the present (Fig. 3.2 (a)).

The MERRA-2 data were acquired from the Giovanni NASA website (https://giovanni.gsfc.nasa.gov/giovanni/). Monthly data on AOD at 550 nm, sea salt AOD at 550 nm, wind speed (m/s), and direction at 500 hPa were analyzed for the period 2003 to 2023 in this study.

Table 3.1 MERRA-2 AOD Observing System. Cited from Randles et al. (2016).

Sensor	Temporal Coverage	Description
AVHRR NNR[a]	1980 – August 2002	PATMOS-x radiances over ocean only (PM orbit)
AERONET[b,c]	Station dependent (1999 – October 2014)	AOD from land station network
Multi-angle Imaging Spectro Radiometer (MISR)[c]	February 2000 – June 2014	AOD over bright land surfaces only (albedo > 0.15)
MODIS Terra NNR[a]	March 2000 – onwards (NRT[d])	Collection 5 "Dark Target" land and ocean radiances (AM orbit)
MODIS Aqua NNR[a]	August 2002 – onwards (NRT[d])	Collection 5 "Dark Target" land and ocean radiances (PM orbit)

[a]NNR refers to Neural Net Retrieval algorithm that computes AERONET-calibrated AOD from radiances.

[b]AERONET AOD is converted to 550 nm using an Angström-based. interpolation and AOD reported at adjacent channels (500 and 675, typically).

[c]We do not bias-correct AERONET or MISR AOD.

[d]MODIS data is available in Near Real Time (NRT).

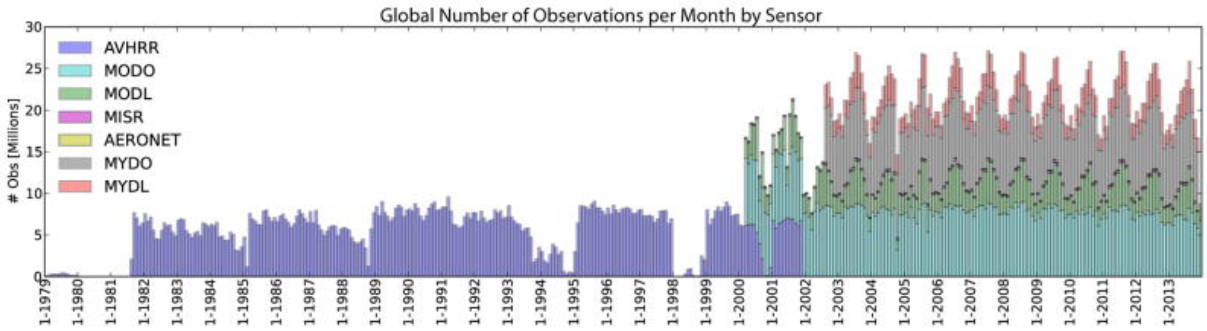

Fig. 3.1 The total global monthly number of observations from various sources, where NNR denotes the bias-corrected neural net retrieved Aerosol Optical Depth (AOD). It includes data from AVHRR NNR, MODIS Terra over land (MODL NNR) and ocean (MODO NNR), MODIS Aqua over land (MYDL NNR) and ocean (MYDO NNR), MISR over bright surfaces such as deserts, and AERONET. Cited from Randles et al. (2016).

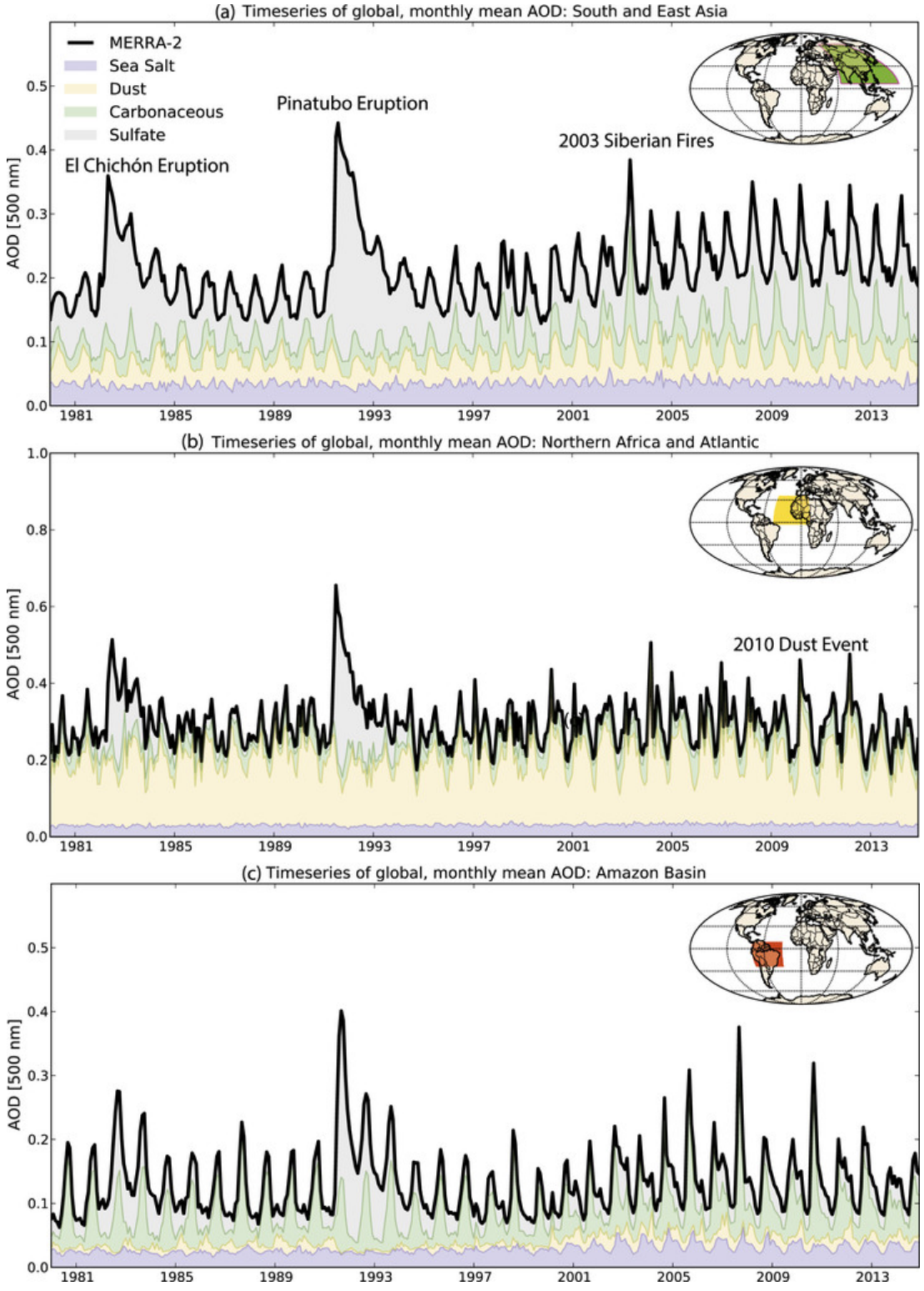

Fig. 3.2 Time series of area-weighted AOD from the MERRA-2 over major aerosol source regions: (a) South and East Asia (5°–55°N, 65°–160°W), (b) northern Africa (2.5°S–30°N, 45°W–15°E), and (c) the Amazon basin in South America (20°S–7.5°N, 80°–30°W). The total AOD (thick black line) is the contributions from sea salt (blue), dust (yellow), carbonaceous (black), organic carbon (green), and sulfate (gray) AOD. Cited from Gelaro et al. (2017).

3.1.1. Aerosol module

The GOCART (Chin et al., 2002; Colarco et al., 2010) aerosol module in MERRA-2 serves as a critical component for simulating aerosols and their interactions within the Earth system. GOCART treats several types of aerosols, including dust, sea salt, sulfate, black carbon, and organic carbon, with sources ranging from wind-driven emissions and fossil fuel combustion to biomass burning and volcanic activity. Secondary aerosols, such as sulfate, are produced through chemical processes like the oxidation of sulfur dioxide. The module divides the particle size distributions of dust and sea salt into five distinct bins (Colarco et al., 2010) and tracks other species in both hydrophobic and hydrophilic modes. Aerosol removal mechanisms include dry deposition, wet scavenging, and convective processes, while hygroscopic growth, driven by ambient humidity, is incorporated into calculations of particle deposition and optical properties. As radiatively active particles, these aerosols influence energy balance, with their optical properties derived from Mie-theory. GOCART uses observationally constrained emissions datasets, such as AeroCom and QFED, integrated seamlessly into the GEOS-5 system for online aerosol simulations. It has been widely applied in Observing System Simulation Experiments (OSSEs), field campaign support (e.g., ARCTAS and SEAC4RS), and studies of aerosol-climate interactions and environmental feedback, providing a robust framework for understanding aerosol processes and their global impacts.

3.1.2. Emission datasets

MERRA-2 incorporates numerous satellite observation datasets. Table 3.2 summarizes the full set of input observations assimilated in MERRA-2, with detailed descriptions available in McCarty et al. (2016).

Table 3.3 provides an overview of the emission sources for various aerosol

types modeled by the GOCART aerosol module in MERRA-2. Temporal variations in emissions, both annual and monthly, are handled through linear interpolation, while the datasets are adjusted to match the native model grid using conservative re-gridding techniques.

Emissions are categorized into natural sources, biomass burning, and anthropogenic activities. Natural emissions include dust and sea salt, both driven by wind speed, and volcanic sulfur dioxide (SO_2), which is injected at varying altitudes depending on eruption intensity (Diehl et al., 2012). Since MERRA-2 does not include eruptive volcanic activity after 2010, this study does not account for the impact of volcanic eruptions when using MERRA-2 data. Biogenic emissions, such as organic aerosols from vegetation and marine dimethyl sulfide (DMS), contribute to organic carbon and sulfate aerosols. Biomass burning emissions are time-resolved differently across periods, with monthly means used before 2010 and daily variations, thereafter, capturing intense vertical mixing within the planetary boundary layer.

Anthropogenic emissions, derived from datasets like EDGAR and AeroCom, include SO_2, primary sulfate, black carbon, and organic carbon from industrial, residential, and transportation sectors. Following 2008, anthropogenic SO_2 emissions are assumed to remain constant, with 2008 emission levels being reused (European Comission, 2011). These emissions are spatially and temporally detailed, with processes such as linear interpolation ensuring compatibility with the model's native grid. This section highlights the integration of comprehensive datasets and methodologies to accurately represent aerosol emissions and their variability over time and space in the MERRA-2 system.

Tabel. 3.2 Observation data and sources assimilated in MERRA-2. Bold font indicates observation types that were not absorbed by MERRA but were used in MERRA-2. Cited from Gelaro et al. (2017).

Data type	MERRA-2 dates	Source
	Conventional	
Raob, pibal, and dropsonde	1 Jan 1980–present	See Rienecker et al. (2011)
AIREP, PIREP, ASDAR, and MDCRS aircraft	1 Jan 1980–present	NCEP, ECMWF, and JMA
PAOB	1 Jan 1980–17 Aug 2010	BoM
Surface land	1 Jan 1980–present	NCEP
Surface ship and buoy	1 Jan 1980–present	ICOADS
	Ground-based remotely sensed	
Wind profiler	14 May 1992–present	UCAR and NCEP
NEXRAD VAD wind	16 Jun 1997–present	NCEP
	Satellite-derived wind	
GMS, MTSAT, and Himawari atmospheric motion vector	1 Jan 1980–present	NCEP and JMA
Meteosat atmospheric motion vector	1 Jan 1980–present	NCEP and EUMETSAT
GOES atmospheric motion vector	1 Jan 1980–present	NCEP
AVHRR atmospheric motion vector	**1 Oct 1982–present**	**CIMSS**
SSM/I surface wind speed	9 Jul 1987–4 Nov 2009	RSS
ERS-1 surface wind vector	5 Aug 1991–21 May 1996	ESA
ERS-2 surface wind vector	19 Mar 1996–29 Mar 2011	ESA
QuikSCAT surface wind vector	19 Jul 1999–22 Nov 2009	JPL
MODIS atmospheric motion vector	2 Jul 2002–present	CIMSS and NCEP
SSMIS surface wind speed	**23 Oct 2003–29 Oct 2013**	**RSS**
WindSat surface wind vector	**13 Aug 2007–4 Aug 2012**	**NCEP**
ASCAT surface wind vector	**15 Sep 2008–present**	**NCEP**
	Satellite retrieved	
SBUV and SBUV/2 ozone	1 Jan 1980–31 Sep 2004	NASA GES DISC
SSM/I rain rate	9 Jul 1987–16 Sep 2009	NASA GES DISC
TMI rain rate	1 Jan 1998–8 Apr 2015	NASA GES DISC
MLS temperature	**13 Aug 2004–present**	**NASA GES DISC**
MLS ozone	**1 Oct 2004–present**	**NASA GES DISC**
OMI total column ozone	**1 Oct 2004–present**	**NASA GES DISC**
	Radio occultation	
GPSRO bending angle	**14 July 2004–present**	**NCAR and NCEP**
	Satellite radiance	
TOVS	1 Jan 1980–10 Oct 2006	NCAR and NESDIS
SSM/I	9 Jul 1987–4 Nov 2009	RSS
ATOVS (*NOAA-15*, *NOAA-16*, *NOAA-17*, and *NOAA-18*)	21 Jul 1998–present	NESDIS
GOES sounder (*GOES-8*, *GOES-10*, *GOES-11*, and *GOES-12* low resolution)	24 Apr 2001–31 Mar 2007	NCEP and NESDIS
AMSU-A (*Aqua*)	1 Sep 2002–present	NASA GES DISC
AIRS	1 Sep 2002–present	NASA GES DISC
GOES sounder (*GOES-11*, *GOES-12*, *GOES-13*, and *GOES-15* full resolution)	**1 Apr 2007–present**	**NESDIS**
ATOVS (*NOAA-19*, *MetOp-A*, and *MetOp-B*)	**21 May 2007–present**	**NESDIS**
IASI	**17 Sep 2008–present**	**NESDIS**
ATMS	**16 Nov 2011–present**	**NESDIS**
SEVIRI	**15 Feb 2012–present**	**NESDIS**
CrIS	**7 Apr 2012–present**	**NESDIS**

Tabel. 3.3 Emissions dataset used in MERRA-2. Cited from Randles et al. (2016).

Aerosol Type	Source	Temporal Resolution	Spatial Resolution[a,b]
Dust	Wind-driven emissions w/Ginoux et al. (2001) static topographic depression map	Model	0.3125°× 0.25°[c]
Sea Salt	Wind-driven emissions	Model	Model
Volcanic (SO_2)	AeroCom Phase II (HCA0 v2; Diehl et al., 2012)	Daily degassing (1980 – onwards) and daily eruptive (1980 – 2010)	Point-sources
Biogenic terpene	Guenther et al. (1995)	Monthly-mean climatology	2°× 2.5°
Di-Methyl Sulfide (DMS)	Lana et al. (2011)	Monthly-mean climatology	1°× 1°
Biomass Burning (SO_2, SO_4, POM, and BC)	scaled RETROv2 (Duncan et al., 2003)	Monthly-varying (1980 – 1996)	0.3125°× 0.25°
	scaled GFEDv3.1 (Randerson et al., 2006)	Monthly-varying (1997 – 2010)	0.3125°× 0.25°
	QFED 2.4-r6 (Darmenov and da Silva, 2015)	Daily-varying (2010 – onwards)	0.3125°× 0.25°
Anthropogenic SO_2	EDGARv4.2 (Energy + Non-Energy) (European Comission, 2011)	Annually-varying (1980 – 2008)	0.1°× 0.1°
Anthropogenic SO_4, POM, and BC	AeroCom Phase II (HCA0 v1; Diehl et al., 2012)	Annually-varying (1980 – 2006)	1°× 1°
International Ships SO_2	EDGARv4.1 (European Commission, 2010)	Annually-varying (1980 – 2005)	1°× 1°
International Ships SO_4, POM, and BC	AeroCom Phase II (HCA0 v1; Diehl et al., 2012)	Annually-varying (1980 – 2007)	1°× 1°
Aircraft SO_2	AeroCom Phase II (HCA0 v1; Diehl et al., 2012)	Monthly-varying (1980 – 2006)	1°× 1.25°× 72-levels

[a] Model = MERRA-2 time-step of 30 minutes with spatial resolution of 0.5° latitude × 0.625° longitude.
[b] latitude × longitude
[c] Resolution is for source map (Ginoux et al., 2001); wind-driven emissions at model time-step and grid.

3.1.3. Aerosol assimilation

The aerosol assimilation in MERRA-2 integrates observations and modeling to improve aerosol representations in the reanalysis system. This process is carried out using the Goddard Aerosol Assimilation System (GAAS), which constrains simulated AOD based on observed data (Randles et al., 2016). Observations from various sources, including MODIS, MISR, AVHRR, and AERONET, are assimilated after bias correction using a neural net retrieval method. The assimilation operates on a cubed-sphere grid at eight synoptic times per day, utilizing a two-step process: a two-dimensional AOD analysis and subsequent three-dimensional aerosol mass mixing ratio adjustment. Local Displacement Ensembles (LDEs) are used to address errors in aerosol plume locations, enhancing the vertical and spatial distribution of aerosol species.

The system accounts for observation and model errors, with quality checks to ensure data consistency. Observations are processed to reduce biases and standardize retrievals across multiple sensors. Innovation statistics, such as observation minus forecast (O−F) and observation minus analysis (O−A), are

evaluated to assess the assimilation's performance, showing improvements in aerosol representation after assimilation

In the GEOS-5/GOCART model, AOD is calculated as a column-integrated property using the following formula:

$$\mathrm{AOD} = \sum_{z,i} xi \times b_{ext,i}(RH) \times \partial_z \tag{3.1}$$

where xi represents the concentration of 15 aerosol species, including dust (in 5 size bins), sea salt (in 5 size bins), hydrophobic and hydrophilic BC, OC, and SO_4^{2-}. The extinction coefficient $b_{ext,i}(RH)$ is species-specific and derived from Mie theory, varying with relative humidity (RH), which affects the optical properties of aerosols. ∂_z is the vertical layer thickness, ensuring proper integration of aerosol concentrations and extinction coefficients throughout the atmospheric column. The assimilation in MERRA-2 constrains the simulated AOD based on the forecasted aerosol speciation and vertical distribution. However, LDEs may slightly affect the strict validity of the calculation.

Firstly, the AOD analysis in GEOS-5 is conducted using analysis splitting. Every 3 hours, a 2-D analysis of AOD is performed, utilizing error covariances derived from innovation data based on the maximum-likelihood method of Dee and da Silva (1999). This process combines observational data with model forecasts to adjust the forecasted AOD by incorporating observed AOD and their associated uncertainties through a two-dimensional analysis algorithm. It is expressed as:

$$\tau^a = Hx^a = H(x^f + \delta x^a) = \tau^f + \delta\tau^a$$

$$= \tau^f + HP^fH^T\,(HP^fH^T + R)^{-1}(\tau^o - Hx^f) \tag{3.2}$$

where τ^a is the analyzed AOD, τ^f is the forecast AOD, and τ^o is the observed AOD. The observation operator H translates aerosol mass into AOD, while P^f and R represent the background and observation error covariance matrices, respectively.

Secondly, to project the analyzed 2D AOD increments ($\delta\tau^a$) into 3D aerosol concentration increments (δx^a), the algorithm uses background error covariance relationships. The relationship is expressed as:

$$\delta x^a = P^f H^T \left(HP^f H^T\right)^{-1} \delta\tau^a \tag{3.3}$$

where δx^a is the adjustment made to the aerosol species concentrations. This method ensures that the increments are consistent with the vertical and species-specific distribution of aerosols in the model. By incorporating covariance operators, the approach effectively distributes the horizontal AOD increments into vertical layers and across different aerosol species, accounting for their modeled relationships.

Finally, the LDE (Buchard et al., 2015) further simplifies the computational demands of error covariance modeling. It generates realistic vertical and horizontal error structures by using ensemble perturbations of aerosol concentrations (*X*) and AOD (*Y*). These perturbations are weighted by a diagonal matrix D*D*, and the analysis increment is calculated as:

$$\delta x^a = \mathrm{XDY^T}(YDY^T)^{-1} \delta\tau^a \tag{3.4}$$

$$\mathrm{X} = (x_1, x_2 \ldots\ldots x_E)$$

$$\mathrm{Y} = \mathrm{HX} = (\tau_1, \tau_1 \ldots\ldots \tau_E)$$

where X represents a matrix of dimensions $n_q \times n_E$. n_q is the product of the number of aerosol concentration tracers and the vertical levels, and n_E denotes the total number of ensemble perturbations for a given column. This ensemble-based approach models aerosol forecast errors as local displacements of aerosol plumes, ensuring computational efficiency while maintaining physical plausibility. The LDE method is particularly valuable in assimilating complex, spatially variable aerosol distributions in the MERRA-2 system.

3.1.4. Assimilation errors

The primary errors in MERRA-2's AOD assimilation arise from observational biases, forecast errors, and vertical distribution uncertainties.

Satellite-derived AOD products from sensors like AVHRR, MODIS, and AERONET exhibit systematic biases due to cloud contamination, surface reflectance uncertainties, and calibration issues. While Neural Net Retrievals (NNR) reduce these biases, residual errors persist, particularly in regions with complex aerosol sources or bright surfaces. Overestimation of sea-salt AOD in oceanic regions and underestimation in biomass-burning regions highlight such issues.

Background forecasts often underestimate AOD in high-loading regions, such as deserts and biomass-burning zones, due to limitations in emission inventories and transport modeling.

The system effectively constrains column-integrated AOD but lacks direct constraints on vertical aerosol distributions, leading to potential errors in aerosol mass and radiative properties. However, biases remain in specific regions, particularly over land. MERRA-2 is globally consistent and accurate for total column AOD analysis, making it a valuable resource for climate and air quality studies.

3.2. Numerical simulations (SPRINTARS)

SPRINTARS is a sophisticated numerical model designed to simulate the impact of atmospheric aerosols on global climate systems and air quality. The SPRINTARS has been developed by the Climate Change Science Section, Research Institute for Applied Mechanics, Kyushu University. SPRINTARS effectively models the complexities of both natural and anthropogenic aerosols, including black carbon, organic matter, sulfate, soil dust, and sea salt, which are categorized into SPM, PM_{10}, and $PM_{2.5}$ (Takemura et al., 2000, 2002, 2005).

SPRINTARS is integrated into the MIROC atmosphere-ocean general circulation model, which is a collaborative effort by the Atmosphere and Ocean Research Institute (AORI) at the University of Tokyo, the National Institute for Environmental Studies, and the Japan Agency for Marine-Earth Science and Technology (JAMSTEC). It also collaborates with the global cloud-resolving model, NICAM, enhancing its capability to simulate detailed climatic interactions.

This advanced numerical model is suitable for simulating AOD, particularly noting its effectiveness in complex emission source regions like East Asia. The reliability and precision of SPRINTARS in simulating AOD and other aerosol characteristics have been validated against satellite data and ground observations, ensuring their accuracy in revealing atmospheric states (Takemura et al., 2005). Incorporated into the MIROC general circulation model through collaborations with the University of Tokyo and other Japanese research institutes, SPRINTARS extends its utility by modeling interactions between aerosols and climate systems, further detailed in its ability to handle aerosol dynamics such as advection, diffusion, and deposition processes. This comprehensive approach not only enhances our understanding of aerosol impacts on global climate but also facilitates studies in significant emission areas like East Asia, providing insights into regional and global climate alterations due to aerosols (Takemura et al., 2000).

The SPRINTARS model is particularly useful for studying regions with significant aerosol emissions, such as East Asia, where it describes the effects of aerosols on regional and global climates. In this study, the SPRINTARS AOD at 550 nm and sea salt AOD at 550 nm data were utilized for the period from 2003 to 2021. The original resolution of the SPRINTARS AOD data at 550 nm (0.5625°×0.5625°) has been adjusted to match the MERRA-2 resolution (0.625°×0.5°) using the nearest neighbor method.

3.2.1. Emission data source

SPRINTARS incorporates both natural and anthropogenic emission data. Meteorological inputs are integrated with emission datasets to simulate aerosol emissions and transport. The aerosol transport model uses meteorological constraints from the NCEP/NCAR reanalysis data, which include wind velocities, temperature, and specific humidity to nudge the AGCM. Diffusion coefficients, precipitation flux, and cloud water are generated every two hours by running the AGCM with 1990 NCEP/NCAR reanalysis data, selected for direct comparison with AVHRR satellite data from the same year. For example, soil dust emissions are calculated using wind speed, soil moisture, snow cover, and LAI, with land use classifications (Matthews, 1983) determining emission regions. Soil dust and sea-salt emissions depend on 10-meter wind velocity, while diffusion and precipitation processes are parameterized based on the reanalysis-derived atmospheric state. Wind velocity at 10 meters, essential for evaluating soil dust and sea-salt aerosol emissions, is derived from the AGCM's lowest layer (approximately 50 meters above ground) using Monin-Obukhov similarity theory, adjusted for stability conditions with the Richardson number (Louis, 1979). Small-scale dry convection, characterized by large sensible heat fluxes, improve surface wind dynamics.

Carbonaceous aerosols include organic carbon (OC) and black carbon (BC)

from biomass burning, fossil fuel combustion, and biogenic sources. Biomass burning data come from GEIA and GFEDv2 (1997–2006) (Randerson et al., 2005), with corrections for forest cover changes. Fossil fuel emissions are sourced from databases such as GEIA, EDGAR, and REAS, with OC/BC ratios based on combustion efficiency. Biogenic OC emissions use GEIA and FAO datasets, with conversion rates from Pandis et al. (1991).

Sulfate aerosol emissions arise from anthropogenic SO_2 sources (e.g., fossil fuel combustion) and natural DMS emissions. SO_2 data are sourced from GEIA and Benkovitz et al. (1996), while DMS emissions are parameterized based on surface solar radiation (Takemura et al., 2000). Emissions exclude sea-ice-covered areas using sea-ice masks from da Silva (1994).

Sea-salt emissions depend on oceanic wind speed, calculated using Erickson et al. (1986), with flux adjustments for sea-ice regions. Natural vegetation and soil emissions are parameterized using LAI, solar zenith angle, and temperature (Spiro et al., 1992). This comprehensive approach enables the model to simulate global aerosol distributions and radiative impacts with high fidelity.

3.2.2. Aerosol transport process simulation

SPRINTARS simulates the full lifecycle of aerosols, encompassing emission, transport, and deposition processes. The transport processes include advection, which is calculated using a flux-form semi-Lagrangian scheme from the MIROC model, and diffusion, which accounts for both horizontal and vertical spreading (Takemura et al., 2000, 2002, 2005). Chemical processes, such as the conversion of sulfur compounds into sulfate aerosols, rely on three-dimensional distributions of oxidants like OH, H_2O_2, and O_3 provided by the CHASER model. Aerosol removal is represented through wet deposition, including washout by rain droplets and rainout via in-cloud scavenging, as well as dry deposition

driven by turbulence and gravitational settling.

The aerosol transport process is governed by the mass conservation equation, which forms the basis of the simulation. This equation accounts for the aerosol mixing ratio changes over time, incorporating contributions from emissions, advection, diffusion, and deposition processes. Mathematically, it is expressed as:

$$\frac{\partial}{\partial \mathrm{t}}(\rho_{\mathrm{air}}\, q_a) \;+\; div\,(\rho_{air}\, q_a\, v) \;+\; \frac{\partial\,(\rho_{\mathrm{air}}\, \mathrm{q_a\, w})}{\partial\, \mathrm{z}} \;=\; \frac{\partial}{\partial\, z}(F_E \;+\; F_D \;+\; F_S) \qquad (3.5)$$

where ρ_{air} is the air density, q_a represents the aerosol mixing ratio, v and w are the horizontal and vertical wind components, and F_E, F_D, F_S denote emission, diffusion, and deposition fluxes, respectively.

The emission flux F_E depends on source-specific factors. For instance, soil dust emissions are calculated based on the wind speed at 10 meters($|\overrightarrow{v_{10}}|$) exceeding a threshold velocity (u_t). The relationship is defined as:

$$\mathrm{F_{dust}} \;=\; \mathrm{C}\,(\,|\overrightarrow{\mathrm{v_{10}}}| \;-\; \mathrm{u_t}\,)^2 \qquad \text{for } |\overrightarrow{\mathrm{v_{10}}}| \;>\; \mathrm{u_t} \qquad (3.6)$$

where C is an empirically determined coefficient related to soil moisture. Such formulations ensure that the model accurately captures emissions from natural and anthropogenic sources.

Deposition processes, encompassing both wet and dry deposition, play a critical role in removing aerosols from the atmosphere. Dry deposition is modeled using a constant dry deposition velocity (v_{dry}), while wet deposition considers two mechanisms: sub-cloud scavenging, where raindrops collide with aerosols, and in-cloud scavenging, where aerosols within cloud droplets are precipitated. For example, the flux due to dry deposition is:

$$F_{\mathrm{dry}} \;=\; -\,\rho_{air}\, q_a\, v_{dry} \qquad (3.7)$$

Vertical diffusion is calculated to account for turbulent mixing using the

gradient of the aerosol mixing ratio with a diffusion coefficient K :

$$F_D = -\rho_{\text{air}} K \frac{\partial q_a}{\partial z} \tag{3.8}$$

3.2.3. AOD calculation

In addition to transport and deposition, the model computes the aerosol optical thickness (τ) to evaluate radiative effects. The optical thickness is derived from the extinction efficiency factor Q_{ext}, effective particle radius r_{eff}, and aerosol concentration. The formula is given by:

$$\tau = \sum_{i,k} \frac{3}{4\rho_{\text{air}} r_{\text{eff}}(i,k)} Q_{\text{ext}}(i,k) q_a(i,k) \Delta p_k \tag{3.9}$$

where Δp_k represents the pressure difference across the model layer, Q_{ext} and r_{eff} are computed based on Mie theory, considering aerosol size distribution and hygroscopic growth under varying humidity conditions.

3.2.3.1. Removal of volcanic effects

When calculating SPRINTARS AOD, the highest AOD values were excluded as anomalies, potentially caused by volcanic eruptions in the Mariana Trench, using the Median Filter method in this study. From Fig. 3.3, the high AOD observed in the Mariana Sea area, which is surrounded by the red dotted line, may be due to volcanic emissions. SPRINTARS is particularly sensitive to emissions.

The median filter (Zhu et al., 2012) is a widely recognized digital filtering technique, highly effective for reducing noise in images while preserving essential edge details. This nonlinear filtering technique involves ordering the pixel values within a predetermined neighborhood (defined by the kernel size) and replacing the central pixel with the median value from this set.

The Median filter operates with a sliding window that traverses each signal

entry sequentially. At each entry, it arranges the neighboring values in numerical order and substitutes the central value with the median from this array. The conventional algorithm relies on this sorting method, which can be inefficient and cause significant execution delays. Therefore, various optimization techniques have been developed to identify the median value more efficiently. In this study, a kernel size of 1x7 was chosen for the median filter applied to the AOD data which can effectively filter out noise while ensuring that the structural integrity and distribution of the AOD data are not compromised.

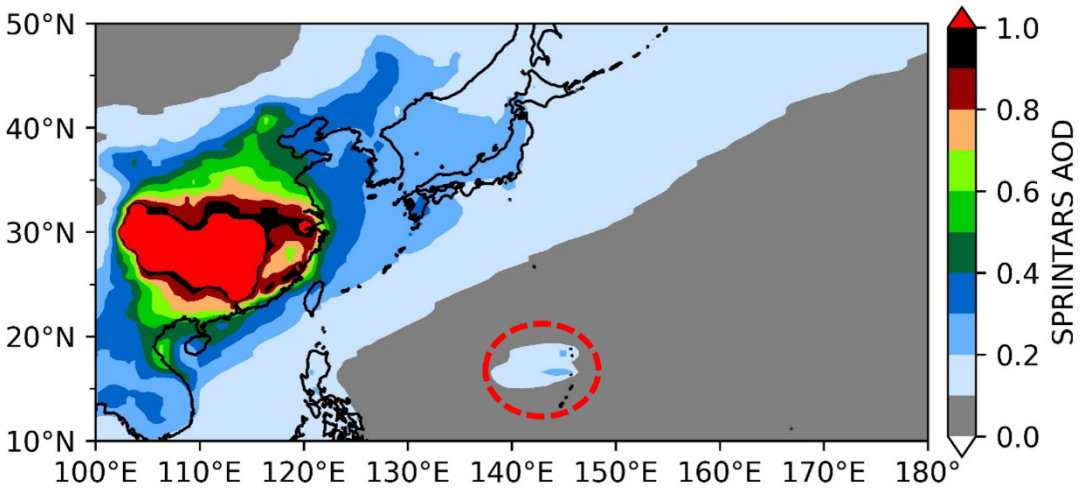

Fig. 3.3 Spatial distribution of annual average SPRINTARS AOD at 550 nm from 2003 to 2021. The position of the red dotted box is the Malina Trench (13°N, 144°E).

Chapter 4. Defining the study area

This chapter provides insights into the potential of using long-term aerosol data, such as AOD values, as tracers for monitoring meteorological conditions through AOD distribution and trajectory analysis. The results show that variation in long-term AOD datasets based on satellite observations (e.g. MODIS) over East Asia, indicate the North China Plain as a prominent emission source region with high AOD value in China. An averaged 10-day forward trajectory from Beijing, Shanghai, Hongkong and Seoul was analyzed by utilizing the Meteorological Data Explorer (METEX) during 2003-2021. The results of forward trajectory suggest that a unique open ocean area at downwind of China was selected as the study area.

4.1. AOD variation over East Aisa

Fig. 4.1 - 4.5 shows annual spatial distribution and trend of MODIS AOD at 550 nm over East Asia from 2003 to 2021. The annual average of AOD over the Chinese mainland shows significant year-to-year variation in emission. Significant variations are characterized by an increasing trend from 2003 to 2012 and a subsequent decreasing trend from 2013 to 2021, as depicted in Fig. 4.5 (e)-(f). The change in AOD trends is largely attributed to the emission control policies introduced with China's Clean Air Action in 2013 (Zheng et al., 2018; Zhang et al., 2019).

The decline in AOD after 2011, as shown in Fig. 4.3, can be associated with two main reasons. The first is a reduction in anthropogenic emissions of primary aerosols, such as sulfur dioxide (SO_2) and nitrogen oxides ($NO_{x)}$, corresponding with the enhancement of vehicle emission standards between 2011 and 2015. This led to a 50% reduction in permissible NO_x emissions from road vehicles

(Wu et al., 2017). The second factor relates to China’s 12th Five-Year Plan (2011–2015), which introduced environmental protection policies targeting improved air quality (Cai et al., 2017). During the period following 2011, there was a notable average AOD decrease per year across most of China. This change corresponds with significant emission reductions due to policy implementations, with highly populated regions showing a more pronounced effect (Sogacheva et al., 2018).

The V-shaped pattern in the AOD time series reflects the 2008-2009 financial crisis's impact when China's economic expansion slowed. Complementary research by Itahashi et al. (2021) shows a decreasing trend in fine mode AOD over the Yellow Sea from 2006 to 2009, with a subsequent rise through to 2011(Fig. 4.7 (a)). While this trend consistent with the AOD analysis over the (North China Plain) NCP, AOD values over the NCP are higher than those over the Yellow Sea, likely due to the inclusion of dust in the total AOD dataset. Despite the substantial variations between 2006 and 2011, the changes in AOD during this period were not very significant.

Additionally, the NCP is identified as a prominent source of high AOD values, depicted by black rectangles in Fig. 4.1-4.5. Similar to the trends over the Chinese mainland, the AOD over the NCP shows significant year-to-year variability and a decreasing AOD trend after 2013. Moreover, a substantial decrease in anthropogenic emissions of various pollutants such as sulfur dioxide and nitrogen oxides after 2013 (Kong et al., 2021), which correlates with the declining AOD trend observed in the NCP (Fig. 4.6). The decreasing variation of AOD over NCP corresponds well with the reduction in anthropogenic emissions (Itahashi et al., 2021), due to the emission regulation policy implemented in 2013 by China (Zheng et al., 2018; Zhang et al., 2019). These observations emphasize the NCP's significant contribution to both anthropogenic and natural aerosols, playing a crucial role in the variability of

AOD in East Asia.

These findings highlight that the NCP remains a significant source of anthropogenic and natural aerosols, which is the main factor driving the variability of Chinese mainland AOD in East Asia and cannot be disregarded. Therefore, to quantitatively detect the variation in meteorological fields due to climate change, it is necessary to remove the effect from Chinese emissions when constructing R_{AOD}.

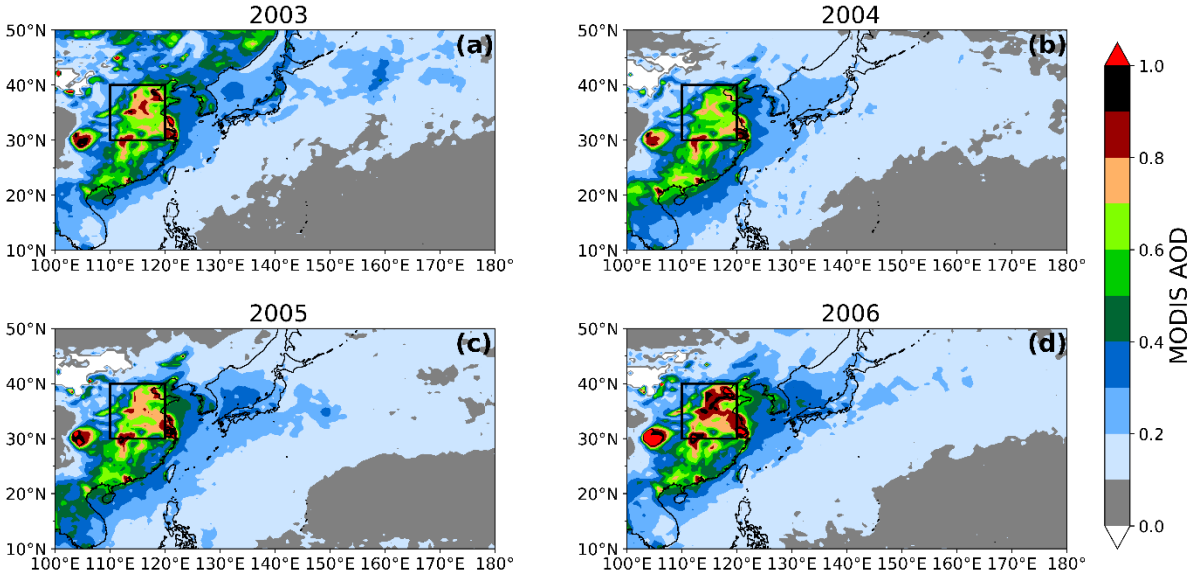

Fig. 4.1 Annual spatial distributions of MODIS AOD values at 550 nm for the years (a) 2003, (b) 2004, (c) 2005, and (d) 2006. Black rectangles represent the NCP region.

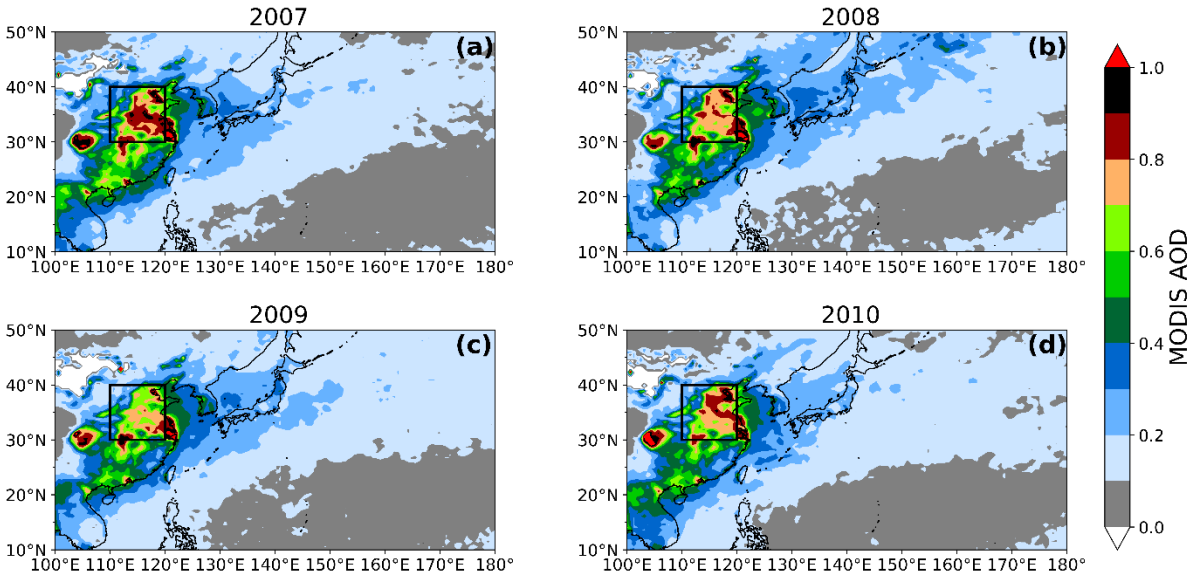

Fig. 4.2 Annual spatial distributions of MODIS AOD values at 550 nm for the years (a) 2007, (b) 2008, (c) 2009, and (d) 2010. Black rectangles represent the NCP region.

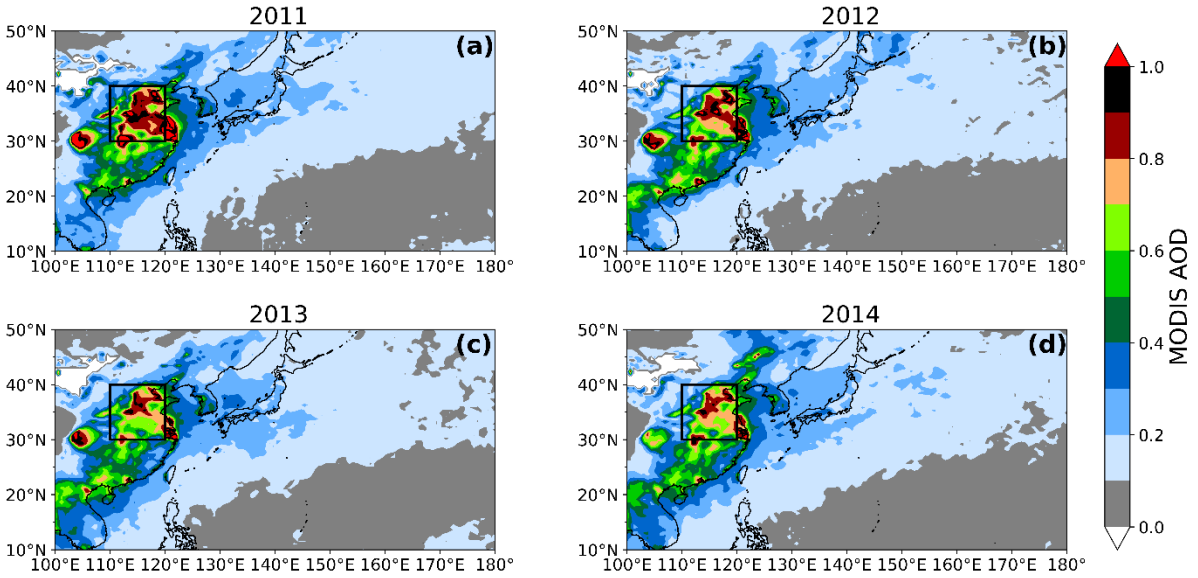

Fig. 4.3 Annual spatial distributions of MODIS AOD values at 550 nm for the years (a) 2011, (b) 2012, (c) 2013, and (d) 2014. Black rectangles represent the NCP region.

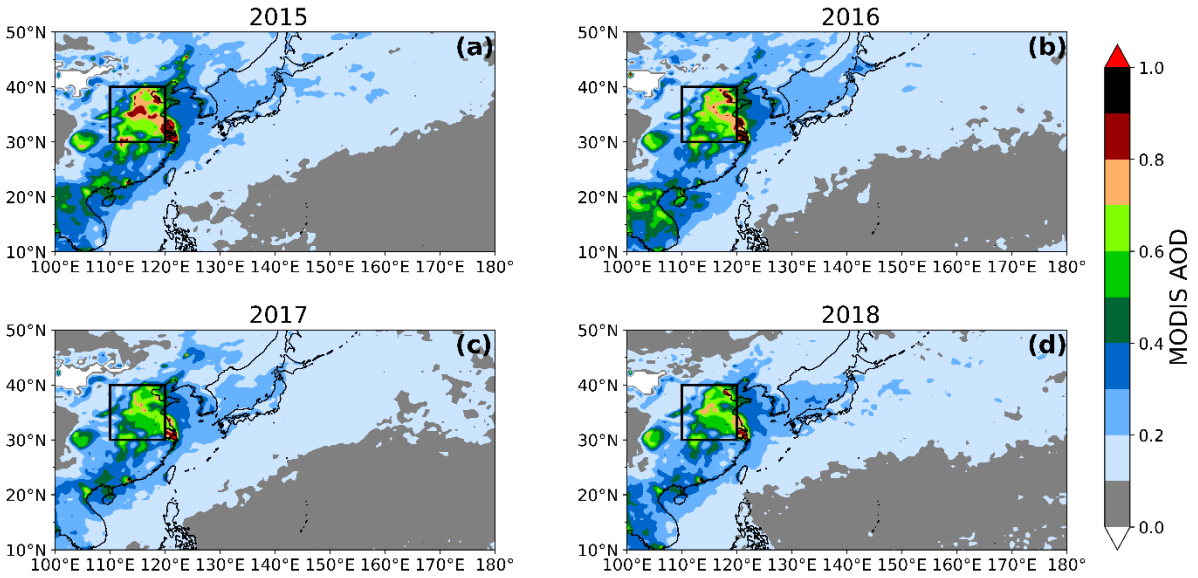

Fig. 4.4 Annual spatial distributions of MODIS AOD values at 550 nm for the years (a) 2015, (b) 2016, (c) 2017, and (d) 2018. Black rectangles represent the NCP region.

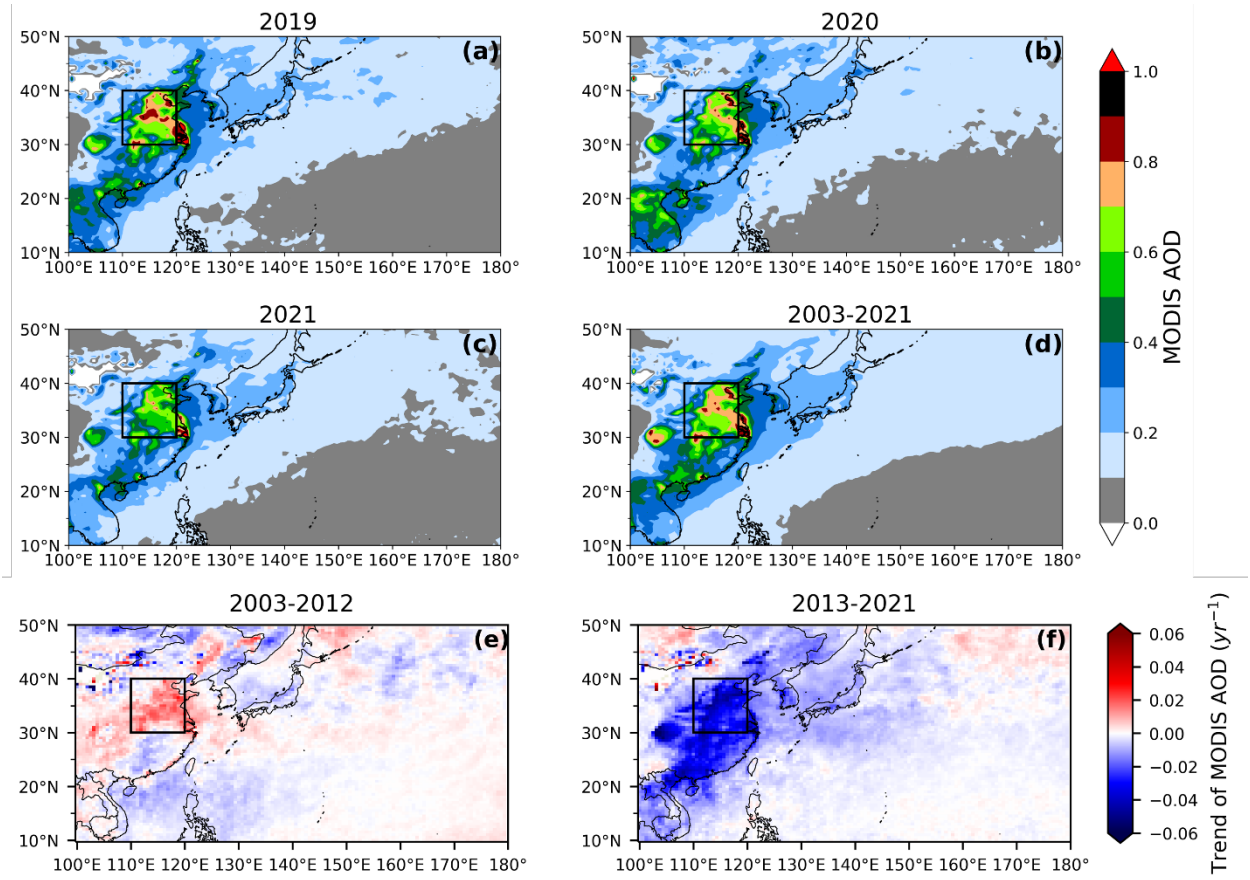

Fig. 4.5 Annual spatial distributions of MODIS AOD values at 550 nm for the years (a) 2019, (b) 2020, (c) 2021, and for the period (d) 2003 to 2021. Annual trend (yr^{-1}) of MODIS AOD at 550 nm from (e) 2003 to 2012 and (f) 2013–2021. Black rectangles represent the NCP region.

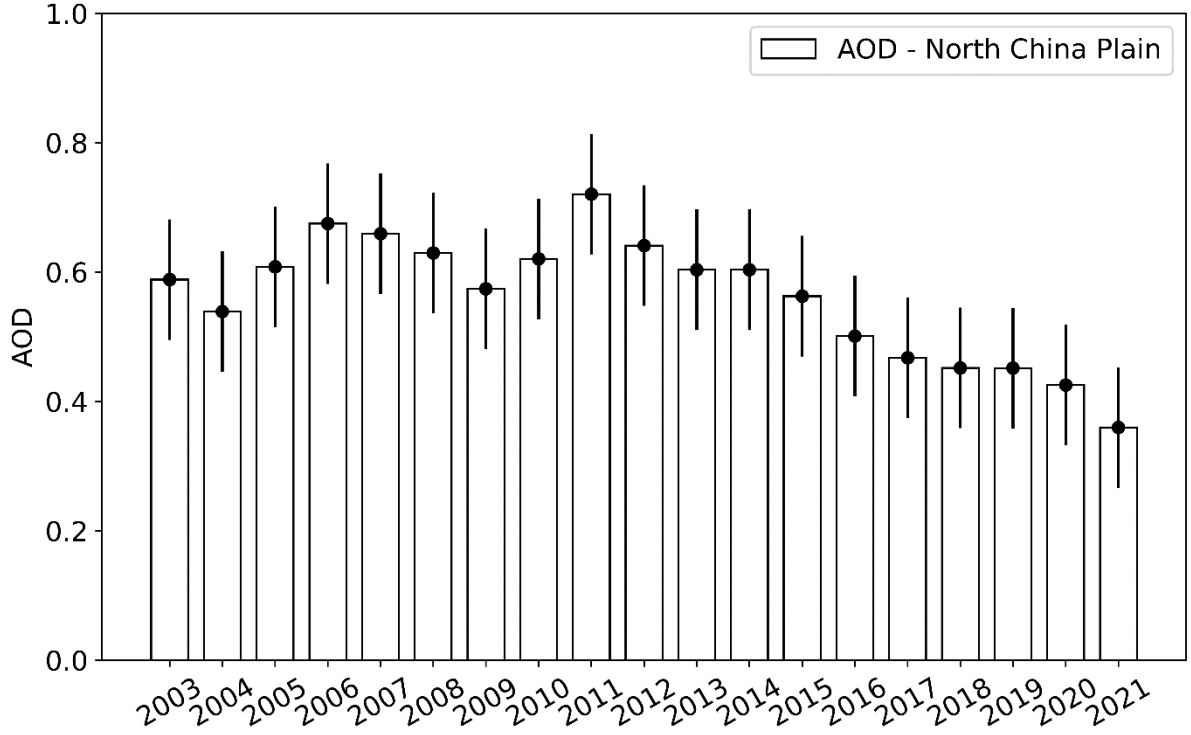

Fig. 4.6 Annual average MODIS AOD at 550 nm over the NCP (30–40°N, 110–120°E) from 2003 to 2021. Error bars represent the standard deviation, indicated as 0.56 ± 0.09.

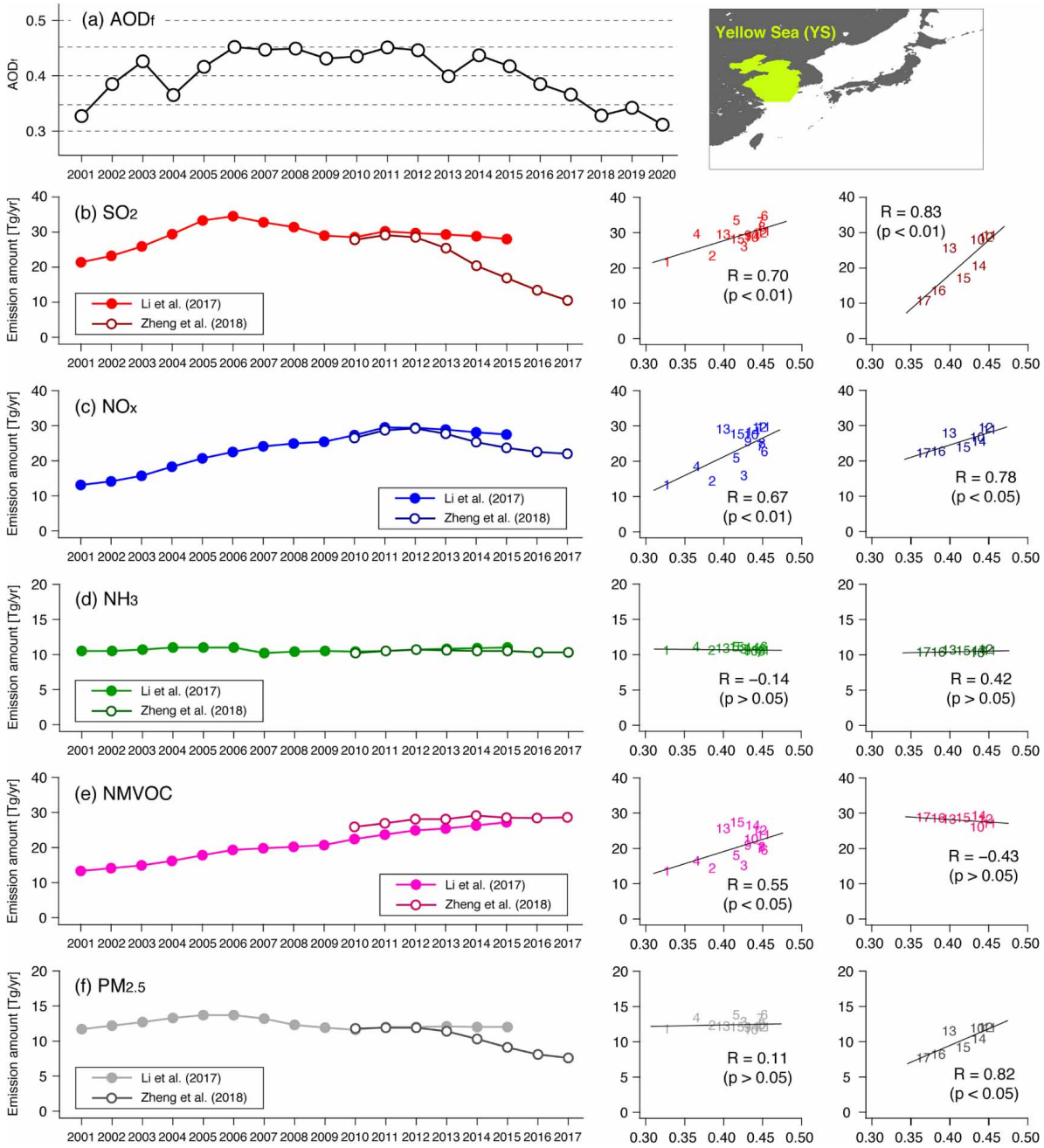

Fig. 4.7 Annual trends of (a) AOD_f (fine-mode AOD) over the Yello Sea and (b)–(f) anthropogenic emissions in China. Scatterplots between AOD_f over the Yello Sea. Cited from Itahashi et al. (2021).

4.2. Analysis of transboundary air pollution pathway

To accurately define the research area, we conducted a detailed analysis to calculate the forward trajectories, identifying a specific marine region located downstream of China. This assessment aimed to enhance our understanding of the dynamics of aerosol transport toward the Pacific Ocean. Fig. 4.8(a)-(d) depict the spatial distribution of MODIS AOD at 550 nm and the 19-year average of 10-day forward trajectories calculated for every day (1 data per day) over the period during 2003 to 2021. This trajectory analysis was calculated across spring, summer, autumn and winter at a height of 100 m above the surface. The trajectory calculations utilized the METEX, which includes a 3D-wind kinematic model (Zeng et al., 2003) with a 24-hour interval of calculation at four major locations: Beijing, Seoul, Shanghai, and Hong Kong for the period 2003 to 2021.

A similar path of 10-day forward trajectory was observed in spring, summer, and autumn, which shows the aerosol transport from west toward east within strength line except winter in Fig. 4.8 (a)-(d). This pattern is particularly noticeable in the spring, largely influenced by the prevailing westerly winds.

Further insights are provided in Fig. 4.9, where an averaged 10-day forward trajectory from 2003 to 2021 across all seasons reveals a clear, direct west-to-east transport path. The western Pacific regions (25–30°N, 125–180°E) situated in the downwind area of China which can clearly represent the phenomenon of aerosol transportation which also show as the aerosol gradient of AOD pattern in MODIS map during 2003 to 2021 (Fig. 4.9).

High AOD values were observed in Fukue (red star in Fig. 4.9), located in western Japan. These values are primarily due to intense aerosol loading, mainly from foreign anthropogenic air pollution, as detailed in studies by Ikeda et al. (2015). The pollution originates from the NCP and is transported over the East China Sea, including emissions notably from Shanghai as reported by Lee

et al. (2019). This suggests the critical role of prevailing westerly winds in forming meteorological patterns that facilitate the transboundary movement of air pollution, potentially impacting air quality as far as Japan.

Additionally, the AOD values on the south side of Sendai (yellow circle in Fig. 4.9) are shown to be affected by transboundary air pollution from Seoul, with significant contributions from emissions in Northeast China and the NCP which supported by Ikeda and colleagues in 2015.

The gradient of AOD (Fig. 4.9) values decreases from the eastern coast of China towards the Pacific Ocean, consistent with the result from recent research by Leung et al. (2023). Additionally, high-concentration aerosol plumes from the NCP have been documented traveling eastward in relatively direct paths across the Pacific Ocean. Both the MODIS AOD maps (Fig. 4.9) and trajectory analyses confirm that the observed gradient pattern in the AOD distribution over the Pacific is predominantly due to transboundary air pollution. Consequently, the prevalent high MODIS AOD levels over mainland China serve as a critical tracer, indicating the significant impact of transboundary air pollution on the western middle Pacific regions downstream from China.

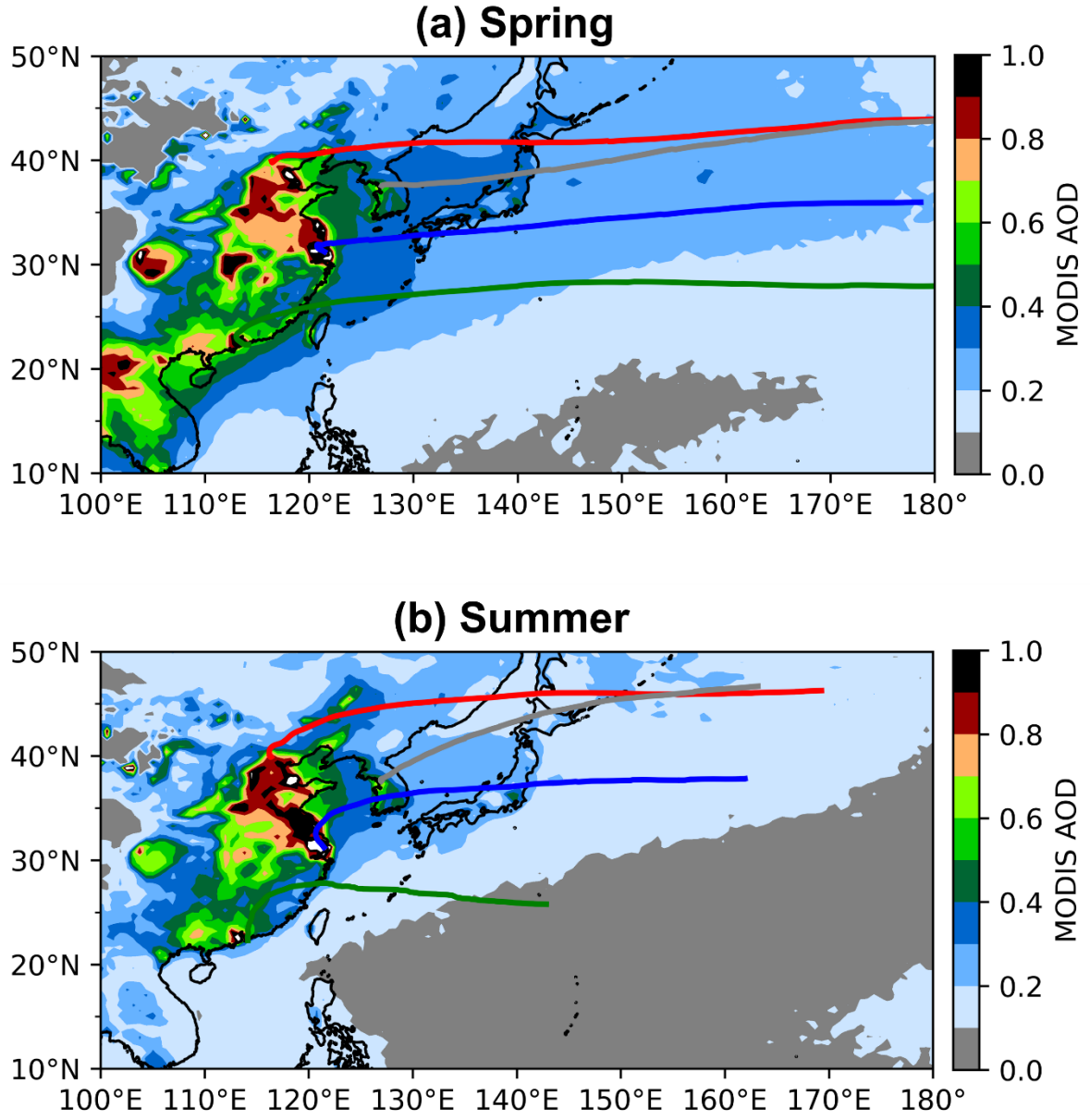
(a) Spring
50°N
40°N
30°N
20°N
10°N
100°E
110°E
120°E
130°E
140°E
150°E
160°E
170°E
180°
1.0
0.8
0.6
0.4
0.2
0.0
MODIS AOD
(b) Summer
50°N
40°N
30°N
20°N
10°N
100°E
110°E
120°E
130°E
140°E
150°E
160°E
170°E
180°
1.0
0.8
0.6
0.4
0.2
0.0
MODIS AOD

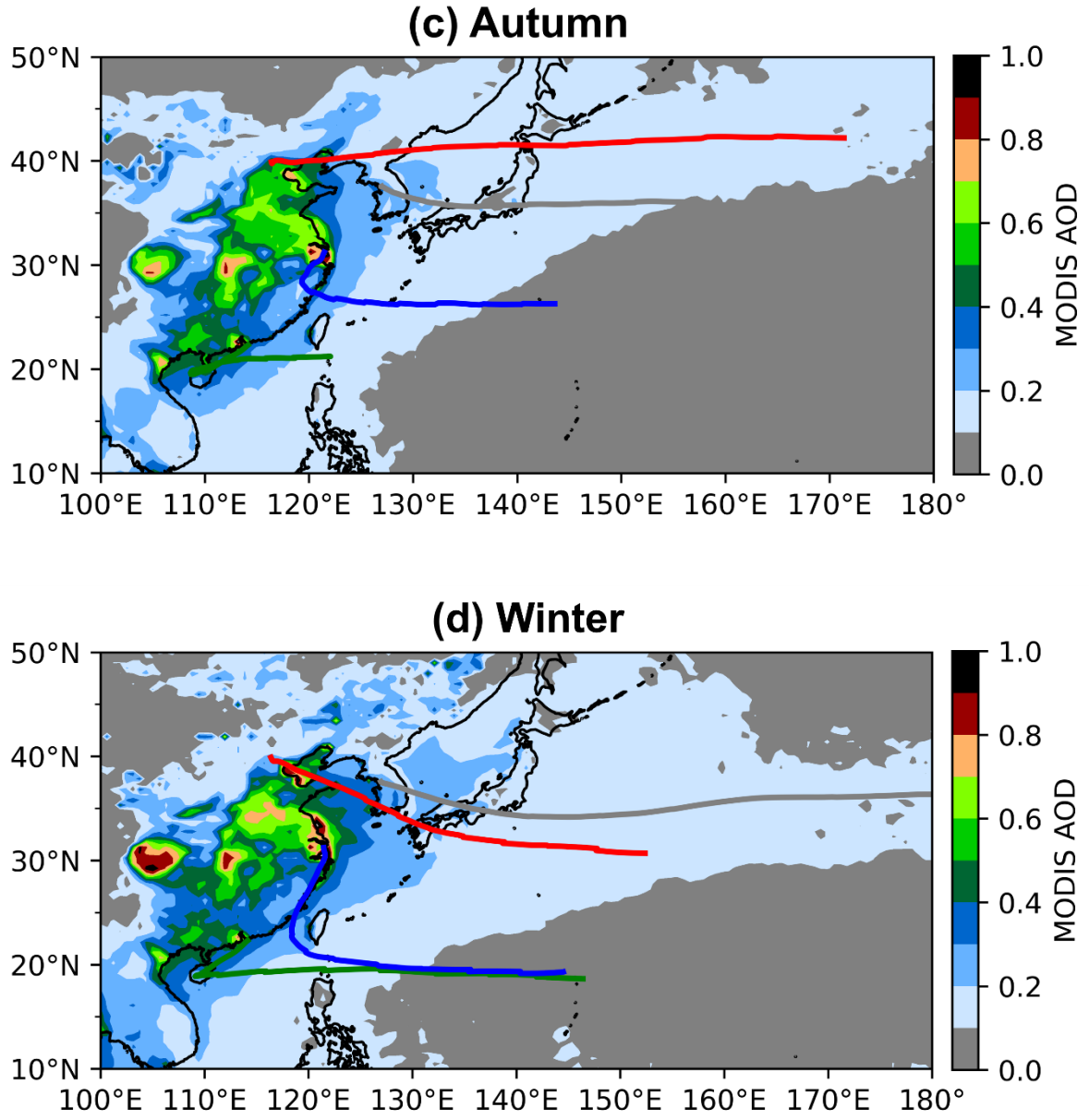

Fig. 4.8 Spatial distribution of annual average MODIS AOD at 550 nm and 19-year average of 10-day forward trajectories calculated for every day (1 data per day) from 2003 to 2021 in (a) Spring, (b) Summer, (c) Autumn and (d) Winter. Lines represent the 19-year average trajectories at 100 m above the surface, calculated by METEX using a 3D-wind kinematic model with 24-hour intervals for Beijing (red), Seoul (gray), Shanghai (blue), and Hong Kong (green).

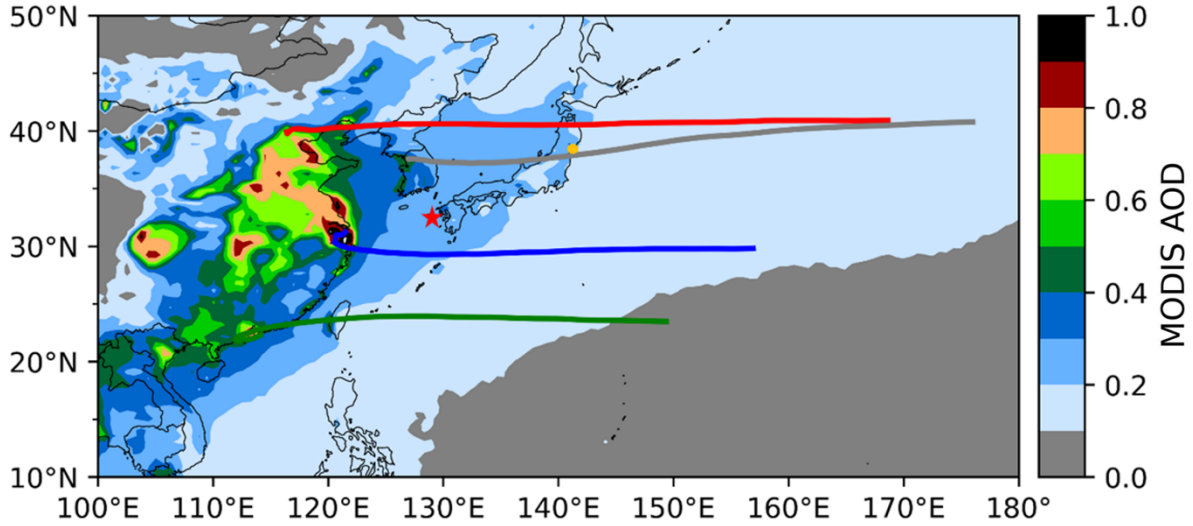

Fig. 4.9 Spatial distribution of annual average MODIS AOD at 550 nm and 19-year average of 10-day forward trajectories calculated for every day (1 data per day) from 2003 to 2021, across all seasons. Lines represent the 19-year average trajectories at 100 m above the surface, calculated by METEX using a 3D-wind kinematic model with 24-hour intervals for Beijing (red), Seoul (gray), Shanghai (blue), and Hong Kong (green). Fukue (red star) is located in western Japan, and Sendai (yellow circle) is in eastern Japan.

4.3. Study area

Our study focuses on the western Pacific regions (25–30°N, 125–180°E), located in the downwind area of China as illustrated in Fig. 4.10 This specific area is characterized by its location over the open ocean, where anthropogenic impacts are significantly reduced, making it a vital area for studying transboundary air pollution transport. Efforts to minimize confounding variables such as plankton influences (Park et al., 2022) and human activities prevalent along the coastal zones, led to the selection specifically starting at longitude 125°E on the eastern coastline of China. This choice ensures that the study area is optimally positioned to assess meteorological variation with minimal local interference. A comprehensive selection for this study area is depicted in Section 5.1.1.

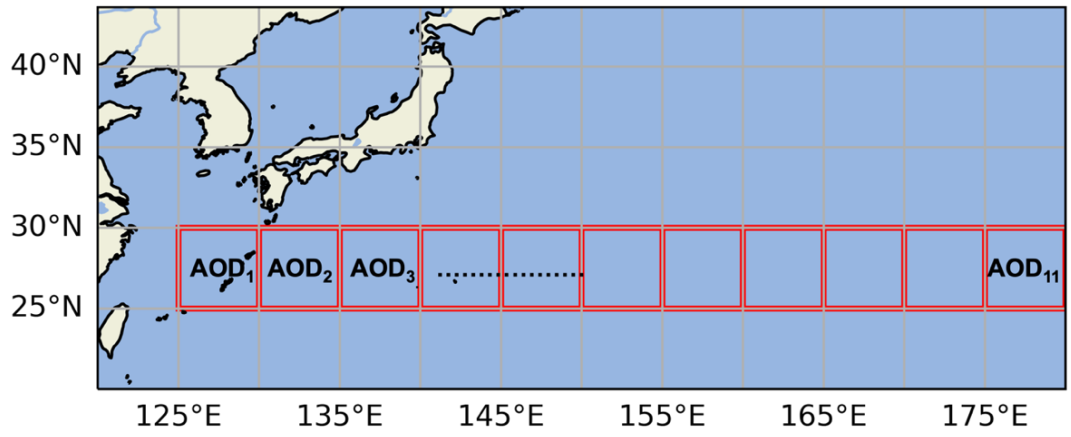

Fig. 4.10 Map depicting the study area. The red rectangles show the study region spanning 25–30°N and 125–180°E, segmented into 5° intervals. AOD_1 represents the average of Level-2 AOD values over the ocean within the 25–30°N and 125–130°E rectangle. Similarly, AOD_2, AOD_3, and AOD_{11} correspond to averages at 130–135°E, 135–140°E, and 175–180°E, respectively.

Chapter 5. A new metric R_{AOD}

In this chapter, to accurately assess the long-term variation in aerosol amounts during long-range transport, the ratio named R_{AOD}' was analyzed. This ratio measures the AOD over oceanic regions at every 5° of longitude and contrasts this with AOD measurements along the eastern coast of China (25–30°N, 125–180°E) utilizing MODIS AOD data (further details provided in Section 5.1). To address the potential influence of sea salt, designated as AOD^{ss} in the MERRA-2 sea salt AOD dataset, a modified ratio, R_{AOD}'', was introduced in this research (additional details in Section 5.2). Furthermore, a refined metric called R_{AOD}, detailed in Section 5.3, was developed, which is adjusted to exclude the impacts of oceanic DMS and organic matter. These elements are significant as they substantially contribute to the atmospheric conditions over marine areas and are represented by AOD_{11}^{*}.

5.1. Construction of R_{AOD}'

Using the phenomenon of high-concentration aerosols originating from the NCP and being transported eastward, a new metric, R_{AOD}', has been developed to quantitatively assess long-term changes in aerosol quantities during their long-range transport. This metric, R_{AOD}', enhances the detectability of potential climate change effects on meteorological fields. Emissions from the NCP are the primary drivers of fluctuations in AOD along China's eastern coast and significantly influence the region's AOD levels, complicating the assessment of how climate change could impact meteorological fields and transboundary air pollution pathway.

The new metric, R_{AOD}', is calculated by determining the ratio of AOD for every

5° of longitude over the ocean compared to the AOD along the eastern coast of China within the longitudinal range of 125–180°E. Here is how R_{AOD}' is calculated:

$$\boldsymbol{R_{AOD}}' = \frac{\mathbf{AOD_n}}{\mathbf{AOD_1}} \quad (5.1)$$

In the numerator, AOD_n represents the average ocean AOD for each 5° longitude interval within the range of 25–30°N and 125–180°E, where the index n varies from 1 to 11. For instance, AOD_1 corresponds to the average ocean AOD between 125–130°E, and AOD_2 corresponds to 130–135°E, as illustrated in Fig. 4.10.

5.1.1. Sensitivity analysis of R_{AOD}' across different latitude bands

To verify the accuracy of R_{AOD}', daily and annual average AOD data were analyzed from ground-based Skyradiometer instruments located at Minamitorishima (24.30°N, 153.97°E, 0 m a.s.l.) and Hedo (26.87°N, 128.25°E, 65 m a.s.l.). These instruments, part of the SKYNET network, measure direct solar and diffuse irradiances across ultraviolet, visible, and near-infrared wavelengths, facilitating AOD retrieval (Nakajima et al., 1996, 2007; Hashimoto et al., 2012).

Fig. 5.1(a) displays the daily mean AOD values recorded at Minamitorishima and Hedo from 2008 to 2009. Hedo reported higher average AOD values of 0.30 ± 0.12 compared to Minamitorishima's 0.11 ± 0.04, largely attributed to Hedo's closer proximity to the eastern coast of China, as shown in Fig. 5.1(c). Fig. 5.1(b) conducts a sensitivity analysis of R_{AOD}' across different latitude bands using MODIS data, showing minimal variations in R_{AOD}' values across longitude bands, except for significant anthropogenic influences noted at the 30–35°N latitude band.

For broader spatial analysis, a coarser grid at the latitude band of 25–30°N was selected to monitor the decrease in AOD as aerosols move eastward. The validation involved comparing the AOD ratio of 0.37 ± 0.20 measured by Skyradiometer at the Minamitorishima and Hedo during 2008 to 2009. The consistency of this ratio with R_{AOD}' values of 0.38 in the 145–150°E range and 0.32 in the 150–155°E range confirms the accuracy of R_{AOD}' in capturing longitudinal aerosol distribution.

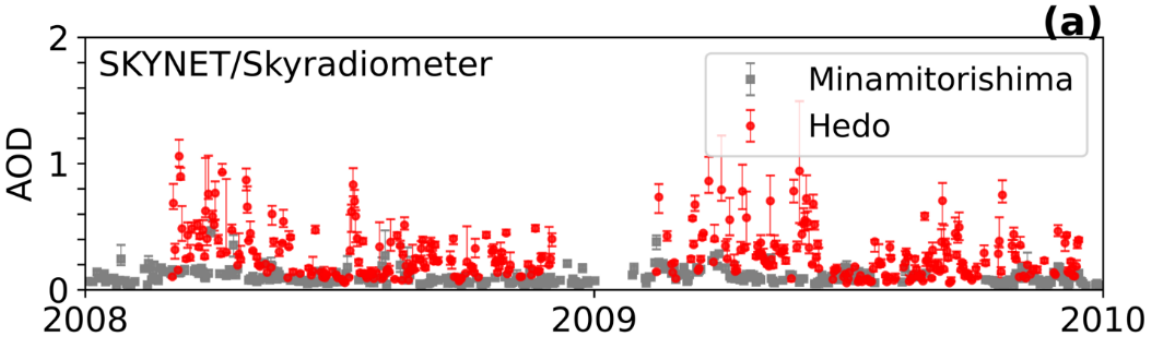
(a)
SKYNET/Skyradiometer
Minamitorishima
Hedo
AOD
2
1
0
2008
2009
2010

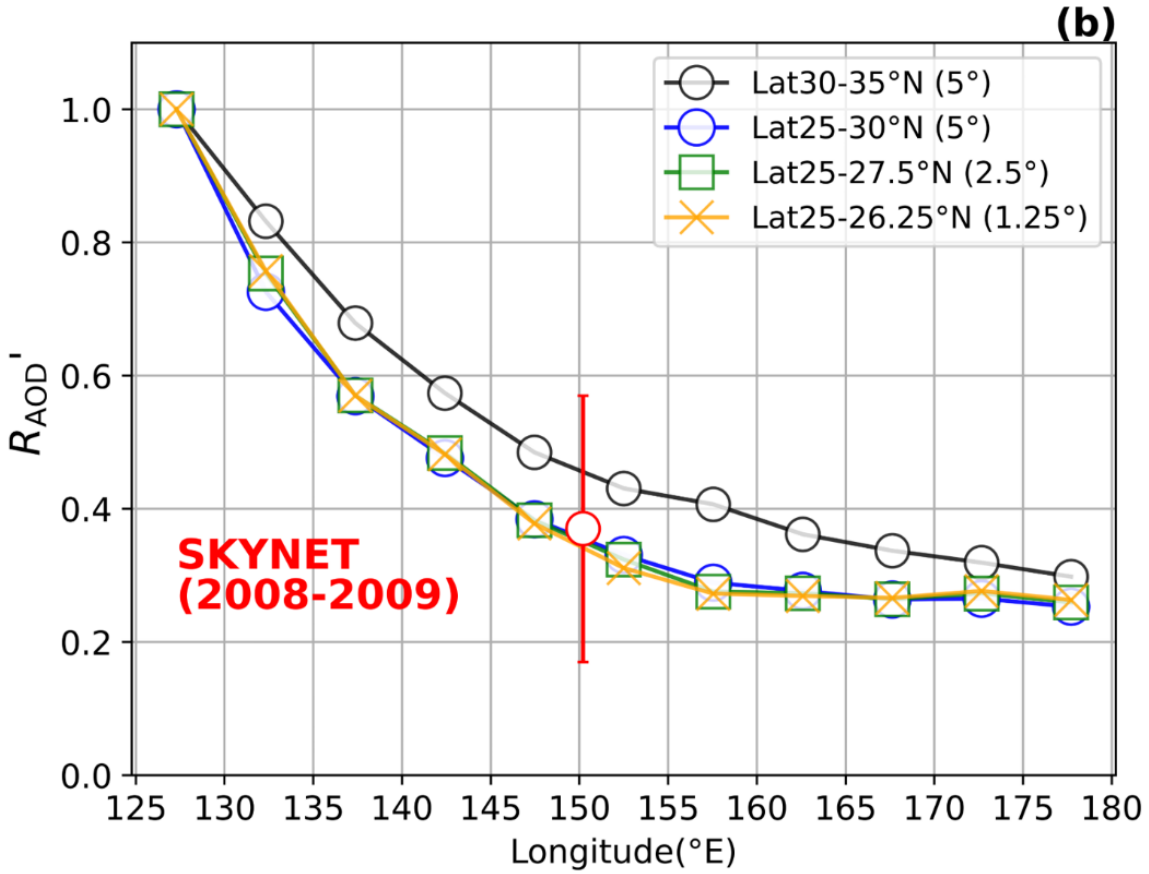
(b)
Lat30-35°N (5°)
Lat25-30°N (5°)
Lat25-27.5°N (2.5°)
Lat25-26.25°N (1.25°)
R_{AOD}'
1.0
0.8
0.6
0.4
0.2
0.0
SKYNET
(2008-2009)
125 130 135 140 145 150 155 160 165 170 175 180
Longitude(°E)

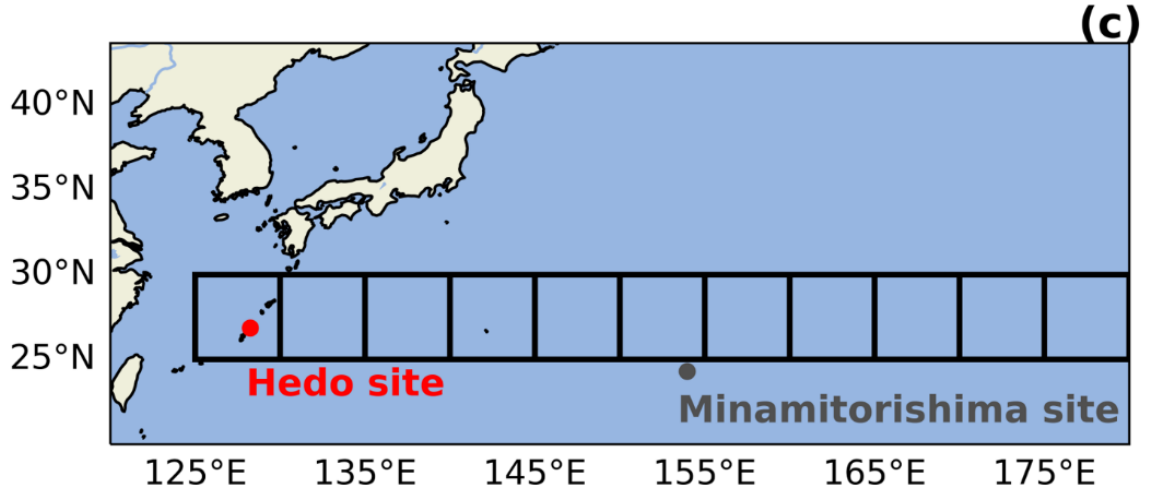
(c)
40°N
35°N
30°N
25°N
Hedo site
Minamitorishima site
125°E
135°E
145°E
155°E
165°E
175°E

Fig. 5.1 (a) Daily median AOD values recorded at Minamitorishima (24.30°N, 153.97°E, 0 m a.s.l.) and Hedo (26.87°N, 128.25°E, 65 m a.s.l.) from 2008 to 2009, measured by Skyradiometers. Error bars show measurement uncertainties at Minamitorishima (gray) and Hedo (red). (b) Sensitivity analysis of R_{AOD}' in the longitudinal range of 125–180°E, evaluated across various latitude bands at intervals of 1.25° (25–26.25°N marked with orange crosses), 2.5° (25–27.5°N marked with green squares), and 5° (25–30°N and 30–35°N marked with blue and black circular markers) using MODIS data. The red error bar indicates a ratio of 0.37 ± 0.20, representing the average AOD comparison between Minamitorishima and Hedo based on 2008 to 2009 Skyradiometer data. (c) Map showing the locations of the Minamitorishima site (gray circle), Hedo site (red circle), and the study areas (outlined in black rectangles).

Fig. 5.2 demonstrates a correlation between R_{AOD}' and AOD_1, with observed variations across different longitudinal bands at 130–135°E, 145–150°E, and 175–180°E. R_{AOD}' values decrease progressively from 130–135°E to 175–180°E, consistent with the results from forward trajectory analysis (Fig. 4.9). The open circles represent average AOD_1 values within the ranges of 0.15–0.19, 0.19–0.23, and 0.23–0.27. These hollow circles show that R_{AOD}' varied by only ± 0.1, despite a 1.5-fold increase in average AOD1 values due to emissions from mainland China (Fig. 5.2). This indicates that R_{AOD}' effectively counters the impact of temporal fluctuations in emissions from China. Moreover, the negative correlations between R_{AOD}' and AOD_1, characterized by slopes of −0.22, −0.56, and −1.64 at 130–135°E, 145–150°E, and 175–180°E, respectively, might be influenced by sea salt and cloud cover.

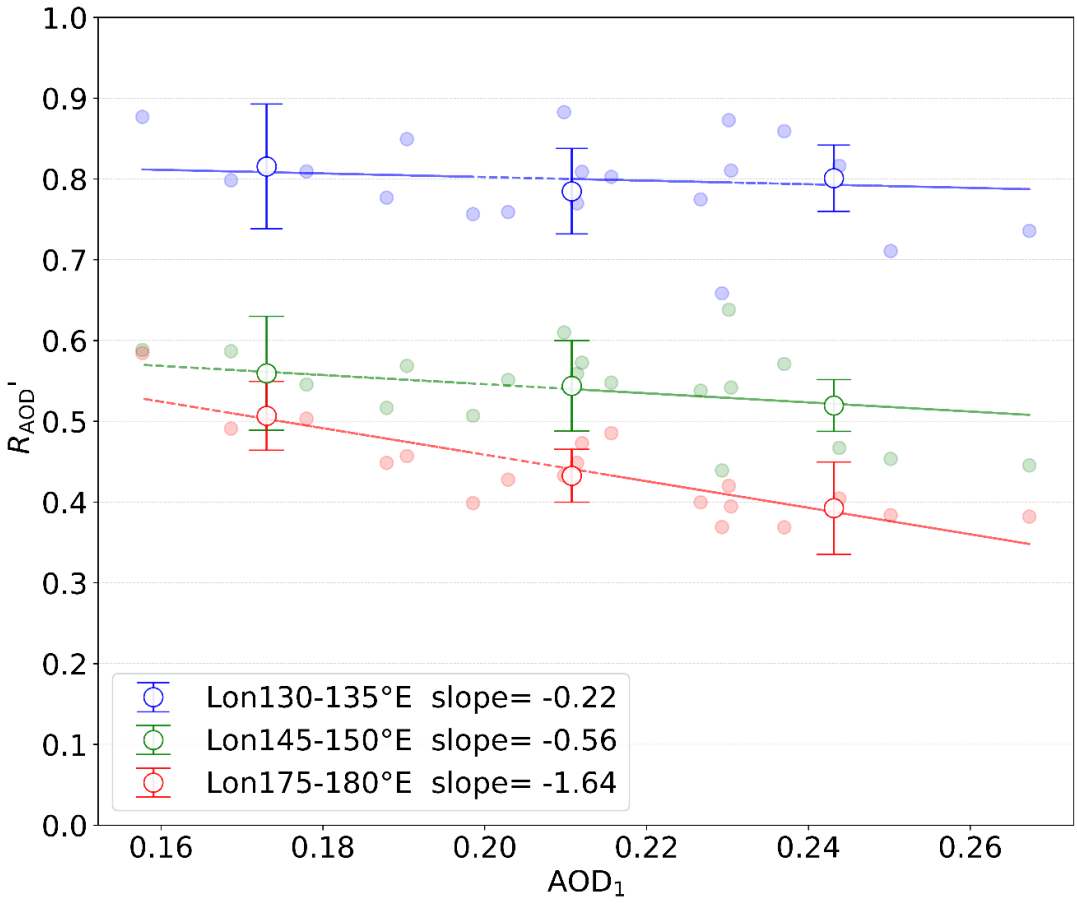

Fig. 5.2 Correlation analysis between R_{AOD}' and AOD_1 (MODIS AOD 550 nm at 125–130°E). Longitudinal segments are depicted with circles: 130–135°E (blue), 145–150°E (green), and 175–180°E (red). Error bars, represented by hollow circles and calculated using the standard deviation, indicate the average AOD_1 values for the ranges 0.15–0.19, 0.19–0.23, and 0.23–0.27. Colored lines illustrate the regression lines for average AOD_1, with their slopes detailed in the legend.

5.2. Construction of R_{AOD}''

To explore the impacts of sea salt and cloud coverage, we employed MERRA-2 data, which adjusts for cloud cover. To isolate the background influence of sea salt, we subtracted the monthly average sea salt AOD at each grid from the MERRA-2 data. MODIS utilizes MERRA-2 sea salt AOD data due to its integration of satellite data through assimilation, which consistent well with MODIS sensors. Additionally, the average MERRA-2 sea salt AOD value near

terrestrial areas is higher than in the northwestern Pacific, yet it stabilizes at approximately 0.05 within the rectangular region spanning 25–30°N and 125–180°E (Fig. 5.3). This sea salt effect is accounted for as a background variable in the R_{AOD}" calculation as follows:

$$\boldsymbol{R_{AOD}''} = \frac{\mathbf{AOD_n - AOD_n^{ss}}}{\mathbf{AOD_1 - AOD_1^{ss}}} \tag{5.2}$$

As shown in equation (5.1), $\mathrm{AOD_n}$ represents the average ocean AOD calculated for every 5° of longitude within the latitude range of 25–30°N and longitude range of 125–180°E, where n ranges from 1 to 11. Similarly, $\mathrm{AOD_n^{ss}}$ indicates the average sea salt AOD from MERRA-2 for each 5° of longitude interval within the same latitudinal and longitudinal range. Specifically, $\mathrm{AOD_1^{ss}}$ refers to the average sea salt AOD from MERRA-2 at 125–130°E.

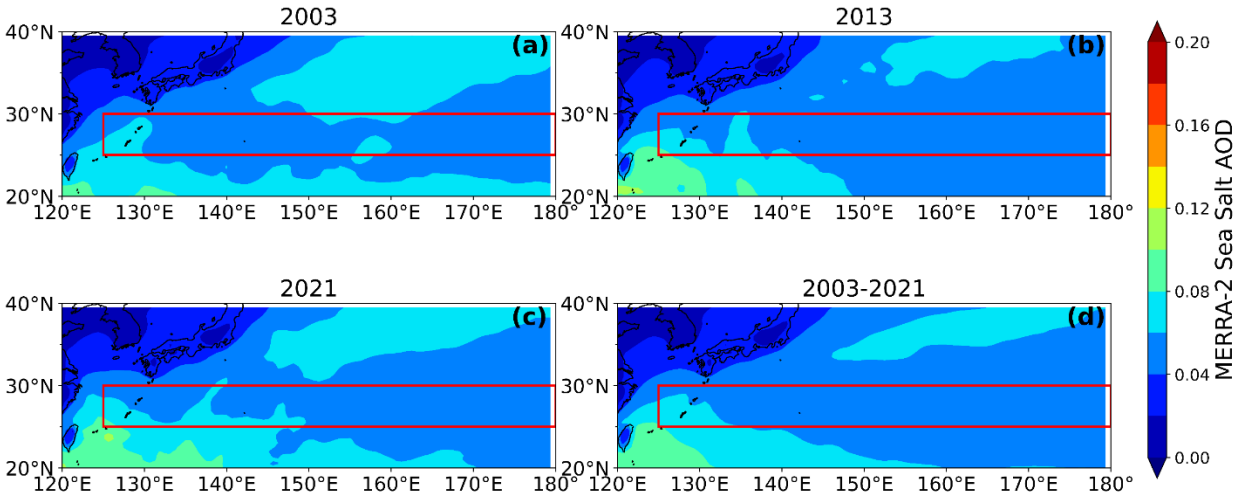

Fig. 5.3 Spatial distributions of annual average of the MERRA-2 sea salt AOD at 550 nm for the years (a) 2003, (b) 2013, (c) 2021, along with the cumulative period (d) from 2003 to 2021. The red rectangles delineate a study area extending from 25–30°N to 125–180°E.

Similar to Fig. 5.2, Fig. 5.4 presents a correlational analysis between $R_{AOD}^{''}$ and AOD_1 across the longitude bands of 130–135°E, 145–150°E, and 175–180°E. In contrast to the negative correlation observed between $R_{AOD}^{'}$ and AOD_1 (Fig. 5.2), a positive correlation is evident between $R_{AOD}^{''}$ and AOD_1 in Fig. 5.4, with slopes of 0.23 and 0.44 at 130–135°E and 145–150°E respectively. Furthermore, the relationship between $R_{AOD}^{''}$ and AOD_1 at 175–180°E shows a more moderate slope of -0.90 compared to the steeper slope of -1.64 between $R_{AOD}^{'}$ and AOD_1, indicating a significant contribution from sea salt. Additionally, the increased steepness of the slope at 175–180°E relative to other longitude bands may be attributed to the influence of oceanic DMS and organic matter.

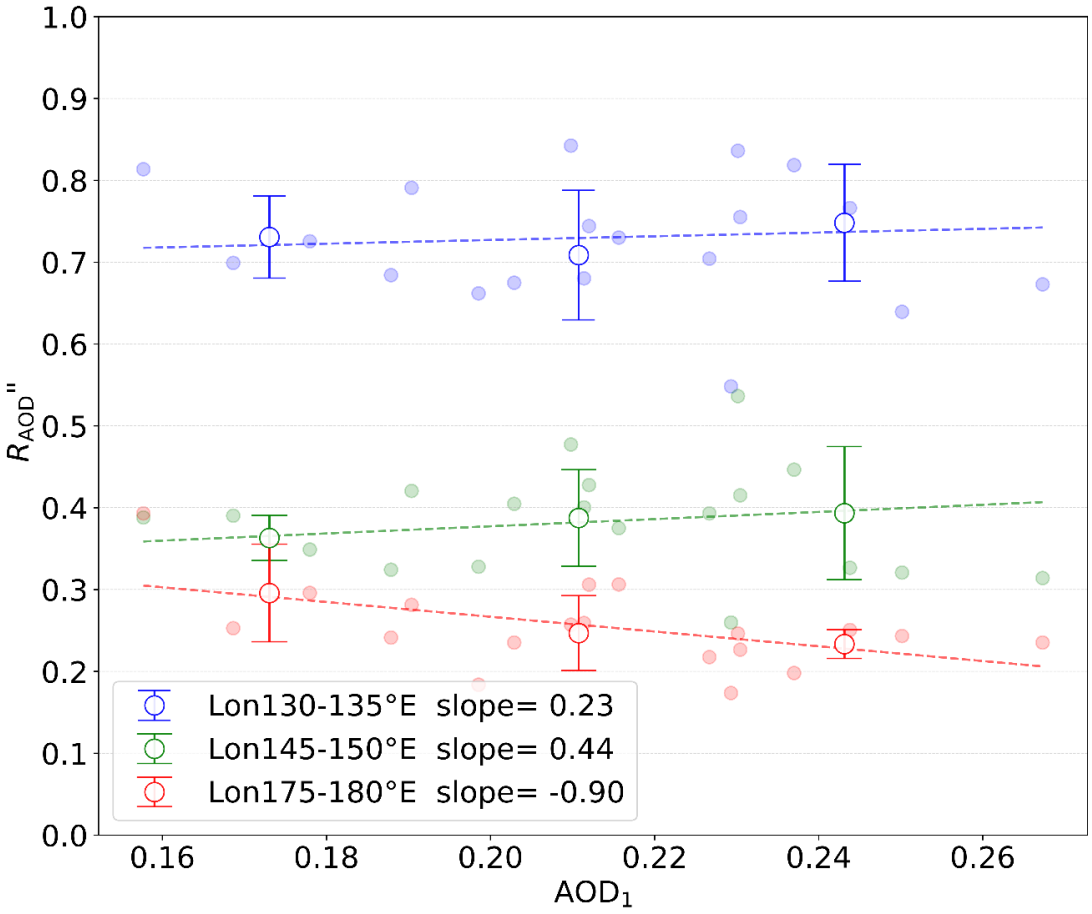

Fig. 5.4. Correlational analysis between R_{AOD}" and AOD_1 (MODIS AOD 550 nm at 125–130°E). This figure retains the longitudinal segments and error bar methodologies of Fig. 5.2 and includes regression lines for the average AOD_1 values, with the regression line slopes in the legend.

5.3. Construction of R_{AOD}

DMS, a dominant sulfur compound, plays a crucial role in atmospheric chemistry and global climate regulation. It is predominantly produced by natural sources, such as marine phytoplankton, bacteria, and certain plants, primarily released into the atmosphere through oceanic processes. DMS emissions peak during the summer in the Northern Hemisphere. Globally, DMS emissions (excluding sea salt) range between 98–120 Tg(s)yr^{-1}, with oceanic DMS levels ranging from 15–25 Tg(s)yr^{-1}. In the Northern Hemisphere alone, oceanic DMS emissions are approximately 8.4 Tg(s)yr^{-1} (Seinfeld and Pandis, 2016;

Berresheim et al., 1995), highlighting the importance of oceanic DMS emissions in defining R_{AOD} over marine environments.

Therefore, for an accurate estimation of R_{AOD}, it is essential to accurately include contributions from naturally occurring oceanic aerosols, such as DMS and organic matter. R_{AOD} is computed using the equation below:

$$\boldsymbol{R_{AOD}} = \frac{\mathbf{AOD_n - AOD_n^{ss} - AOD_{11}^{*}}}{\mathbf{AOD_1 - AOD_1^{ss} - AOD_{11}^{*}}}$$

(5.3)

$$\mathbf{AOD_{11}^{*}} = \mathbf{AOD_{11}} - \mathbf{AOD_{11}^{ss}}$$

As outlined in equations (5.1) and (5.2), $\mathrm{AOD_n}$ represents the average ocean AOD measured at 5° longitude intervals within the latitude range of 25–30°N and longitude range of 125–180°E, where *n* ranges from 1 to 11. $\mathrm{AOD_n^{ss}}$ denotes the average sea salt AOD from MERRA-2 within the same geographical range. $\mathrm{AOD_{11}^{*}}$ quantifies the effects of oceanic DMS and organic matter, calculated by subtracting the average sea salt AOD from MERRA-2 at 25–30°N and 175–180°E. Fig. 5.5. shows the flow chart of R_{AOD}.

To evaluate the R_{AOD} performance with other datasets, we AOD data from SPRINTARS version 6.1.0, which considers aerosol transport processes. SPRINTARS data provides accurate simulations of global climate changes and air pollution, influenced by both natural and anthropogenic aerosols in the Asian region over extended periods (Takemura et al., 2000, 2002, 2005, 2009). The original resolution of the SPRINTARS AOD data at 550 nm (0.5625°×0.5625°) was adjusted to match the MERRA-2 resolution (0.625°×0.5°) using the nearest neighbor method. The highest AOD values were excluded using the median filter method, treating them as anomalies potentially caused by volcanic eruptions in the Mariana Trench.

A peak in SPRINTARS AOD data (Fig. 5.6) observed at the Mariana Trench (latitude 13°N, longitude 144°E), located over 2500 km south of Japan, close to the study area, could potentially be attributed to an underwater volcanic eruption. To mitigate the influence of submarine volcanic activity on SPRINTARS AOD data near the Mariana Trench, the median filter method with a kernel size of 7 was applied. This approach helps reduce the impact of emission data overestimation related to volcanic activity. Although the MERRA-2 dataset monitors volcanic events, it does not include volcanoes that have erupted after 2010 or subglacial or submarine volcanoes. Thus these impacts are disregarded in this analysis (Randles et al., 2017).

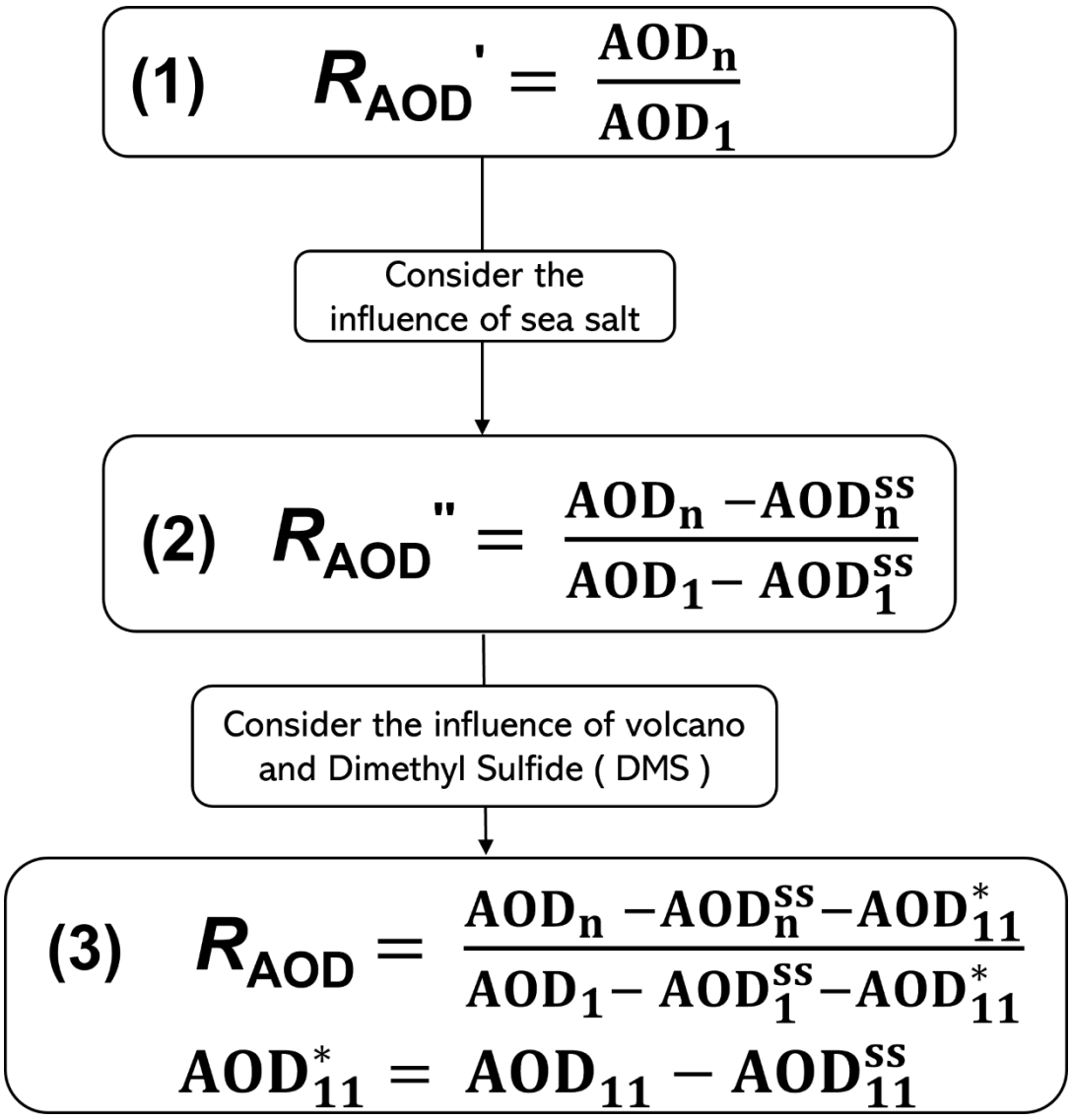

Fig. 5.5 The flow chart deriving R_{AOD}.

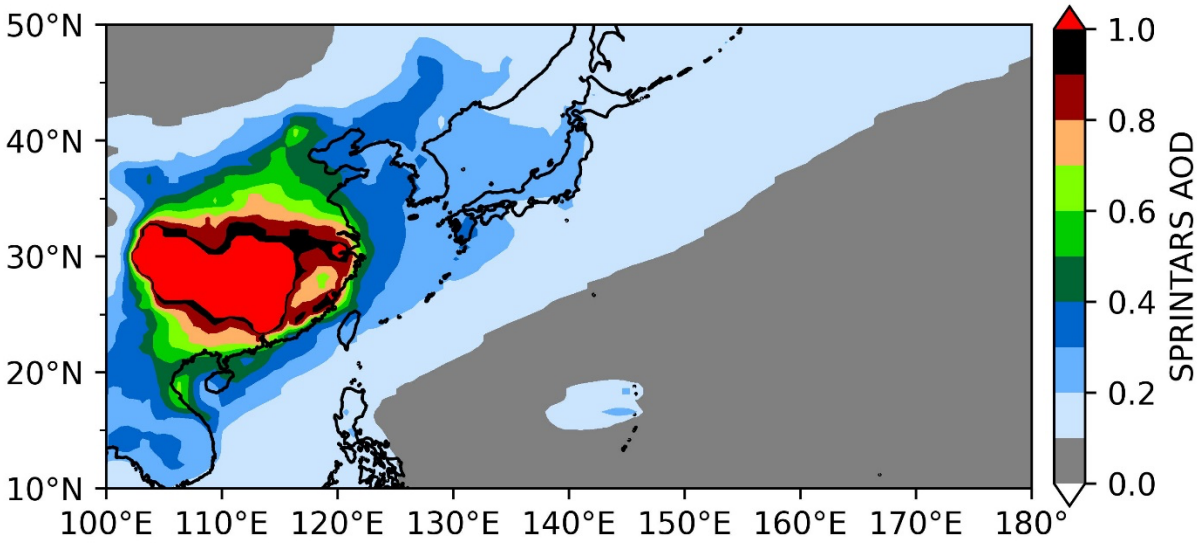

Fig. 5.6 Spatial distribution of annual average SPRINTARS AOD at 550 nm from 2003 to 2021.

Chapter 6. Evaluation of atmospheric transport fields variability using R_{AOD} over 19 years

This chapter evaluates the atmospheric transport variation by discussing the characteristics of R_{AOD}, based on Cai et al. (2024). Section 6.1 analyzes the longitudinal distribution of R_{AOD}, revealing an eastward exponential decline over 19 years. Section 6.4 examines the monthly and seasonal changes in wind speed and direction, while Section 6.5 discusses long-term variations in atmospheric transport fields.

6.1. Longitudinal distribution of R_{AOD}

6.1.1. The 19-year average of longitudinal distribution of R_{AOD}

To analyze the natural attenuation of AOD during transboundary air pollution transport, we used the exponential function because it reflects the natural decay behavior of aerosols as follows:

$$d\tau = -\alpha\tau dx \tag{6.1}$$

$$\int \frac{d\tau}{\tau} = -\alpha \int dx \tag{6.2}$$

$$\ln\tau - \ln\tau_0 = -\alpha L \tag{6.3}$$

$$\tau = \tau_0 exp(-\alpha L) \tag{6.4}$$

where τ is AOD, τ_0 represent the AOD along the eastern coast of China (25–30°N, 125–180°E), dx represent an infinitesimal distance along the path of transport of the aerosols, $d\tau$ represents the change in AOD during its natural attenuation over an infinitesimal distance of transport (6.1), and α is an

attenuation coefficient of AOD, describing the rate at which aerosols are removed or diminished per unit distance due to physical or chemical processes, such as deposition or dispersion. L is the length of the transboundary air pollution path from the eastern coast of China to Pacific region. After integration, equation (6.4) describes the natural attenuation of AOD during its transport along the path of transboundary pollution.

Fig. 6.1 displays the longitudinal distribution of R_{AOD} values from MODIS, MERRA-2, and SPRINTARS datasets across the 125–180°E range. The slopes of the R_{AOD} curves, determined through exponential fitting, are −0.08 for both MODIS and MERRA-2, and −0.07 for SPRINTARS. Both MODIS and MERRA-2 data reveal a consistent pattern of exponential decline in R_{AOD} values moving eastward from China's eastern coast, a trend that SPRINTARS also replicates (Fig. 6.1). The decreasing trend observed in the MODIS R_{AOD} data, consistent with the MERRA-2 dataset, which includes cloud cover indicates that cloud cover does not significantly influence R_{AOD} variability. Therefore, it appears that changes in meteorological conditions are the predominant factors affecting R_{AOD} variations.

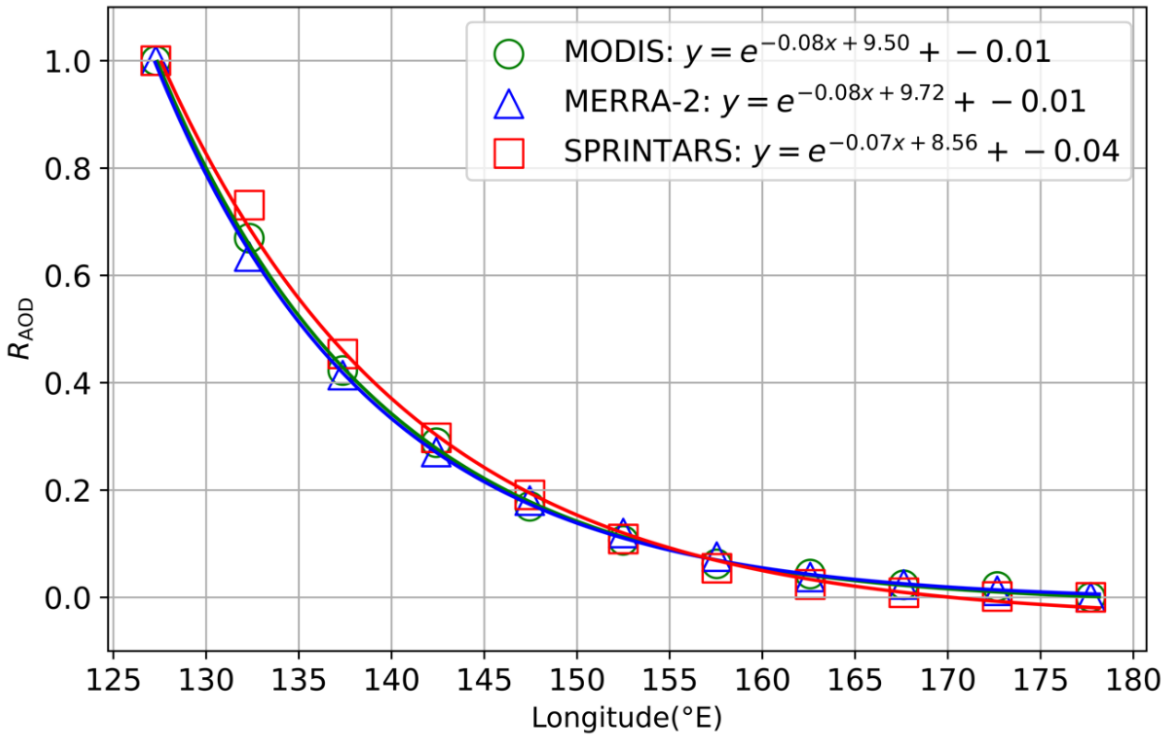

Fig. 6.1 Longitudinal analysis of R_{AOD} within the 25–30°N and 125–180°E ranges, divided into 5° intervals, utilizing data from MODIS (represented by green circles), MERRA-2 (blue triangles), and SPRINTARS (red rectangles) over the period from 2003 to 2021. The curve of R_{AOD}, derived from exponential fitting, slopes are −0.08 for both MODIS and MERRA-2, and −0.07 for SPRINTARS.

6.1.2. Seasonal average of longitudinal distribution of R_{AOD}

Fig. 6.2 illustrates the seasonal variations in the R_{AOD} across different longitudes (125°E to 180°E) using data from three distinct sources: MODIS, MERRA-2, and SPRINTARS. Each panel corresponds to a different season: spring (MAM), summer (JJA), autumn (SON), and winter (DJF), showing how R_{AOD} values change geographically from the eastern coast of China eastward.

A clear trend observed across all datasets and seasons is an exponential decline in R_{AOD} values as longitude increases. This pattern indicates a decrease in aerosol concentrations moving away from continental sources toward the

Pacific, potentially driven by atmospheric dispersion and prevailing wind patterns. The slope of these trends varies seasonally, suggesting changes in aerosol sources or atmospheric conditions that affect aerosol transport and deposition.

In spring and winter, the slopes are generally smaller, indicating a less steep decrease in R_{AOD}. This may be influenced by stable atmospheric conditions that limit the dispersion of aerosols. Conversely, summer and autumn exhibit relatively steeper declines, possibly due to enhanced wind activity that aids in more efficient aerosol dispersion. This seasonal disparity in slopes could hint at the influence of monsoonal winds or other meteorological factors that vary throughout the year, affecting aerosol distribution patterns over the downwind of China.

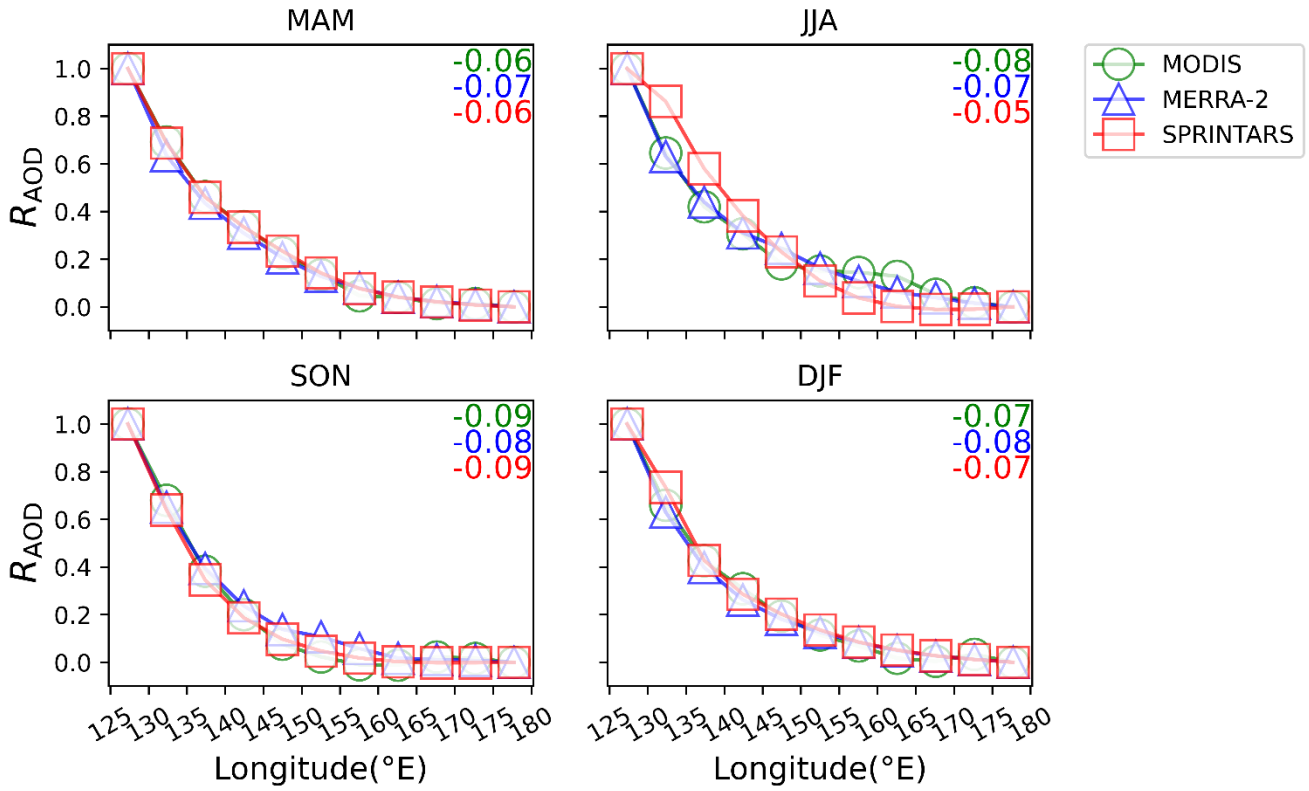

Fig. 6.2 Seasonal variation in the R_{AOD} across longitudes range of 125°E to 180°E for various datasets during the year. Each panel represents a different season: spring (MAM; March-April-May), summer (JJA; June-July-August), autumn (SON; September-October-November), and winter (DJF; December-January-February). The datasets shown are MODIS (green circles), MERRA-2 (blue triangles), and SPRINTARS (red squares). Numerical values in the top right corner of each panel indicate the linear regression slope (deg^{-1}) of R_{AOD} trends for each dataset for each season.

6.2. Interannual variation of R_{AOD}

To analyze the spatial and temporal interannual variation of R_{AOD} along a longitudinal axis from 2003 to 2021, a Hovmöller diagram was employed by using MODIS, MERRA-2, and SPRINTARS datasets (Fig. 6.3). This pattern is visually represented by a color gradient that transitions from red to green and then to blue, reflecting the trend shown in Fig. 6.3.

Throughout the 2003 to 2021 period, R_{AOD} exhibited significant fluctuations from year to year. Despite these fluctuations, there was notable consistency in the data patterns from the MODIS and MERRA-2 datasets. Particularly in the MODIS dataset, R_{AOD} values around 0.1 to 0.2 in light blue extended up to approximately 160°E during the years 2005, 2006, 2007, and 2013, indicating meteorological conditions favorable for transboundary air pollution.

In contrast, R_{AOD} values also ranged from 0.1 to 0.2 but were observed around 145°E in 2018, suggesting that aerosols tended to deposit closer to the eastern coast of China. The SPRINTARS dataset is also consistent with the annual patterns observed in MODIS and MERRA-2.

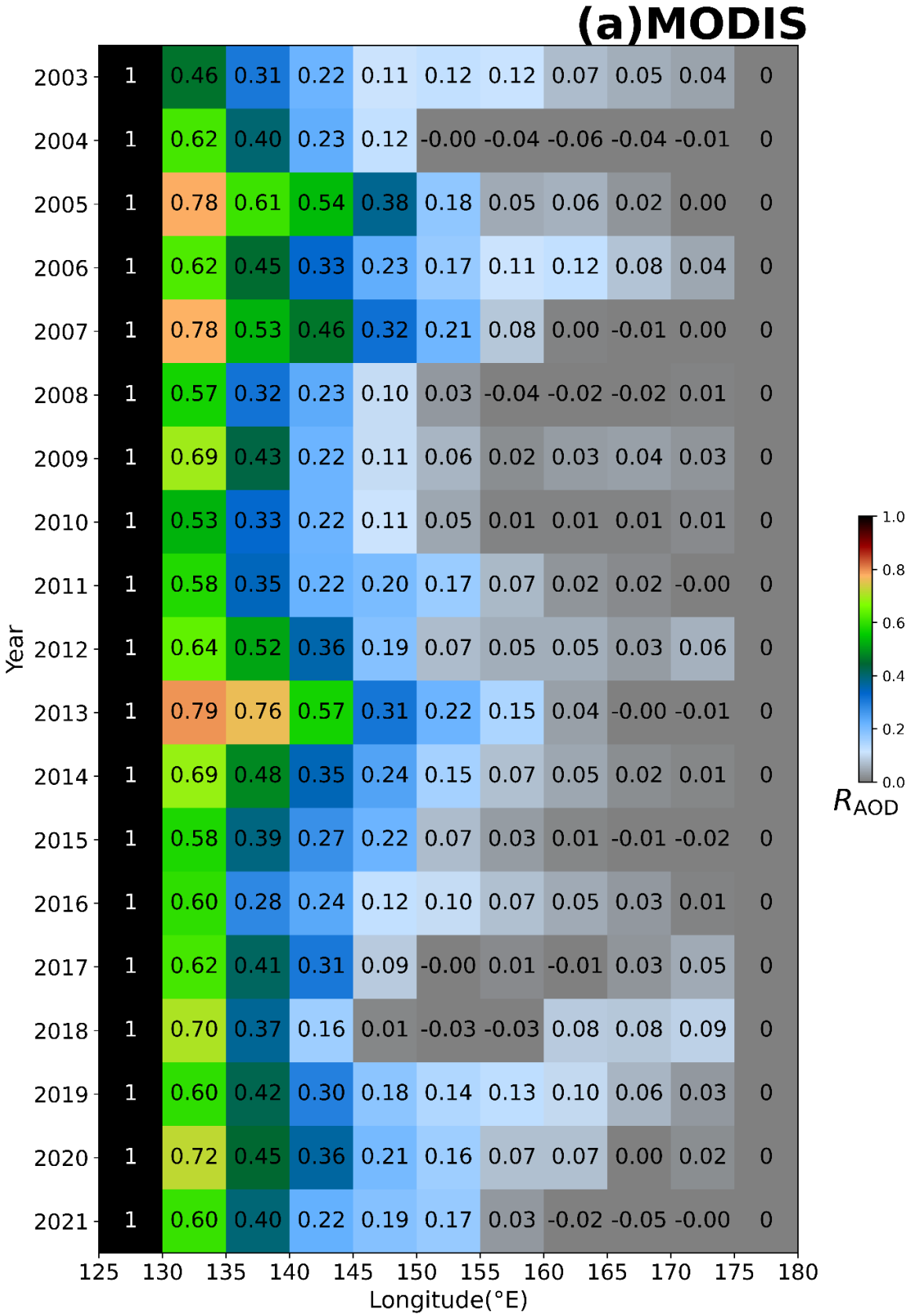
(a)MODIS
Year
2003 1 0.46 0.31 0.22 0.11 0.12 0.12 0.07 0.05 0.04 0
2004 1 0.62 0.40 0.23 0.12 -0.00 -0.04 -0.06 -0.04 -0.01 0
2005 1 0.78 0.61 0.54 0.38 0.18 0.05 0.06 0.02 0.00 0
2006 1 0.62 0.45 0.33 0.23 0.17 0.11 0.12 0.08 0.04 0
2007 1 0.78 0.53 0.46 0.32 0.21 0.08 0.00 -0.01 0.00 0
2008 1 0.57 0.32 0.23 0.10 0.03 -0.04 -0.02 -0.02 0.01 0
2009 1 0.69 0.43 0.22 0.11 0.06 0.02 0.03 0.04 0.03 0
2010 1 0.53 0.33 0.22 0.11 0.05 0.01 0.01 0.01 0.01 0
2011 1 0.58 0.35 0.22 0.20 0.17 0.07 0.02 0.02 -0.00 0
2012 1 0.64 0.52 0.36 0.19 0.07 0.05 0.05 0.03 0.06 0
2013 1 0.79 0.76 0.57 0.31 0.22 0.15 0.04 -0.00 -0.01 0
2014 1 0.69 0.48 0.35 0.24 0.15 0.07 0.05 0.02 0.01 0
2015 1 0.58 0.39 0.27 0.22 0.07 0.03 0.01 -0.01 -0.02 0
2016 1 0.60 0.28 0.24 0.12 0.10 0.07 0.05 0.03 0.01 0
2017 1 0.62 0.41 0.31 0.09 -0.00 0.01 -0.01 0.03 0.05 0
2018 1 0.70 0.37 0.16 0.01 -0.03 -0.03 0.08 0.08 0.09 0
2019 1 0.60 0.42 0.30 0.18 0.14 0.13 0.10 0.06 0.03 0
2020 1 0.72 0.45 0.36 0.21 0.16 0.07 0.07 0.00 0.02 0
2021 1 0.60 0.40 0.22 0.19 0.17 0.03 -0.02 -0.05 -0.00 0
125 130 135 140 145 150 155 160 165 170 175 180
Longitude(°E)
1.0
0.8
0.6
0.4
0.2
0.0
R_{AOD}

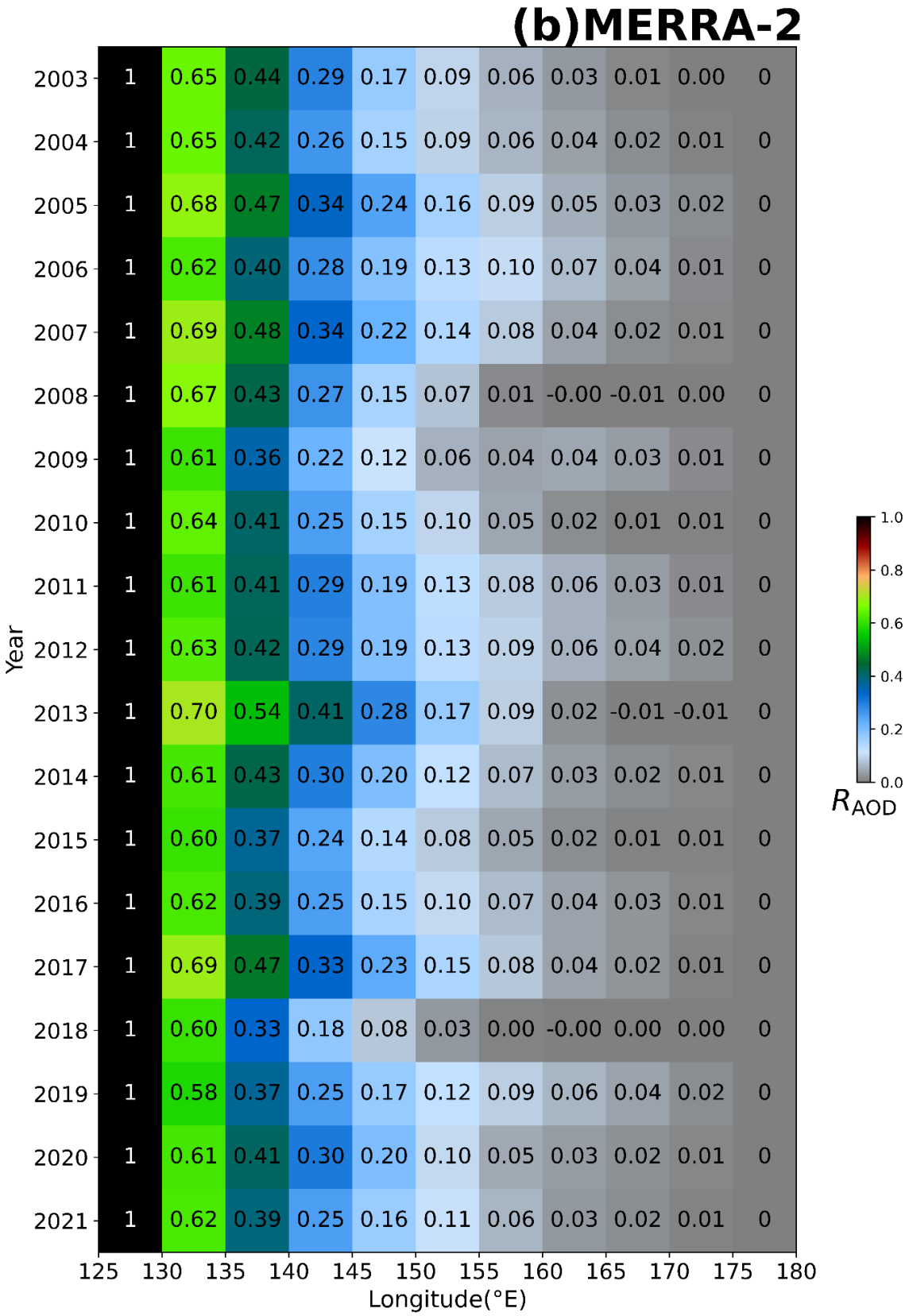
(b)MERRA-2
2003 1 0.65 0.44 0.29 0.17 0.09 0.06 0.03 0.01 0.00 0
2004 1 0.65 0.42 0.26 0.15 0.09 0.06 0.04 0.02 0.01 0
2005 1 0.68 0.47 0.34 0.24 0.16 0.09 0.05 0.03 0.02 0
2006 1 0.62 0.40 0.28 0.19 0.13 0.10 0.07 0.04 0.01 0
2007 1 0.69 0.48 0.34 0.22 0.14 0.08 0.04 0.02 0.01 0
2008 1 0.67 0.43 0.27 0.15 0.07 0.01 -0.00 -0.01 0.00 0
2009 1 0.61 0.36 0.22 0.12 0.06 0.04 0.04 0.03 0.01 0
2010 1 0.64 0.41 0.25 0.15 0.10 0.05 0.02 0.01 0.01 0
2011 1 0.61 0.41 0.29 0.19 0.13 0.08 0.06 0.03 0.01 0
2012 1 0.63 0.42 0.29 0.19 0.13 0.09 0.06 0.04 0.02 0
2013 1 0.70 0.54 0.41 0.28 0.17 0.09 0.02 -0.01 -0.01 0
2014 1 0.61 0.43 0.30 0.20 0.12 0.07 0.03 0.02 0.01 0
2015 1 0.60 0.37 0.24 0.14 0.08 0.05 0.02 0.01 0.01 0
2016 1 0.62 0.39 0.25 0.15 0.10 0.07 0.04 0.03 0.01 0
2017 1 0.69 0.47 0.33 0.23 0.15 0.08 0.04 0.02 0.01 0
2018 1 0.60 0.33 0.18 0.08 0.03 0.00 -0.00 0.00 0.00 0
2019 1 0.58 0.37 0.25 0.17 0.12 0.09 0.06 0.04 0.02 0
2020 1 0.61 0.41 0.30 0.20 0.10 0.05 0.03 0.02 0.01 0
2021 1 0.62 0.39 0.25 0.16 0.11 0.06 0.03 0.02 0.01 0
Year
125 130 135 140 145 150 155 160 165 170 175 180
Longitude(°E)
1.0
0.8
0.6
0.4
0.2
0.0
R_{AOD}

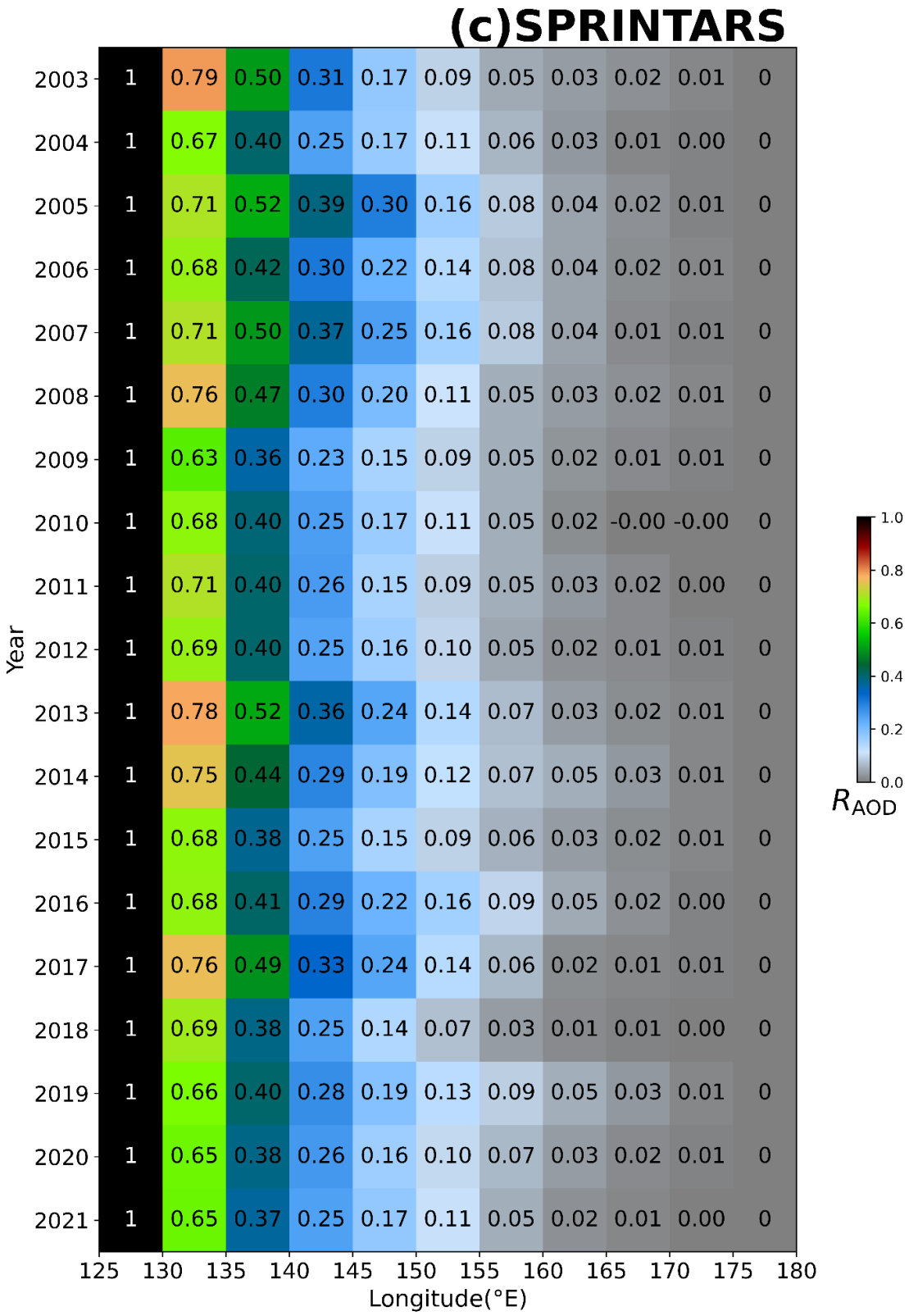

Fig. 6.3 Hovmöller diagram depicting annual average R_{AOD} values within the longitudinal range of 125–180°E using (a) MODIS, (b) MERRA-2, and (c) SPRINTARS data from 2003 to 2021.

6.3. Analysis for the linear regression slope of the R_{AOD}

6.3.1. Monthly and annual variation in the slope of R_{AOD}

To conduct a detailed analysis of interannual variations in meteorological conditions, this study focused on R_{AOD} within the longitudinal range of 125–150°E. This specific range was chosen because it exhibits high R_{AOD} variability, as shown in Table 6.1. The table lists R_{AOD} values derived from three distinct data sets: MODIS, MERRA-2, and SPRINTARS. These values are documented for each 5° interval across the broader longitudinal range of 125–180°E and the latitudinal range of 25–30°N from 2003 to 2021.

The data in Table 6.1 reveal that the MODIS and MERRA-2 datasets display similar R_{AOD} trends, suggesting consistent aerosol variations across the studied range. Notably, as the longitude approaches 150–155°E, there is an observable gradual decrease in R_{AOD} values, indicating diminishing aerosol concentrations moving further eastward. This pattern leads to a more leveled slope, suggesting a reduction in the eastward dispersion of aerosols over time.

Table 6.1. Comparison between R_{AOD} values from MODIS, MERRA-2, and SPRINTARS data for each 5° grid interval in the ranges 125–180°E and 25–30°N from 2003 to 2021, where n represents the number of grid intervals.

n	**1**	**4**	**6**	**8**	**11**
Longitude (°E)	**125-130**	**140-145**	**150-155**	**160-165**	**175-180**
MODIS	1	0.29	0.11	0.04	0
MERRA-2	1	0.27	0.12	0.04	0
SPRINTARS	1	0.30	0.11	0.02	0

To analyze the horizontal trend of decreasing R_{AOD} year-by-year as shown in Fig. 6.3, the monthly and annual slope of the regression line for R_{AOD} within the

longitude band of 125–150°E was calculated for each year from 2003 to 2021, using data from the MODIS, MERRA-2, and SPRINTARS datasets, as presented in Fig. 6.4. Linear regression was used to effectively capture the year-to-year fluctuations in R_{AOD} within this specific longitudinal range, where the trend is linear rather than curvilinear. The monthly average R_{AOD} was calculated by removing data points that deviated more than 0.01 from the previous month's value to enhance accuracy and consistency. The resulting refined monthly mean values are shown as individual dots, while the annual means are depicted with lines and markers (Fig. 6.4).

The monthly averages and their standard deviations for MODIS, MERRA-2, and SPRINTARS were recorded as -0.043 ± 0.012, -0.042 ± 0.012, and -0.042 ± 0.006, respectively. The data amount for the slope of R_{AOD} comprises 113, 184, and 204 for MODIS, MERRA-2, and SPRINTARS, respectively.

In Fig. 6.5, both MODIS and MERRA-2 datasets demonstrated consistent downward trends in the R_{AOD} slope over the 19-year period. Notably, the absolute value of the R_{AOD} slope was particularly high in 2018, indicating a significant decline in R_{AOD}, while the lowest values were recorded in 2005, 2007, and 2013. Earlier years showed a flatter slope, suggesting a predominant west-to-east movement of aerosols, consistent with the annual R_{AOD} patterns depicted in Fig. 6.3. In contrast, the steep slope in 2018 indicated that aerosols were more likely to settle near their sources, showing limited long-range transport, consistent with the R_{AOD} patterns observed that year.

Interannual variability in the R_{AOD} slope from SPRINTARS generally matched the observations from MODIS and MERRA-2. Additionally, a peak pattern in the meteorological field was noted approximately every eight years, as shown in Fig. 6.5. However, the East Asian Monsoon Index (EAMI) and the El Niño–Southern Oscillation (ENSO) were considered as potential drivers of this cyclic variation, but no clear correlation was established with the EAMI, and only a few

El Niño–La Niña events were reported by Gan et al., 2023, which left unclear whether there was a true connection.

These findings indicate that long-term changes in R_{AOD}, potentially influenced by climate change, were relatively minor and overshadowed by more pronounced year-to-year variations in the meteorological field. Therefore, detecting the effects of climate change on meteorological fields using R_{AOD} as a metric would require aerosol data spanning more than two decades.

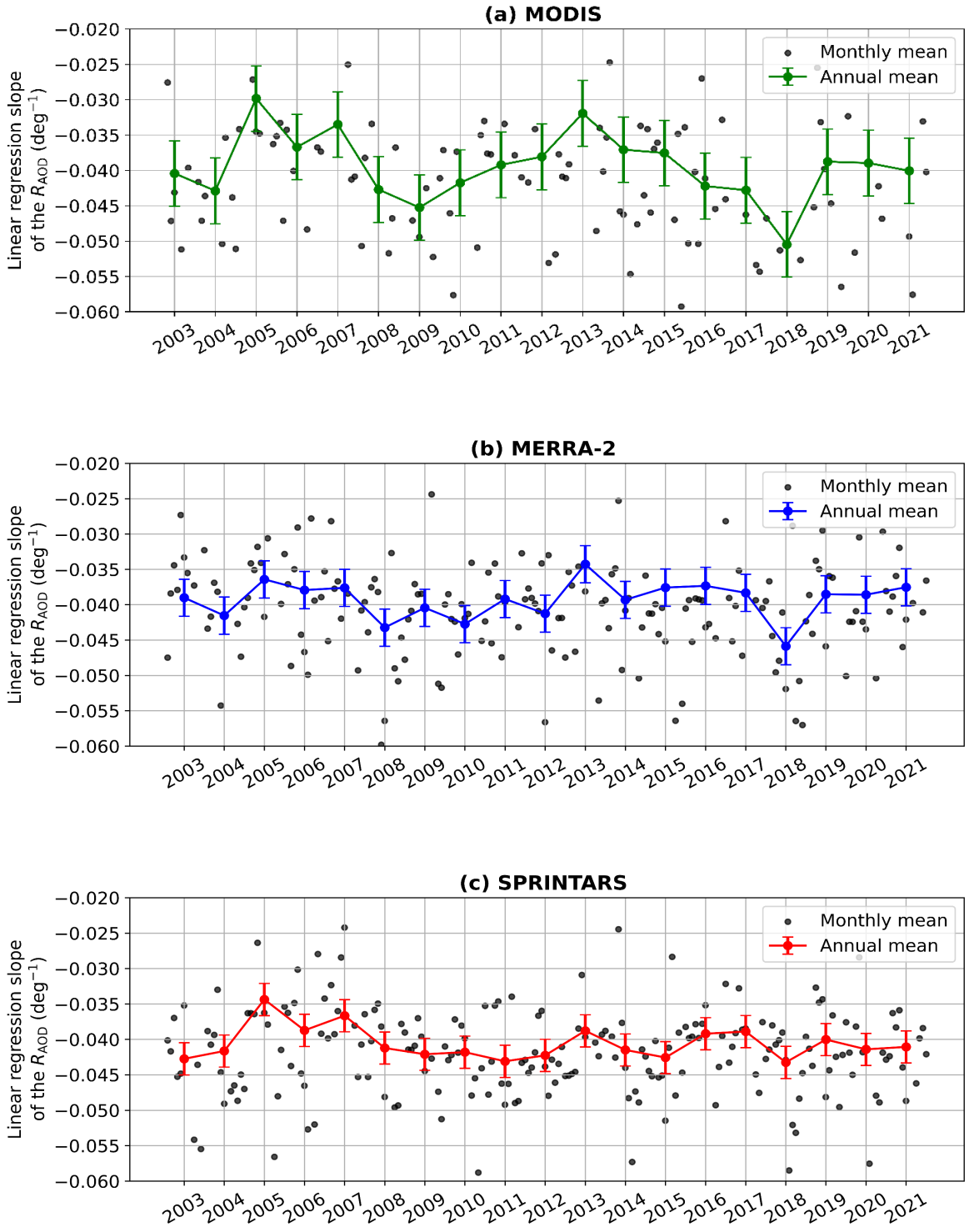

Fig. 6.4 Monthly and annual variations in the R_{AOD} slope of the linear regression (deg^{-1}) within the 125–150°E longitude band from 2003 to 2021, derived from (a) MODIS, (b) MERRA-2, and (c) SPRINTARS datasets. Each panel shows the monthly mean R_{AOD} values (indicated by individual dots) and the corresponding annual mean (line with markers). The monthly averages and their standard deviations for MODIS, MERRA-2, and SPRINTARS were -0.043 ± 0.012, -0.042 ± 0.012, and -0.042 ± 0.006, respectively.

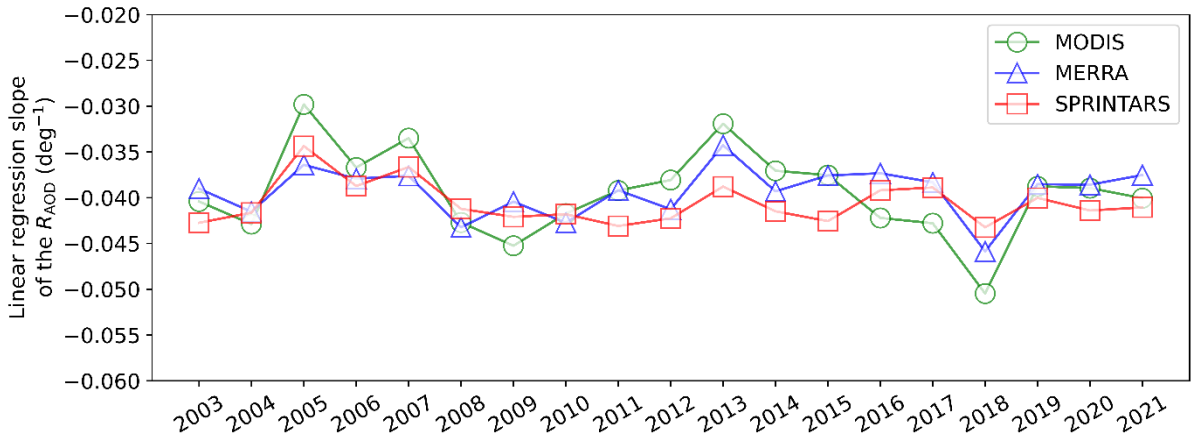

Fig. 6.5 Annual variations in the slope (deg^{-1}) of the linear regression of R_{AOD} in the 125–150°E longitude band from 2003 to 2021, based on MODIS, MERRA-2, and SPRINTARS data.

6.3.2. Seasonal variation in the slope of the R_{AOD}

Fig. 6.6 presents the (a) monthly and (b) seasonal variations in the regression line slope of R_{AOD} within the longitude band of 125–150°E from 2003 to 2021, based on data from MODIS, MERRA-2, and SPRINTARS. Monthly and seasonal variations are found to be consistent among MODIS, MERRA-2, and SPRINTARS. However, the monthly variations observed between July and September exhibit significant uncertainty, evidenced by the large error bars on the SPRINTARS data, represented by red lines in Fig. 6.6 (a).

A clear seasonal pattern is observed in the values of the R_{AOD} slope, which decreases from spring to summer and increases from autumn to winter. The slope of R_{AOD} represents the degree of reduction in the amounts of aerosols transported eastward. When the absolute value of the R_{AOD} slope is small, it indicates that aerosols are transported over longer distances, as observed in spring (March and April) and winter (December to February). Conversely, higher absolute slope values, such as those in summer (June) and autumn (October), suggest that aerosols are less likely to be transported eastward.

The variability in the slope of R_{AOD} is likely due to changes in atmospheric transport fields (Wu et al., 2013; Nguyen et al., 2019; Lee et al., 2022). To clarify the consistency between the atmospheric transport fields and the slope of R_{AOD}, the wind speed and wind direction will be analyzed in detail in the following section.

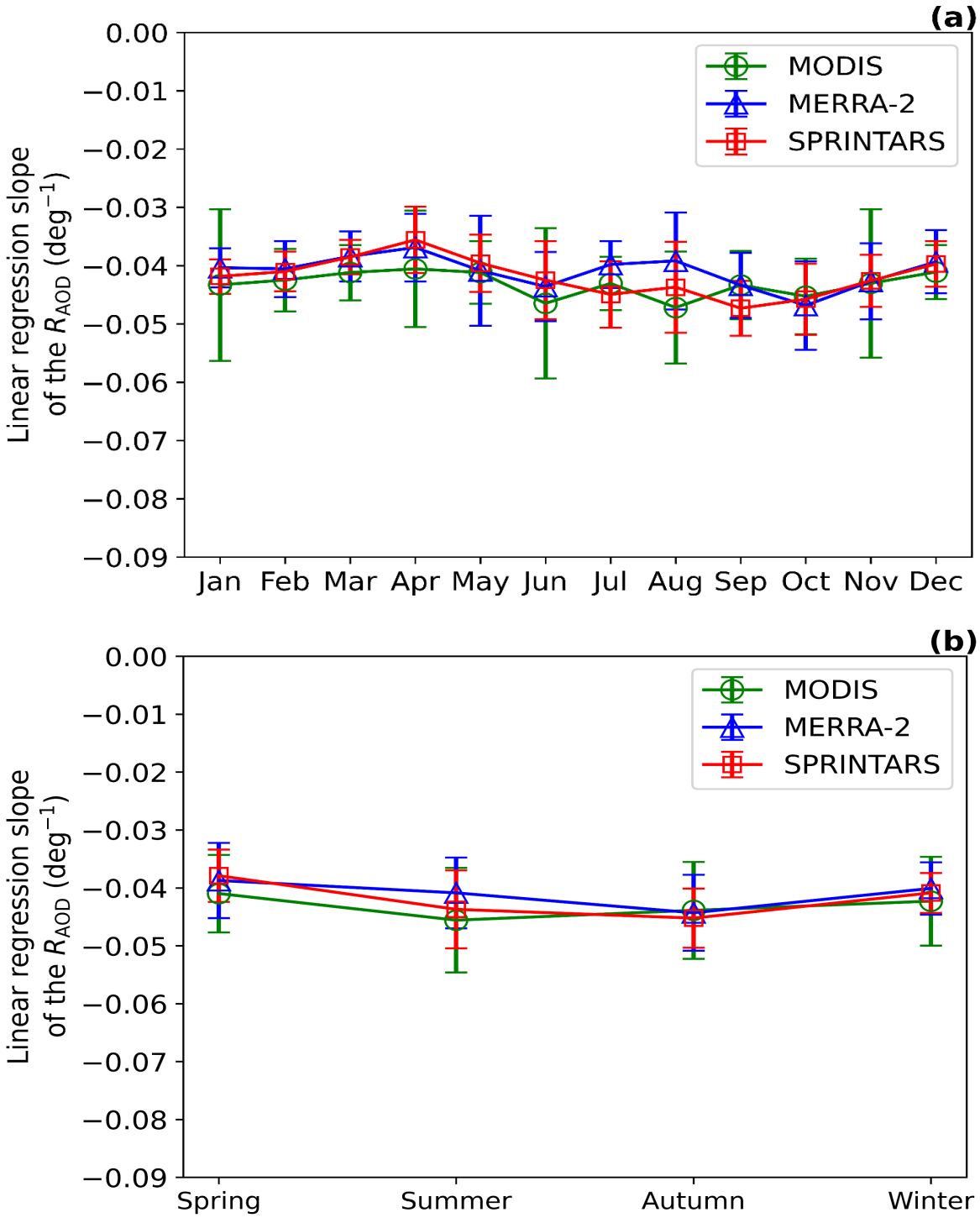

Fig. 6.6 (a) Monthly and (b) seasonal variations in the slope (deg^{-1}) of the regression line for R_{AOD} within the 25–30°N and 125–150°E range from 2003 to 2021, based on MODIS (green circles), MERRA-2 (blue triangles), and SPRINTARS (red squares) data. The error bars represent the standard deviation of the data.

6.4. Wind analysis in atmospheric transport fields

The monthly variation (Fig. 6.7) and seasonal variation (Fig. 6.8) in wind speed (measured in m/s) and direction at the 500 hPa level were analyzed using MERRA-2 data from 2003 to 2021. Despite significant monthly variability in the wind field, there is a pronounced seasonal pattern in wind direction, predominantly facilitating west-to-east transport during the spring and winter seasons, as depicted in Fig. 6.8.

In spring (Fig. 6.8(a)) and winter (Fig. 6.8(d)), there is strong west-to-east transport, whereas in summer (Fig. 6.8(b)) and autumn (Fig. 6.8(c)), there is a tendency for transport to be more northward. These results are consistent with the patterns observed in the absolute values of the R_{AOD} slope within the longitude band of 125–150°E (Fig. 6.6). In spring and winter, the absolute value of the R_{AOD} slope is smaller, indicating that aerosols are transported over longer distances. Conversely, in summer and autumn, the absolute value of the R_{AOD} slope is larger, indicating a tendency for less long-range eastward transport. From these findings, the seasonal variation in atmospheric transport fields is consistent with the slope of R_{AOD}. Therefore, the longitudinal and seasonal analysis indicated that R_{AOD} has the potential to detect long-term changes in atmospheric transport fields.

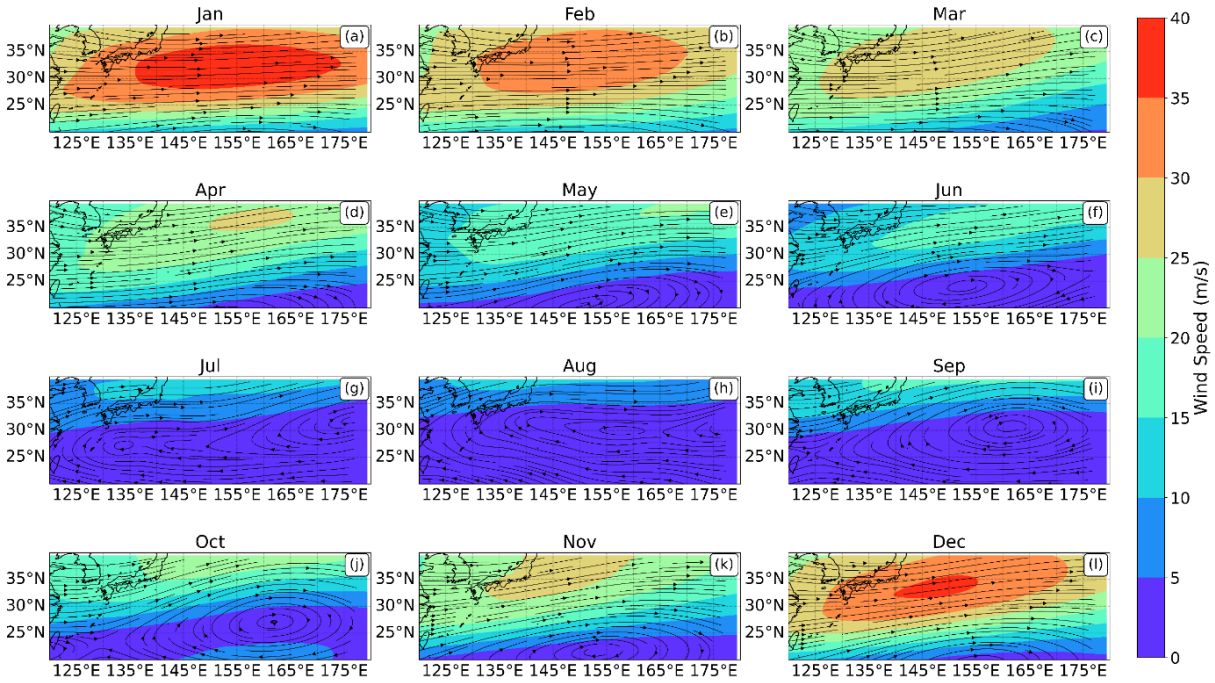

Fig. 6.7 Monthly wind speed (m/s) and direction at 500 hPa for the period 2003 to 2021, represented for each month (a–l) as calculated from MERRA-2 data. Color shading indicates wind speed (m/s), and quivers depict wind direction.

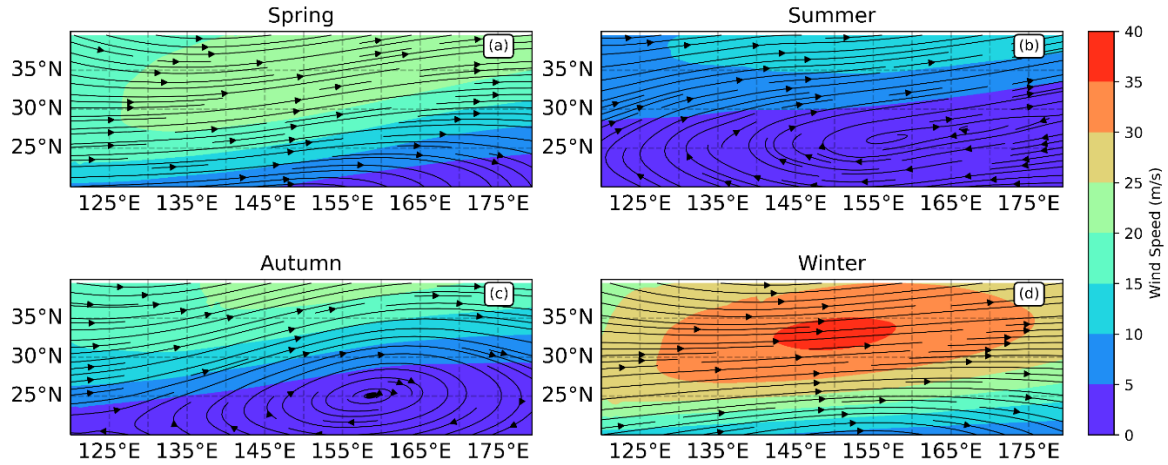

Fig. 6.8 Seasonal wind speed (m/s) and direction at 500 hPa for the period 2003–2021, represented for (a) spring, (b) summer, (c) autumn, and (d) winter as calculated from MERRA-2 data. The color shading indicates wind speed (m/s), and the quivers depict wind direction.

6.5. Long-term variations in atmospheric transport fields

To investigate recent variations in the atmospheric transport fields, a long-term trend analysis of R_{AOD} was analyzed. The longitudinal distribution of the 6-year average R_{AOD} was analyzed using data from MODIS, MERRA-2, and SPRINTARS for three periods: 2003–2008, 2009–2014, and 2015–2021 (Fig. 6.9). The analysis showed a significant decreasing trend in R_{AOD} values when compared at the same longitudes over the temporal span of the study. Furthermore, we observed a clear trend that the longitudinal distance of R_{AOD} to reach a specified threshold value (e.g., 0.2) gradually decreased over time. It has been observed that the distance over which aerosol concentration decrease by 20% has been shortened in recent years (2015–2021). This trend can be explained by a slight northward shift in the transboundary air pollution pathways in recent years.

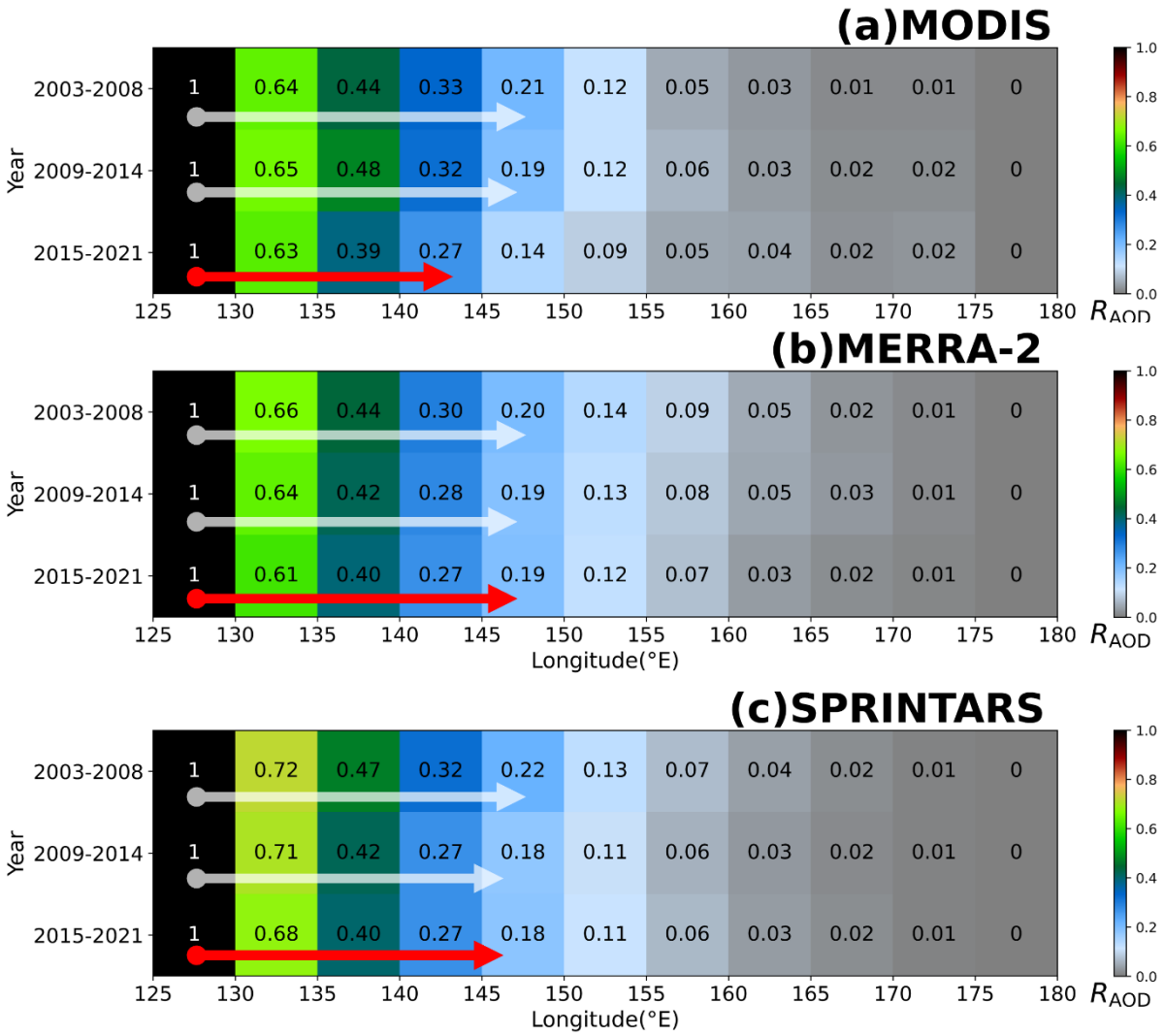

Fig. 6.9 Hovmöller diagram depicting 6-year average R_{AOD} values within the longitudinal range of 125–180°E using (a) MODIS, (b) MERRA-2, and (c) SPRINTARS data during three periods: 2003–2013, 2009–2014, and 2015–2021. The arrows indicate the range where R_{AOD} decreases from 1 to 0.2.

6.6. Summary

Emissions, cloud cover, and atmospheric transport field changes significantly influence the variability of R_{AOD}. There is no correlation between the R_{AOD} and AOD value near emission sources from 2003 to 2021, indicating that R_{AOD} can offset the temporal changes in China's emissions. The R_{AOD} from MODIS, MERRA-2, and SPRINTARS datasets show a consistent trend, with an exponential decrease in R_{AOD} values extending from the eastern coast of China across the longitudinal range of 125–180°E. These results indicate that emissions and cloud cover do not significantly affect R_{AOD} variations, highlighting that the changes in the atmospheric transport field play a dominant role in transboundary air pollution.

Seasonal variations in atmospheric transport fields are consistent with the slope of R_{AOD} within the 125–150°E longitude band. In spring and winter, aerosols are predominantly transported from west to east, consistent with the lower absolute values of R_{AOD} slopes. Conversely, during summer and autumn, wind patterns shift slightly northward, consistent with higher absolute values of R_{AOD} slopes, indicating aerosols cannot transport. These findings suggested that R_{AOD}, which uses aerosols as tracers, has the potential to detect long-term changes in atmospheric transport fields.

Long-term variations in atmospheric transport fields were analyzed, and we found that the distance over which aerosol concentrations decrease by 20% has shortened, which can be explained by a slight northward shift in the transboundary air pollution pathways in recent years.

Chapter 7. Northward shift of transboundary air pollution pathway associated with climate change in recent decades

Chapter 6 suggested that the eastward transport distance of aerosols has been shortened. Two factors can affect the shortening of the transport distance of aerosols: aerosol composition and the northward shift of transboundary air pollution pathways. Since aerosols contain various components, their composition's lifetime may affect the transport distance. The purpose of this chapter is to clarify if the transboundary air pollution pathway has shifted northward in recent decades. It is necessary to minimize the influence of aerosol component lifetimes on the eastward transport distance. And the analysis period was extended to 21 years (2003–2023), and the R_{AOD} for each component was analyzed.

7.1. Longitudinal distribution of R_{AOD} for each component

We analyzed the longitudinal distribution of R_{AOD} for both coarse particles and fine anthropogenic aerosols (Fig. 7.1). The analysis utilized MERRA-2 AOD data for black carbon (BC), organic carbon (OC), sulfate (SO_4^{2-}), and dust, covering a 21-year period from 2003 to 2023. Marine contributions from DMS and organic matter were also considered when calculating the R_{AOD} for each component.

The R_{AOD} curves for total AOD, BC, OC, and SO_4^{2-} exhibit similar and consistent patterns, suggesting that the compositional origins of R_{AOD} in the downwind regions of China are predominantly from anthropogenic aerosols. Furthermore, this similarity indicates that the longitudinal distribution of R_{AOD} for

anthropogenic particles is not significantly influenced by differences in the lifetimes of these particle types. Additionally, the R_{AOD_Dust} does not fit well, and the values around 145°E are negative. This indicates that dust transport is minimal in the Pacific region downwind of China. Even if a transport event were to occur, the large particle size of the dust would result in rapid deposition. Consequently, the R_{AOD_Dust} was not statistically significant in this study. Moreover, this discussion highlights the reliability and effectiveness of R_{AOD} as a metric to be an indicator of aerosol transport from the eastern coast of China.

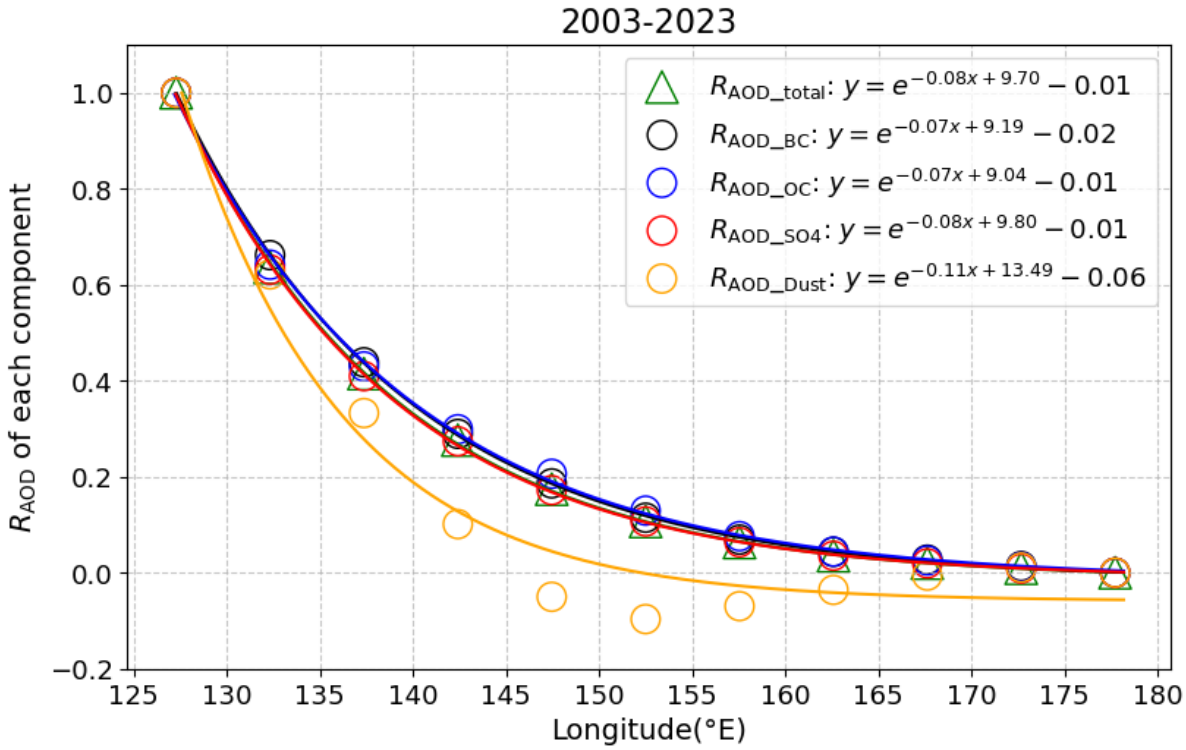

Fig. 7.1 Longitudinal distribution of R_{AOD} for total AOD (green circles), SO_4 (red circles), BC (black circles) and OC (blue circles), and Dust (yellow circles) which represented by R_{AOD_total}, $R_{AOD\_SO_4^{2-}}$, R_{AOD_BC}, R_{AOD_OC} and R_{AOD_Dust}, respectively. The data are from MERRA-2 and divided into 5° intervals over the range of 25–30°N and 125–180°E during from 2003 to 2023. The curve of R_{AOD} derived from exponential fitting, with slopes of −0.08 for both total AOD and SO_4^{2-}, -0.07 for both BC and OC, and -0.11 for dust.

7.2. Annual variation of R_{AOD} for each component

To analyze the spatial and temporal annual variation of R_{AOD} for each component from 2003 to 2023, a Hovmöller diagram was employed by using MERRA-2 data, which is depicted in Fig. 7.2. This pattern is visually represented by a color gradient that transitions from black to green and then to blue. The year-to-year variation of anthropogenic aerosols R_{AOD} ($R_{AOD\_SO_4^{2-}}$, R_{AOD_BC} and R_{AOD_OC}) and total AOD are consistent, suggesting that the main source of R_{AOD} in the downwind area of China predominantly comes from anthropogenic aerosols

Despite the large year-to-year fluctuation in R_{AOD} from 2003 to 2023, a notable consistency was observed between the total AOD of R_{AOD} and $R_{AOD\_SO_4^{2-}}$. The total AOD of R_{AOD} and $R_{AOD\_SO_4^{2-}}$ values extend to around 150–155°E in light blue and range from 0.1 to 0.2 during 2005, 2007, 2013, 2017, and 2019, indicating meteorological conditions suitable for air transportation from the eastern coast of China. In contrast, in 2009 and 2018, the total AOD of R_{AOD} and $R_{AOD\_SO_4^{2-}}$ values suggesting a tendency for less eastward aerosol transport. The trends in R_{AOD_BC} and R_{AOD_OC} also showed similar patterns, with years such as 2005, 2012, 2017, and 2019 showing conditions suitable for eastward aerosol transport. However, there was a tendency for reduced eastward aerosol transport in 2009, 2015, 2016, and 2018.

To clearly observe the annual variation in R_{AOD} from 2003 to 2023, particularly within the longitudinal band of 125–130°E, the slope (deg^{-1}) of the linear regression of R_{AOD} was analyzed (Fig. 7.3). The annual variation in the slope of $R_{AOD\_SO_4^{2-}}$ was consistent with the slope of R_{AOD}, indicating that the composition of aerosols transported downwind from China has remained unchanged, with SO_4^{2-} remaining the dominant component in recent years. This trend was also observed for R_{AOD_BC} and R_{AOD_OC}, despite their relatively smaller contribution to total AOD.

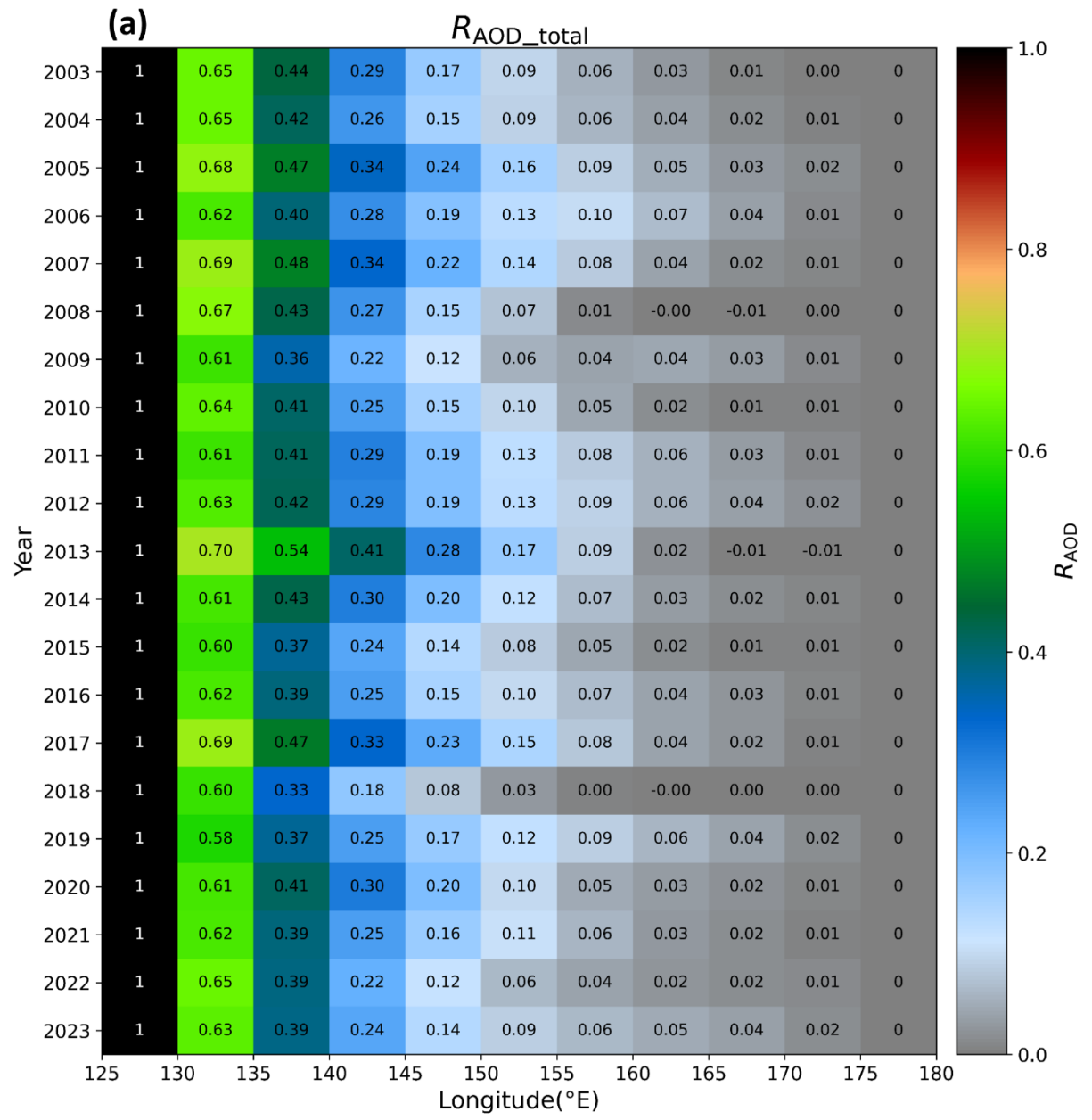
(a)
R_{AOD_total}
Year
Longitude(°E)
R_{AOD}
2003 1 0.65 0.44 0.29 0.17 0.09 0.06 0.03 0.01 0.00 0
2004 1 0.65 0.42 0.26 0.15 0.09 0.06 0.04 0.02 0.01 0
2005 1 0.68 0.47 0.34 0.24 0.16 0.09 0.05 0.03 0.02 0
2006 1 0.62 0.40 0.28 0.19 0.13 0.10 0.07 0.04 0.01 0
2007 1 0.69 0.48 0.34 0.22 0.14 0.08 0.04 0.02 0.01 0
2008 1 0.67 0.43 0.27 0.15 0.07 0.01 -0.00 -0.01 0.00 0
2009 1 0.61 0.36 0.22 0.12 0.06 0.04 0.04 0.03 0.01 0
2010 1 0.64 0.41 0.25 0.15 0.10 0.05 0.02 0.01 0.01 0
2011 1 0.61 0.41 0.29 0.19 0.13 0.08 0.06 0.03 0.01 0
2012 1 0.63 0.42 0.29 0.19 0.13 0.09 0.06 0.04 0.02 0
2013 1 0.70 0.54 0.41 0.28 0.17 0.09 0.02 -0.01 -0.01 0
2014 1 0.61 0.43 0.30 0.20 0.12 0.07 0.03 0.02 0.01 0
2015 1 0.60 0.37 0.24 0.14 0.08 0.05 0.02 0.01 0.01 0
2016 1 0.62 0.39 0.25 0.15 0.10 0.07 0.04 0.03 0.01 0
2017 1 0.69 0.47 0.33 0.23 0.15 0.08 0.04 0.02 0.01 0
2018 1 0.60 0.33 0.18 0.08 0.03 0.00 -0.00 0.00 0.00 0
2019 1 0.58 0.37 0.25 0.17 0.12 0.09 0.06 0.04 0.02 0
2020 1 0.61 0.41 0.30 0.20 0.10 0.05 0.03 0.02 0.01 0
2021 1 0.62 0.39 0.25 0.16 0.11 0.06 0.03 0.02 0.01 0
2022 1 0.65 0.39 0.22 0.12 0.06 0.04 0.02 0.02 0.01 0
2023 1 0.63 0.39 0.24 0.14 0.09 0.06 0.05 0.04 0.02 0
125 130 135 140 145 150 155 160 165 170 175 180
1.0 0.8 0.6 0.4 0.2 0.0

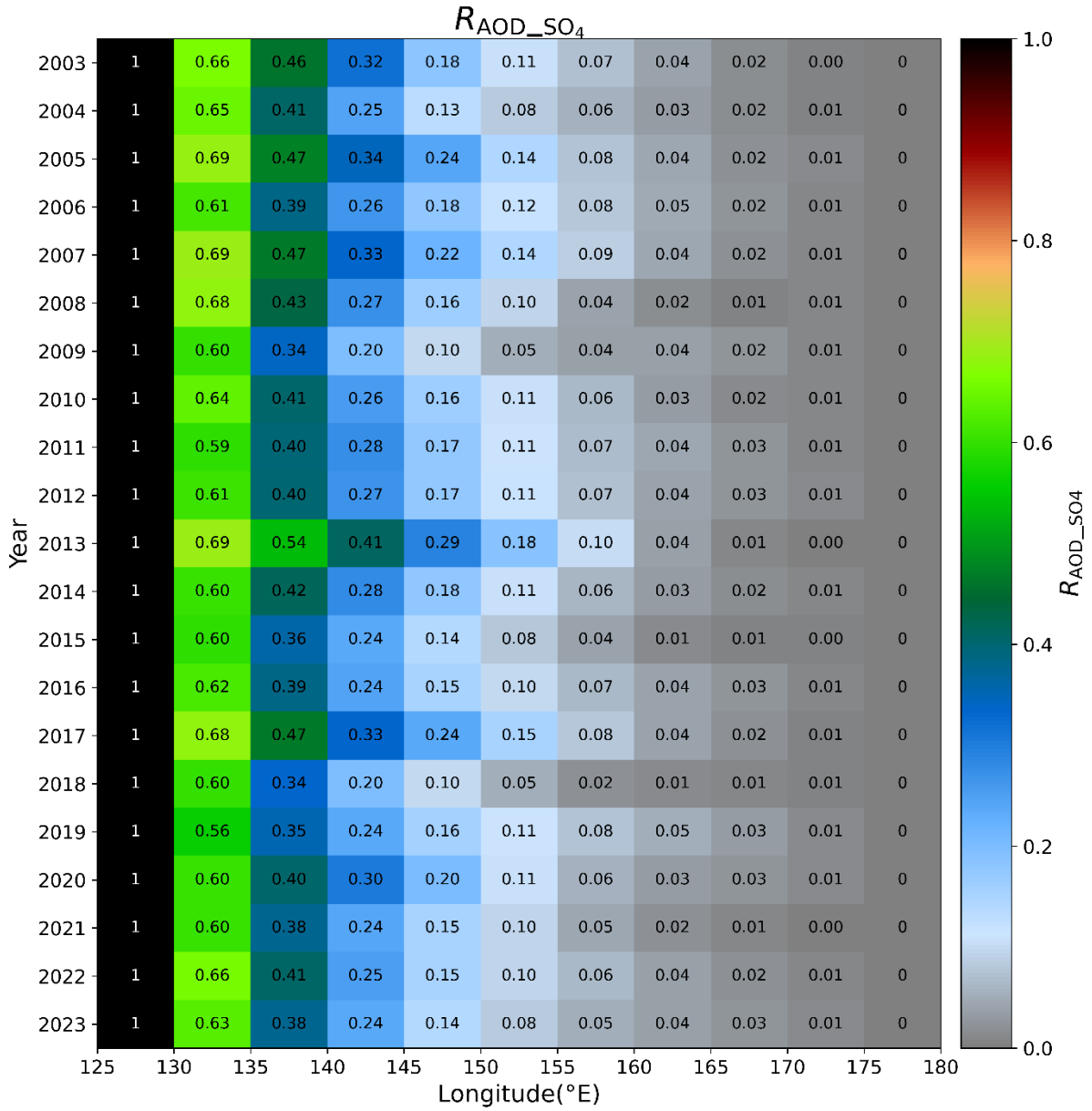
$R_{AOD\_SO_4}$
Year
2003 1 0.66 0.46 0.32 0.18 0.11 0.07 0.04 0.02 0.00 0
2004 1 0.65 0.41 0.25 0.13 0.08 0.06 0.03 0.02 0.01 0
2005 1 0.69 0.47 0.34 0.24 0.14 0.08 0.04 0.02 0.01 0
2006 1 0.61 0.39 0.26 0.18 0.12 0.08 0.05 0.02 0.01 0
2007 1 0.69 0.47 0.33 0.22 0.14 0.09 0.04 0.02 0.01 0
2008 1 0.68 0.43 0.27 0.16 0.10 0.04 0.02 0.01 0.01 0
2009 1 0.60 0.34 0.20 0.10 0.05 0.04 0.04 0.02 0.01 0
2010 1 0.64 0.41 0.26 0.16 0.11 0.06 0.03 0.02 0.01 0
2011 1 0.59 0.40 0.28 0.17 0.11 0.07 0.04 0.03 0.01 0
2012 1 0.61 0.40 0.27 0.17 0.11 0.07 0.04 0.03 0.01 0
2013 1 0.69 0.54 0.41 0.29 0.18 0.10 0.04 0.01 0.00 0
2014 1 0.60 0.42 0.28 0.18 0.11 0.06 0.03 0.02 0.01 0
2015 1 0.60 0.36 0.24 0.14 0.08 0.04 0.01 0.01 0.00 0
2016 1 0.62 0.39 0.24 0.15 0.10 0.07 0.04 0.03 0.01 0
2017 1 0.68 0.47 0.33 0.24 0.15 0.08 0.04 0.02 0.01 0
2018 1 0.60 0.34 0.20 0.10 0.05 0.02 0.01 0.01 0.01 0
2019 1 0.56 0.35 0.24 0.16 0.11 0.08 0.05 0.03 0.01 0
2020 1 0.60 0.40 0.30 0.20 0.11 0.06 0.03 0.03 0.01 0
2021 1 0.60 0.38 0.24 0.15 0.10 0.05 0.02 0.01 0.00 0
2022 1 0.66 0.41 0.25 0.15 0.10 0.06 0.04 0.02 0.01 0
2023 1 0.63 0.38 0.24 0.14 0.08 0.05 0.04 0.03 0.01 0
125 130 135 140 145 150 155 160 165 170 175 180
Longitude(°E)
1.0 0.8 0.6 0.4 0.2 0.0
R_{AOD_SO4}

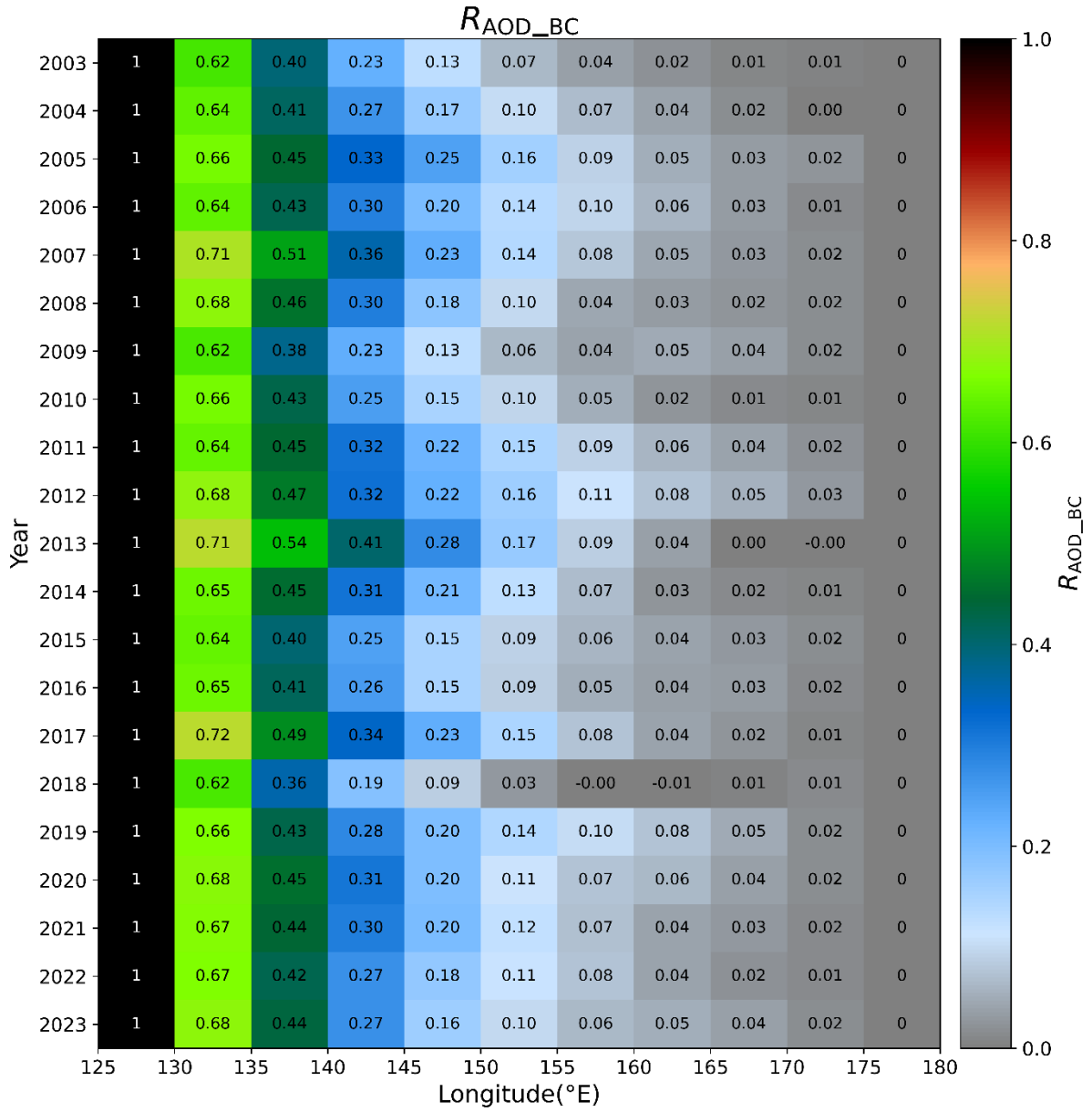
R_{AOD_BC}
Year
Longitude(°E)
2003 1 0.62 0.40 0.23 0.13 0.07 0.04 0.02 0.01 0.01 0
2004 1 0.64 0.41 0.27 0.17 0.10 0.07 0.04 0.02 0.00 0
2005 1 0.66 0.45 0.33 0.25 0.16 0.09 0.05 0.03 0.02 0
2006 1 0.64 0.43 0.30 0.20 0.14 0.10 0.06 0.03 0.01 0
2007 1 0.71 0.51 0.36 0.23 0.14 0.08 0.05 0.03 0.02 0
2008 1 0.68 0.46 0.30 0.18 0.10 0.04 0.03 0.02 0.02 0
2009 1 0.62 0.38 0.23 0.13 0.06 0.04 0.05 0.04 0.02 0
2010 1 0.66 0.43 0.25 0.15 0.10 0.05 0.02 0.01 0.01 0
2011 1 0.64 0.45 0.32 0.22 0.15 0.09 0.06 0.04 0.02 0
2012 1 0.68 0.47 0.32 0.22 0.16 0.11 0.08 0.05 0.03 0
2013 1 0.71 0.54 0.41 0.28 0.17 0.09 0.04 0.00 -0.00 0
2014 1 0.65 0.45 0.31 0.21 0.13 0.07 0.03 0.02 0.01 0
2015 1 0.64 0.40 0.25 0.15 0.09 0.06 0.04 0.03 0.02 0
2016 1 0.65 0.41 0.26 0.15 0.09 0.05 0.04 0.03 0.02 0
2017 1 0.72 0.49 0.34 0.23 0.15 0.08 0.04 0.02 0.01 0
2018 1 0.62 0.36 0.19 0.09 0.03 -0.00 -0.01 0.01 0.01 0
2019 1 0.66 0.43 0.28 0.20 0.14 0.10 0.08 0.05 0.02 0
2020 1 0.68 0.45 0.31 0.20 0.11 0.07 0.06 0.04 0.02 0
2021 1 0.67 0.44 0.30 0.20 0.12 0.07 0.04 0.03 0.02 0
2022 1 0.67 0.42 0.27 0.18 0.11 0.08 0.04 0.02 0.01 0
2023 1 0.68 0.44 0.27 0.16 0.10 0.06 0.05 0.04 0.02 0
125 130 135 140 145 150 155 160 165 170 175 180
1.0 0.8 0.6 0.4 0.2 0.0
R_{AOD_BC}

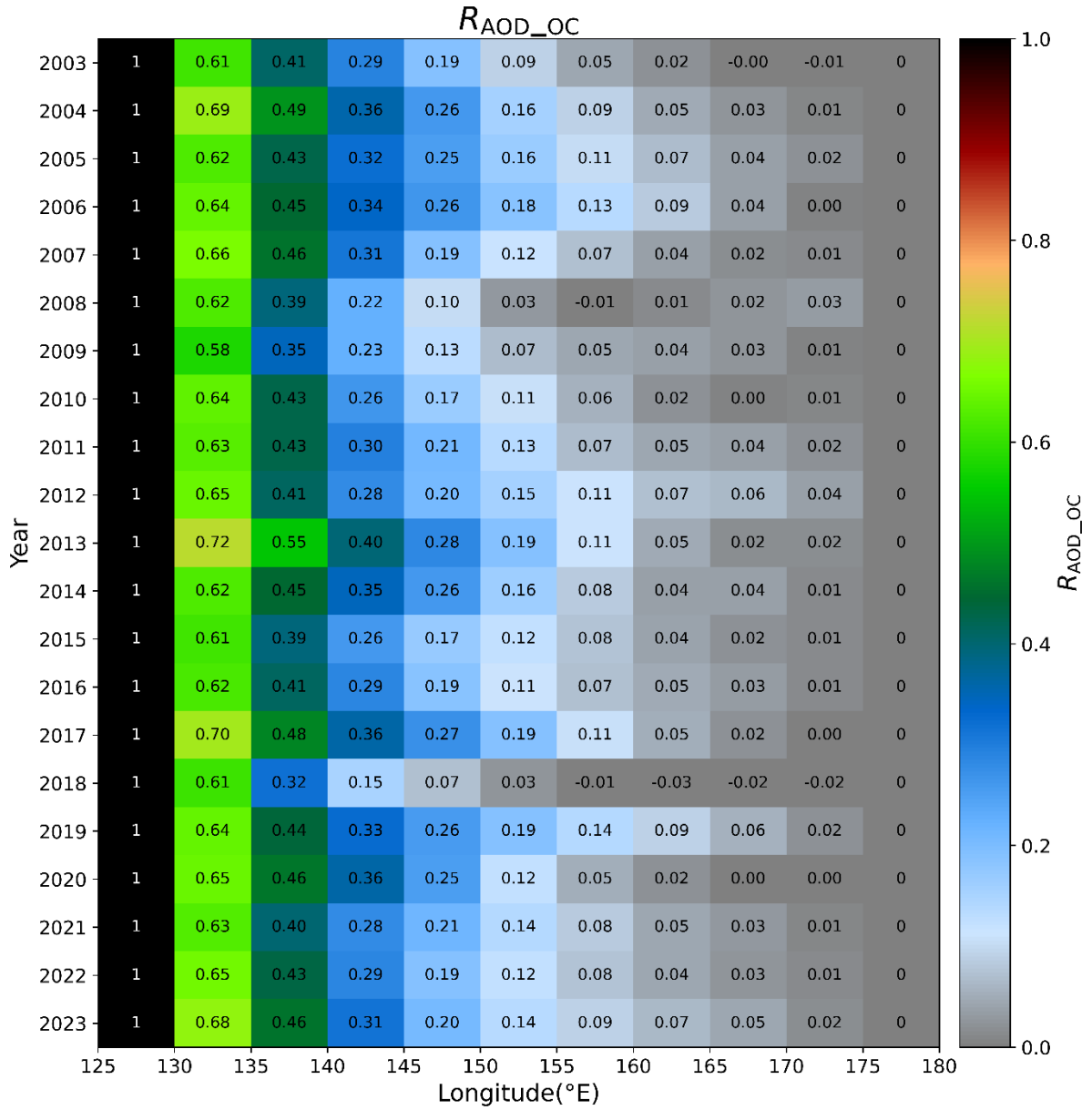

Fig. 7.2 Hovmöller diagram depicting longitudinal year-to-year variation of R_{AOD} for total AOD, SO_4, BC and OC, which represented by (a) R_{AOD_total}, (b) $R_{AOD\_SO_4^{2-}}$, (c) R_{AOD_BC}, (d) R_{AOD_OC}, respectively. The analysis using MERRA-2 data from 2003 to 2023 covers the longitudinal range of 125–180°E.

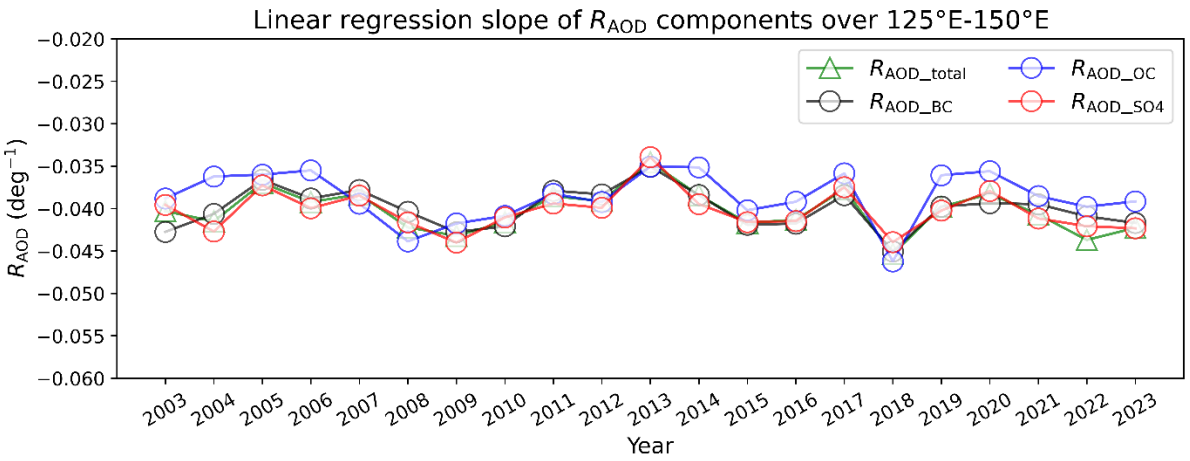

Fig. 7.3 Year-to-year variations in the slope (deg^{-1}) of the R_{AOD} linear regression for total AOD, SO_4^{2-}, BC and OC, represented by R_{AOD_total} (green triangle), $R_{AOD\_SO_4^{2-}}$ (red circle), R_{AOD_BC} (black circle), R_{AOD_OC} (blue circle), respectively. The analysis using MERRA-2 data from 2003 to 2023 covers the longitudinal range of 125–130°E.

7.3. Decadal trend of R_{AOD} for each component

To understand the transboundary air pollution pathway variations associated with climate change over the recent decades, we analyzed the 10-year means of R_{AOD} for each component by using MERRA-2 data during three periods: 2003–2013 and 2014–2023, as depicted in Fig. 7.4. R_{AOD} for each component showed a similar trend, with the distance over which aerosol concentration decreases by 20% has been shortened over the past decade. The composition of aerosols seems to have minimal impact on the eastward transport distance. Therefore, the eastward transport distance of aerosols has been shortened, suggesting the northward shift of the transboundary air pollution pathway in recent decades.

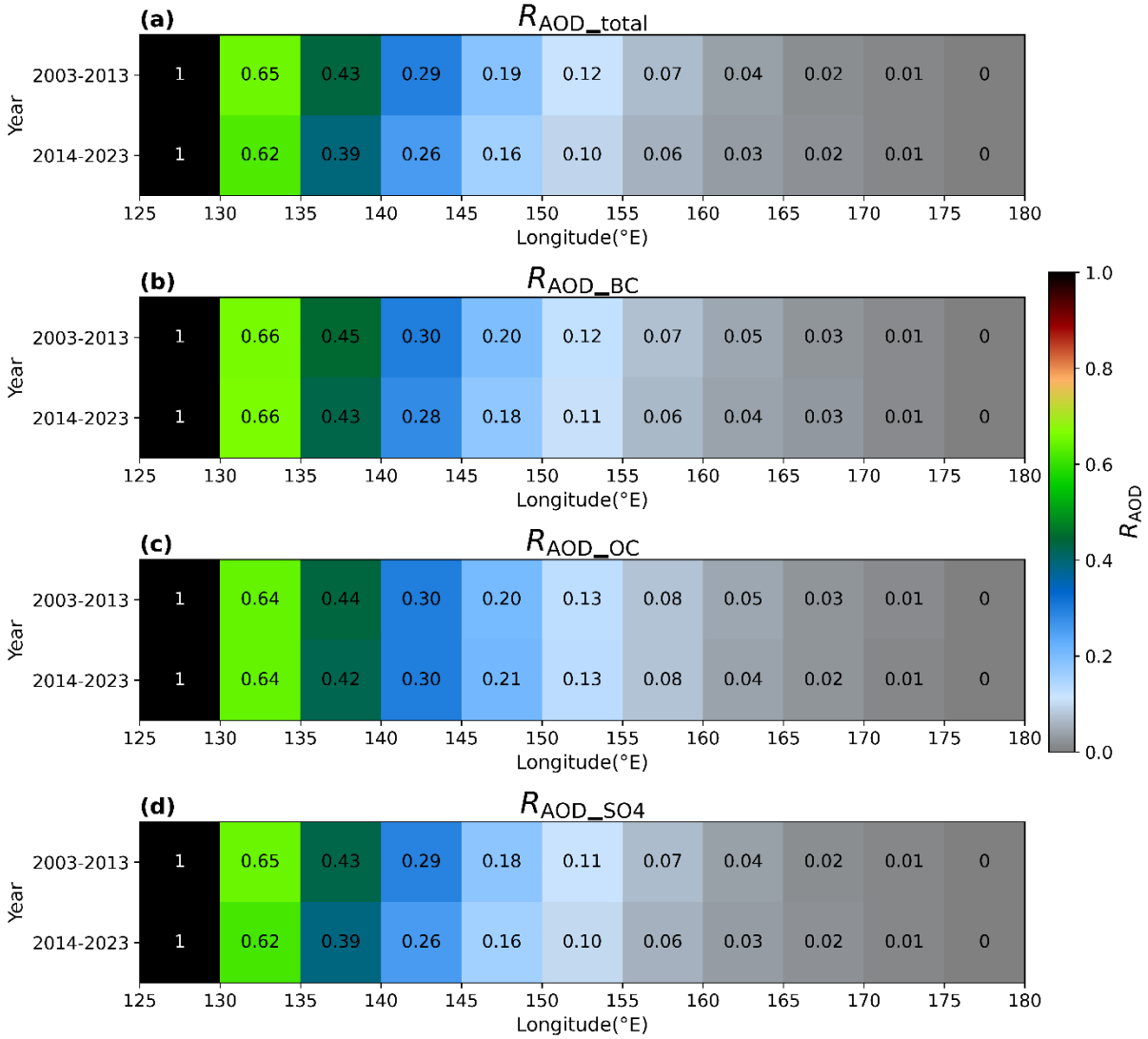

Fig. 7.4 Hovmöller diagram depicting the 10-year longitudinal average of R_{AOD} for total AOD, BC, OC, and SO_4^{2-} which represented by (a) R_{AOD_total}, (b) R_{AOD_BC}, (c) R_{AOD_OC}, (d) $R_{AOD\_SO_4^{2-}}$, respectively. The analysis covers the longitudinal range of 125–180°E using MERRA-2 data during three periods: 2003–2013, and 2014–2023.

7.4. Latitudinal decadal trend of R_{AOD}

The Fig. 7.5 shows an analysis of the linear regression slopes (unit: deg^{-1} per $decade^{-1}$ of the total AOD for R_{AOD} and $R_{AOD\_SO_4^{2-}}$ within the latitude band of 25–30°N (at 0.5° intervals) during two periods (2003–2013 and 2014–2023). Similar to the results, the absolute values of the slopes of R_{AOD} and $R_{AOD\_SO_4^{2-}}$ in the later period (2014–2023) are larger than those in the earlier period (2003–2013). Additionally, the figure reveals a latitudinal trend where the absolute values of the regression slopes decrease with increasing latitude, suggesting that the aerosol transport pathway tends to extend further in higher latitude regions. These results further confirm a northward shift in aerosol transport pathways in recent years.

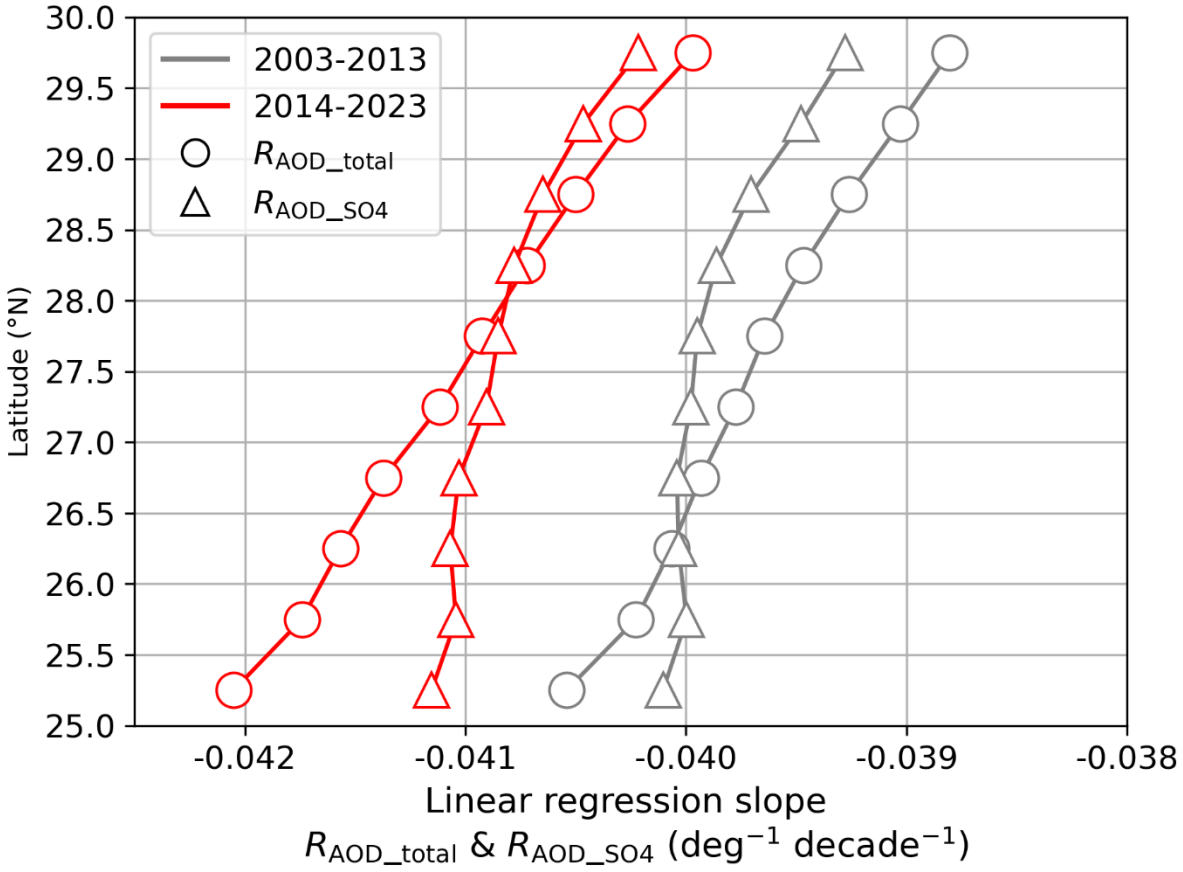

Fig. 7.5 The variation analysis of the slopes (linear regression slopes at Lon125–130°E) of R_{AOD_total} (triangle) and $R_{AOD\_SO_4^{2-}}$ (circle) within the latitude range of 25-30°N (at 0.5° intervals) for the two periods 2003-2013 (gray lines) and 2014-2023 (red lines) (unit: deg^{-1} $decade^{-1}$).

7.5. Decadal wind field analysis

The distribution of wind speed (m/s) and wind direction at 500 hPa over two time periods: 2003–2013 and 2014–2023, based on MERRA-2 reanalysis data (Fig. 7.6). The color scale represents wind speed, with higher wind speeds shown in red, while black arrows indicate the wind direction. The results show that the high wind speed region (depicted in red) has shifted significantly northeast during 2014–2023 compared to 2003–2013. This high wind speed region is likely the position of the subtropical jet stream.

In the earlier period (2003–2013), the core of the subtropical jet was located near 35°N, whereas in the later period (2014–2023), the core of the jet stream shifted northward to approximately 37–40°N. This northward shift in the wind field is consistent with the result of the northward shift of the aerosol transport pathway. The findings suggest that the northward shift of the aerosol transport pathway is likely to be affected by the variation of the wind field, especially due to the northward shift of the subtropical jet stream associated with climate change.

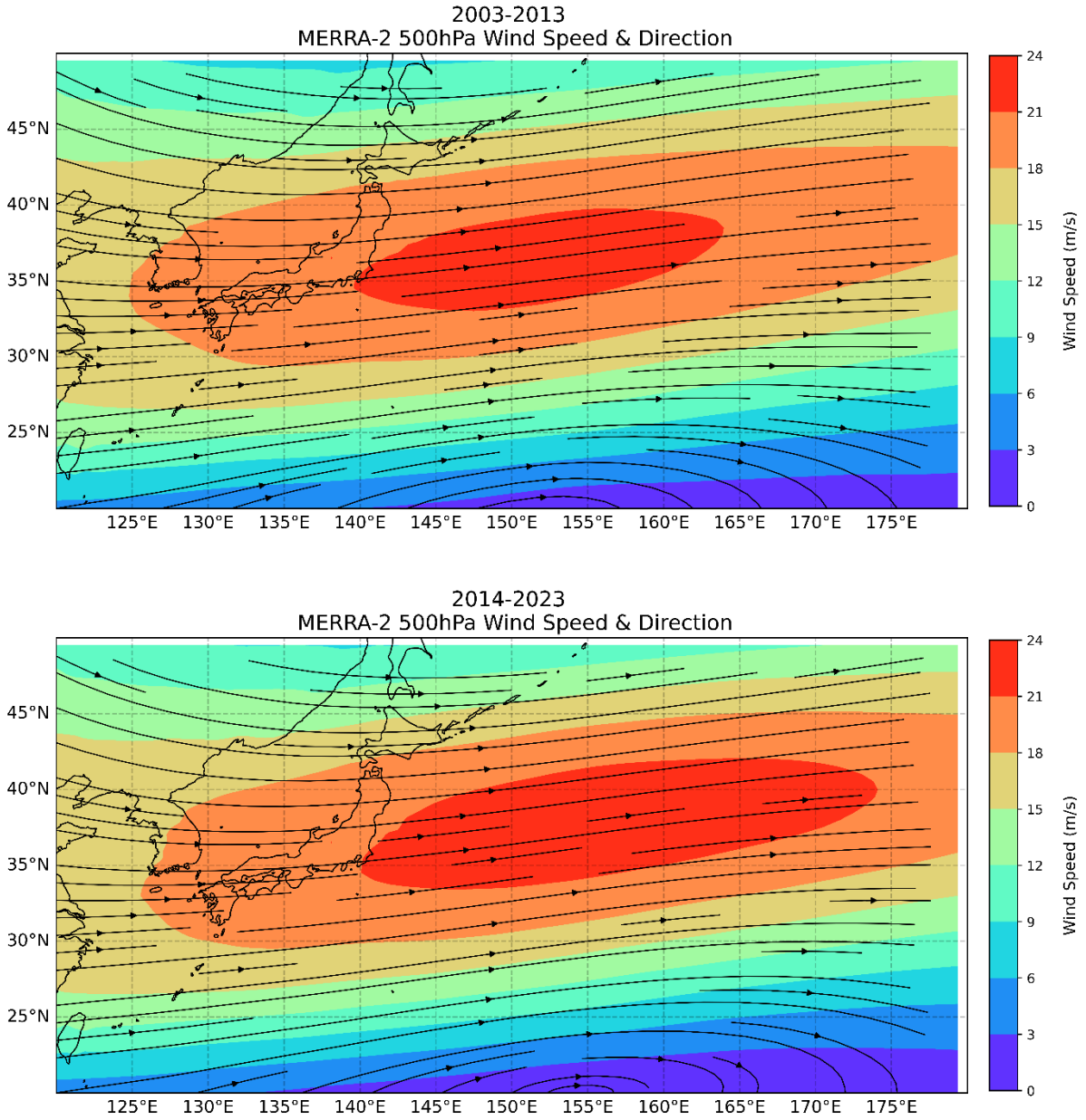

Fig. 7.6 Distribution of wind speed (m/s) and wind direction at 500 hPa from MERRA-2 for the decade periods: 2003-2013 (top figure) and 2014-2023 (bottom figure).

7.6. Summary

We utilized MERRA-2 R_{AOD} for each component, including total AOD, BC, OC, SO_4^{2-} and dust to minimize the influence of aerosol component lifetimes on the eastward transport distance. We also extended the analysis period from 2003 to 2023 to examine variations in transboundary air pollution pathway in recent decades. We found that R_{AOD} for total AOD and SO_4^{2-} exhibited similar longitudinal distribution patterns indicates that SO_4^{2-} aerosols are the primary contributors to R_{AOD} in the downwind regions of China. Moreover, even components like BC and OC have similar trends which contribute relatively less to total AOD. Long-term trends of R_{AOD} for each component showed a similar trend, with the distance over which aerosol concentration decreases by 20% has been shortened over the past decade. These findings provide further evidence that transboundary air pollution pathway have shifted northward in recent decades.

Additionally, the decadal latitudinal analysis of R_{AOD} slopes shows an increased slope in the later decade (2014–2023) compared to the earlier period (2003–2013), suggesting shorter eastward transport distances. Wind field analysis at 500 hPa shows a significant northeastward shift of the high wind speed regions between the two decades. This trend is likely caused by the movement of the subtropical jet stream from approximately 35°N to 37–40°N. These results indicated that the northward shift of the aerosol transport pathway is likely driven by the northward shift of the subtropical jet stream associated with climate change.

Chapter 8. Conclusions

This study analyzed long-term AOD data from the MODIS sensor on Earth observation satellites. We focused on the Pacific region in the downwind area of China, which is a major source of aerosol emissions. To offset the impact of temporal changes in China's emissions, we proposed a new metric (R_{AOD}), which normalized by AOD over coastal China to offset the impact of temporal changes in China's emissions.

Chapter 6 clarifies the detectability of long-term changes in atmospheric transport fields using aerosols. We analyzed the longitudinal trends of R_{AOD} values by using MODIS, MERRA-2, and SPRINTARS datasets. A clear exponential decrease in R_{AOD} values from China towards the Pacific Ocean was observed. Furthermore, the seasonal variations in R_{AOD} were well consistent with the seasonal changes in atmospheric transport fields. These findings indicated that R_{AOD}, has the potential to detect long-term changes in atmospheric transport fields. Additionally, we found that the eastward transport distance of aerosols has been shortened in recent decades, which can be explained by a slight northward shift in the transboundary air pollution pathway in recent years.

Since aerosols contain various components, their composition's lifetime may affect the transport distance. To minimize the influence of aerosol component lifetimes on the eastward transport distance, we analyzed the long-term changes in R_{AOD} for each component in Chapter 7. Investigate not only the main component (SO_4^{2-}), but also other components such as BC (black carbon), OC (organic carbon), and dust. We also extended the analysis period from 2003 to 2023. The longitudinal distribution of anthropogenic R_{AOD} (SO_4^{2-}, BC, OC) is consistent with the total R_{AOD}. Furthermore, annual variations in the slope of

sulfate R_{AOD} are consistent with the total R_{AOD}. BC and OC R_{AOD} showed similar trends, despite a relatively small fraction of total R_{AOD}. Over the past decade, the R_{AOD} for each component has shown a similar trend, with the distance over which aerosol concentration decreases by 20% has been shortened. These results indicate that the SO_4^{2-} is still the primary contributor to AOD in the downwind regions of China. These results provide further evidence that transboundary air pollution pathway has shifted northward in recent decades. Additionally, the decadal latitudinal analysis was consistent with wind field analysis showing a northeastward movement of high wind speed regions and the subtropical jet stream from approximately 35°N to 37–40°N between the periods 2003–2013 and 2014–2023. These results indicated that the northward shift of the aerosol transport pathway is likely driven by the northward shift of the subtropical jet stream associated with climate change.

Overall, potential long-term changes in atmospheric transport fields have been detected, indicating that the transboundary air pollution pathway has shifted northward as climate change progresses. We aspire to utilize R_{AOD} to improve climate model validation and enhance our understanding of future climate change projections. To enhance the detectability of variations in transboundary air pollution pathway associated with climate change, it is essential to utilize longer-term, continuous satellite observation data.

Abbreviations and nomenclature

AOD Aerosol Optical Depth

TOA top-of-atmosphere

σ^{ext} extinction coefficient

$\sigma_{a,a,\lambda}$ aerosol absorption coefficient

$b_{s,a,i,\lambda}$ scattering cross-sections

n_i the number concentration of aerosol of given size (particles cm^{-3})

N_B the number of aerosol sizes

$b_{a,a,i,\lambda}$ effective absorption cross section of a single aerosol particle

$b_{s,a,i,\lambda}$ effective scattering cross section of a single aerosol particle

$n(r)$ size distribution

α^{sca} scattering coefficients

α^{abs} absorption coefficients

Q^{sca} scattering cross-sections

Q^{abs} absorption cross-sections

τ AOD

τ_0 AOD along the eastern coast of China

α attenuation coefficient of AOD

L length of the transboundary air pollution path

$\rho\lambda$ reflectance

L_λ measured spectral radiance

$F_{0,\lambda}$ solar irradiance

$\rho_{0.47}$ reflectance at 0.47 μm

$\sigma_{0.55}$ standard deviation of reflectance at 0.55 μm

$\rho_{atm,\lambda}$ atmospheric path reflectance

T_{λ} total transmittance

$\rho_{surf,\lambda}$ surface reflectance

ϵ squares spectral fitting error

$\rho_{obs,\lambda}$ spectral reflectance of observations

$\rho_{mod,\lambda}$ modeled TOA reflectance

$b_{ext,i}(RH)$ extinction coefficient

∂_z vertical layer thickness

τ^a analyzed AOD in MERRA-2

τ^f forecast AOD in MERRA-2

τ^o observed AOD in MERRA-2

δx^a 3D aerosol concentration increments

$\delta \tau^a$ 2D AOD increments

ρ_{air} air density

q_a aerosol mixing ratio

v horizontal wind components

w vertical wind components

F_E emission fluxes

F_D diffusion fluxes

F_S deposition fluxes

$\mathrm{F_{dust}}$ soil dust emissions

v_{dry} dry deposition velocity

References

Abas, N., Saleem, M.S., Kalair, E., Khan, N., (2019). Cooperative control of regional transboundary air pollutants. Environmental Systems Research, 8, 10. https://doi.org/10.1186/s40068-019-0138-0.

Allan, R.P., Barlow, M., Byrne, M.P., Cherchi, A., Douville, H., Fowler, H.J., Gan, T.Y., Pendergrass, A.G., Rosenfeld, D., Swann, A.L.S., Wilcox, L.J., Zolina, O., (2020). Advances in understanding large-scale responses of the water cycle to climate change. Annals of the New York Academy of Sciences, 1472(1), 49–75. https://doi.org/10.1111/nyas.14337.

Benkovitz, C.M., Scholtz, M.T., Pacyna, J., Tarrason, L., Dignon, J., Voldner, E.C., Spiro, P.A., Logan, J.A., Graedel, T.E., (1996). Global gridded inventories of anthropogenic emissions of sulfur and nitrogen. Journal of Geophysical Research, 101, 29,239–29,253.

Berresheim, H., Wine, P., Davis, D., (1995). Sulfur in the atmosphere. In: Singh, H.B. (Ed.), Composition, Chemistry, and Climate of the Atmosphere. Van Nostrand Reinhold, New York, pp. 251–307.

Bocquet, M., Elbern, H., Eskes, H., Hirtl, M., Žabkar, R., Carmichael, G.R., Flemming, J., Inness, A., Pagowski, M., Pérez Camaño, J.L., Saide, P.E., San Jose, R., Sofiev, M., Vira, J., Baklanov, A., Carnevale, C., Grell, G., Seigneur, C., (2015). Data assimilation in atmospheric chemistry models: Current and future prospects for coupled chemistry meteorology models. Atmospheric Chemistry and Physics, 15, 5325–5358. https://doi.org/10.5194/acp-15-5325-2015.

Bohren, C.F., Huffman, D.R., (2008). Absorption and Scattering of Light by Small Particles. Wiley, Germany, 544 pages. ISBN: 978-3-527-61815-6.

Bosilovich, M.G., Lucchesi, R., Suarez, M., (2016). MERRA-2: File Specification. GMAO Office Note No. 9 (Version 1.1), 73 pp. Available from: http://gmao.gsfc.nasa.gov/pubs/office_notes.

Boucher, O., (2015). Atmospheric Aerosols: Properties and Climate Impacts. Springer, Dordrecht. https://doi.org/10.1007/978-94-017-9649-1.

Buchard, V., da Silva, A.M., Colarco, P.R., Darmenov, A., Randles, C.A., Govindaraju,

R., Torres, O., Campbell, J., Spurr, R., (2015). Using the OMI aerosol index and absorption aerosol optical depth to evaluate the NASA MERRA Aerosol Reanalysis. Atmospheric Chemistry and Physics, 15(10), 5743–5760. https://doi.org/10.5194/acp-15-5743-2015.

Cai, S., Wang, Y., Zhao, B., Wang, S., Chang, X., Hao, J., (2017). The impact of the "Air Pollution Prevention and Control Action Plan" on $PM_{2.5}$ concentrations in Jing-Jin-Ji region during 2012–2020. Science of the Total Environment, 580, 197–209.

Cai, Y., Irie, H., Damiani, A., Itahashi, S., Takemura, T., Khatri, P., (2024). Detectability of the potential climate change effect on transboundary air pollution pathways in the downwind area of China. Science of the Total Environment, 939, 173490. https://doi.org/10.1016/j.scitotenv.2024.173490.

Cao, Z., Luan, K., Zhou, P., Shen, W., Wang, Z., Zhu, W., Qiu, Z., Wang, J., (2023). Evaluation and comparison of multi-satellite aerosol optical depth products over East Asia Ocean. Toxics, 11(10), 813. https://doi.org/10.3390/toxics11100813.

Center for Global Environmental Research, National Institute for Environmental Studies, (n.d.). About METEX. Developed by NIES. Retrieved April 22, 2024, from https://db.cger.nies.go.jp/ged/metex/en/about.html.

Chakraborty, S., Guan, B., Waliser, D.E., da Silva, A.M., Uluatam, S., Hess, P., (2021). Extending the atmospheric river concept to aerosols: Climate and air quality impacts. Geophysical Research Letters, 48, e2020GL091827. https://doi.org/10.1029/2020GL091827.

Che, H., Gui, K., Xia, X., Wang, Y., Holben, B.N., Goloub, P., Cuevas-Agulló, E., Wang, H., Zheng, Y., Zhao, H., Zhang, X., (2019). Large contribution of meteorological factors to inter-decadal changes in regional aerosol optical depth. Atmospheric Chemistry and Physics, 19, 10497–10523. https://doi.org/10.5194/acp-19-10497-2019.

Che, H., Stier, P., Watson-Parris, D., Gordon, H., Deaconu, L., (2022). Source attribution of cloud condensation nuclei and their impact on stratocumulus clouds and radiation in the south-eastern Atlantic. Atmospheric Chemistry and Physics, 22, 10789–10807. https://doi.org/10.5194/acp-22-10789-2022.

Chin, M., Ginoux, P., Kinne, S., Torres, O., Holben, B.N., Duncan, B.N., Martin, R.V., Logan, J.A., Higurashi, A., Nakajima, T., (2002). Tropospheric aerosol optical thickness from the GOCART model and comparisons with satellite and sun photometer measurements. Journal of the Atmospheric Sciences, 59, 461–483.

https://doi.org/10.1175/1520-0469(2002)059<0461:TAOTFT>2.0.CO;2.

Cross, E.S., Onasch, T.B., Ahern, A., Wrobel, W., Slowik, J.G., Olfert, J., Lack, D.A., Massoli, P., Cappa, C.D., Schwarz, J.P., Spackman, J.R., Fahey, D.W., Sedlacek, A., Trimborn, A., Jayne, J.T., Freedman, A., Williams, L.R., Ng, N.L., Mazzoleni, C., Dubey, M., Brem, B., Kok, G., Subramanian, R., Freitag, S., Clarke, A., Thornhill, D., Marr, L.C., Kolb, C.E., Worsnop, D.R., Davidovits, P., (2010). Soot particle studies instrument inter-comparison project overview. Aerosol Science and Technology, 44, 592–611. https://doi.org/10.1080/02786826.2010.482113.

Damiani, A., Cordero, R.R., Llanillo, P.J., Feron, S., Boisier, J.P., Garreaud, R., Rondanelli, R., Irie, H., Watanabe, S., (2020). Connection between Antarctic ozone and climate: Interannual precipitation changes in the southern hemisphere. Atmosphere, 11, 579. https://doi.org/10.3390/atmos11060579.

Dee, D.P., da Silva, A.M., (1999). Maximum-likelihood estimation of forecast and observation error covariance parameters. Part I: Methodology. Monthly Weather Review, 127, 1811–1834. https://doi.org/10.1175/1520-0493(1999)127<1822:MLEOFA>2.0.CO;2.

Diehl, T., Heil, A., Chin, M., Pan, X., Streets, D., Schultz, M., Kinne, S., (2012). Anthropogenic, biomass burning, and volcanic emissions of black carbon, organic carbon, and SO_2 from 1980 to 2010 for hindcast model experiments. Atmospheric Chemistry and Physics Discussions, 12(9), 24895–24954. https://doi.org/10.5194/acpd-12-24895-2012.

Douville, H., Voldoire, A., Geoffroy, O., (2015). The recent global warming hiatus: What is the role of Pacific variability? Geophysical Research Letters, 42(3), 880–888. https://doi.org/10.1002/2014gl062775.

Epstein, P.R., Buonocore, J.J., Eckerle, K., Hendryx, M., Stout III, B.M., Heinberg, R., Clapp, R.W., May, B., Reinhart, N.L., Ahern, M.M., Doshi, S.K., Glustrom, L., (2011). Full cost accounting for the life cycle of coal. Annals of the New York Academy of Sciences, 1219, 73–98. https://doi.org/10.1111/j.1749-6632.2010.05890.x. Erratum in: Annals of the New York Academy of Sciences, 1225, 201.

Erickson, D.J., Merrill, J.T., Duce, R.A., (1986). Seasonal estimates of global atmospheric sea-salt distribution. Journal of Geophysical Research, 91, 1067–1072.

European Commission, (2011). European Commission/Joint Research Centre (JRC)/Netherlands Environmental Assessment Agency (PBL): Emission Database for Global Atmospheric Research (EDGAR), release version 4.2. Available at:

http://edgar.jrc.ec.europa.eu.

Gan, R., Liu, Q., Huang, G., Hu, K., Li, X., (2023). Greenhouse warming and internal variability increase extreme and central Pacific El Niño frequency since 1980. Nature Communications, 14, 394. https://doi.org/10.1038/s41467-023-36053-7.

Gao, B., Yang, P., Han, W., Li, R., Wiscombe, W., (2002). An algorithm using visible and 1.38-μm channels to retrieve cirrus cloud reflectances from aircraft and satellite data. IEEE Transactions on Geoscience and Remote Sensing, 40, 1659–1668. https://doi.org/10.1109/TGRS.2002.802454.

Gao, Y., Zhuang, B., Wang, T., Chen, H., Li, S., Wei, W., Lin, H., Li, M., (2022). Climatic–Environmental Effects of Aerosols and Their Sensitivity to Aerosol Mixing States in East Asia in Winter. Remote Sensing, 14(15), 3539. https://doi.org/10.3390/rs14153539.

Gardner, D.K., (2018). Environmental pollution in China: What everyone needs to know. Oxford University Press, 304 pages. ISBN: 9780190696122.

Gelaro, R., McCarty, W., Suárez, M., Todling, R., Molod, A., Takacs, L., Randles, C., Darmenov, A., Bosilovich, M., Reichle, R., Wargan, K., Coy, L., Cullather, R., Draper, C., Akella, S., Buchard, V., Conaty, A., da Silva, A., Gu, W., Kim, G., Koster, R., Lucchesi, R., Merkova, D., Nielsen, J., Partyka, G., Pawson, S., Putman, W., Rienecker, M., Schubert, S., Sienkiewicz, M., Zhao, B., (2017). The Modern-Era Retrospective Analysis for Research and Applications, Version 2 (MERRA-2). Journal of Climate, 30(14), 5419–5454. https://journals.ametsoc.org/view/journals/clim/30/14/jcli-d-16-0758.1.

Gordon, H., Sengupta, K., Rap, A., Duplissy, J., Frege, C., Williamson, C., Almeida, J., (2016). Reduced anthropogenic aerosol radiative forcing caused by biogenic new particle formation. Proceedings of the National Academy of Sciences, 113(43), 12053–12058. https://doi.org/10.1073/pnas.1602360113.

Goto, D., Nakajima, T., Takemura, T., Sudo, K., (2011). A study of uncertainties in the sulfate distribution and its radiative forcing associated with sulfur chemistry in a global aerosol model. Atmospheric Chemistry and Physics, 11, 10889–10910.

Gu, X., Bao, F., Cheng, T., Chen, H., Wang, Y., Guo, H., (2018). The impacts of regional transport and meteorological factors on aerosol optical depth over Beijing, 1980–2014. Scientific Reports, 8, 5113. https://doi.org/10.1038/s41598-018-22803-x.

Gu, Y., Fang, T., & Yim, S. H. L. (2024). Source emission contributions to particulate

matter and ozone, and their health impacts in Southeast Asia. Environment international, 186, 108578. https://doi.org/10.1016/j.envint.2024.108578.

Guannel, G., Arkema, K., Ruggiero, P., Verutes, G., (2016). The power of three: Coral reefs, seagrasses and mangroves protect coastal regions and increase their resilience. PLoS ONE, 11(7), e0158094. https://doi.org/10.1371/journal.pone.0158094.

Hao, H., Wang, K., Zhao, C., Wu, G., Li, J., (2024). Visibility-derived aerosol optical depth over global land from 1959 to 2021. Earth System Science Data, 16, 3233–3260. https://doi.org/10.5194/essd-16-3233-2024.

Hashimoto, M., Nakajima, T., Dubovik, O., Campanelli, M., Che, H., Khatri, P., Takamura, T., Pandithurai, G., (2012). Development of a new data-processing method for SKYNET sky radiometer observations. Atmospheric Measurement Techniques, 5, 2723–2737. https://doi.org/10.5194/amt-5-2723-2012.

Heald, C.L., Ridley, D.A., Kroll, J.H., Barrett, S.R.H., Cady-Pereira, K.E., Alvarado, M.J., Holmes, C.D., (2014). Contrasting the direct radiative effect and direct radiative forcing of aerosols. Atmospheric Chemistry and Physics, 14, 5513–5527. https://doi.org/10.5194/acp-14-5513-2014.

Heidinger, A.K., Cao, C., Sullivan, J.T., (2002). Using Moderate Resolution Imaging Spectrometer (MODIS) to calibrate advanced very high resolution radiometer reflectance channels. Journal of Geophysical Research, 107, 4702. https://doi.org/10.1029/2001JD002035.

Holben, B., and Coauthors, (1998). AERONET—A federated instrument network and data archive for aerosol characterization. Remote Sensing of Environment, 66, 1–16. https://doi.org/10.1016/S0034-4257(98)00031-5.

Holton, J.R., (2004). An Introduction to Dynamic Meteorology. 4th Edition, Volume 88. Elsevier Academic Press, April 26, 2004. eBook ISBN: 9780080470214.

Hosono, T., Nakashima, S., Tanoue, M., et al., (2022). Monsoon climate controls metal loading in global hotspot region of transboundary air pollution. Scientific Reports, 12, 11096. https://doi.org/10.1038/s41598-022-15066-0.

Hsu, N.C., Tsay, S.-C., King, M.D., Herman, J.R., (2004). Aerosol properties over bright-reflecting source regions. IEEE Transactions on Geoscience and Remote Sensing, 42(3), 557–569. https://doi.org/10.1109/TGRS.2004.824067.

Huang, X., Ding, A., Wang, Z., et al., (2020). Amplified transboundary transport of haze

by aerosol–boundary layer interaction in China. Nature Geoscience, 13, 428–434. https://doi.org/10.1038/s41561-020-0583-4.

Ikeda, K., Yamaji, K., Kanaya, Y., Taketani, F., Pan, X., Komazaki, Y., Kurokawa, J., Ohara, T., (2015). Source region attribution of $PM_{2.5}$ mass concentrations over Japan. Geochemical Journal, 49(2), 185–194. https://doi.org/10.2343/geochemj.2.0344.

Intergovernmental Panel on Climate Change (IPCC), (2021a). Climate Change 2021: The Physical Science Basis. Contribution of Working Group I to the Sixth Assessment Report of the Intergovernmental Panel on Climate Change. [Online]. Available at: https://www.ipcc.ch/report/ar6/wg1/.

Intergovernmental Panel on Climate Change (IPCC), (2021b). Climate Change 2021: Mitigation of Climate Change. Contribution of Working Group III to the Sixth Assessment Report of the Intergovernmental Panel on Climate Change. [Online]. Available at: https://www.ipcc.ch/report/ar6/wg3/.

Itahashi, S., Sakurai, T., Shimadera, H., Araki, S., Hayami, H., (2021). Long-term trends of satellite-based fine-mode aerosol optical depth over the Seto Inland Sea, Japan, over two decades (2001–2020). Environmental Research Letters, 16(10), 105009. https://doi.org/10.1088/1748-9326/ac03db

Jin, S., Ma, Y., Huang, Z., Huang, J., Gong, W., Liu, B., Wang, W., Fan, R., Li, H., (2023). A comprehensive reappraisal of long-term aerosol characteristics, trends, and variability in Asia. Atmospheric Chemistry and Physics, 23, 8187–8210. https://doi.org/10.5194/acp-23-8187-2023.

Jion, M.M.M.F., Jannat, J.N., Mia, M.Y., Ali, M.A., Islam, M.S., Ibrahim, S.M., Pal, S.C., Islam, A., Sarker, A., Malafaia, G., Bilal, M., Islam, A.R.M.T., (2023). A critical review and prospect of NO_2 and SO_2 pollution over Asia: Hotspots, trends, and sources. Science of the Total Environment, 876, 162851. https://doi.org/10.1016/j.scitotenv.2023.162851.

Jonidi Jafari, A., Charkhloo, E., Pasalari, H., (2021). Urban air pollution control policies and strategies: A systematic review. Journal of Environmental Health Science & Engineering, 19(2), 1911–1940. https://doi.org/10.1007/s40201-021-00744-4.

Justice, C.O., Townshend, J.R.G., Vermote, E.F., Masuoka, E., Wolfe, R.E., Saleous, N., Roy, D.P., Morisette, J.T., (2002). An overview of MODIS Land data processing and product status. Remote Sensing of Environment, 83(1–2), 3–15. https://doi.org/10.1016/S0034-4257(02)00084-6.

Jyethi, D., (2016). Air Quality: Global and Regional Emissions of Particulate Matter, SO_x, and NO_x. In: Global and Regional Emissions. Springer, pp. 19–42. https://doi.org/10.1007/978-981-10-1201-3_2.

Kahn, R.A., Gaitley, B.J., Martonchik, J.V., Diner, D.J., Crean, K.A., Holben, B., (2005). Multiangle Imaging Spectroradiometer (MISR) global aerosol optical depth validation based on 2 years of coincident Aerosol Robotic Network (AERONET) observations. Journal of Geophysical Research, 110, D10S04. https://doi.org/10.1029/2004JD004706.

Kaufman, Y.J., Tanré, D., Remer, L.A., Vermote, E.F., Chu, A., Holben, B.N., (1997). Operational remote sensing of tropospheric aerosol over land from EOS moderate resolution imaging spectroradiometer. Journal of Geophysical Research: Atmospheres, 102(D14), 17051–17067. https://doi.org/10.1029/96JD03988.

Keeley, J., Yisheng, Z., (Eds.), (2012). Green China: Chinese insights on environment and development. IIED. ISBN: 9781843698166. Available at: https://www.iied.org/17509iied.

Kleidman, R.G., Smirnov, A., Levy, R.C., Mattoo, S., Tanré, D., (2012). Evaluation and wind speed dependence of MODIS aerosol retrievals over open ocean. IEEE Transactions on Geoscience and Remote Sensing, 50, 429–435. https://doi.org/10.1109/TGRS.2011.2162073.

Kondragunta, S., Zhu, A., (2024). Methane emissions from wildfires: Trends and anomalies. EGU General Assembly 2024, Vienna, Austria, 14–19 Apr 2024, EGU24-20492. https://doi.org/10.5194/egusphere-egu24-20492.

Kong, L., Tang, X., Zhu, J., Wang, Z., Li, J., Wu, H., Wu, Q., Chen, H., Zhu, L., Wang, W., Liu, B., Wang, Q., Chen, D., Pan, Y., Song, T., Li, F., Zheng, H., Jia, G., Lu, M., Wu, L., Carmichael, G.R., (2021). A 6-year-long (2013–2018) high-resolution air quality reanalysis dataset in China based on the assimilation of surface observations from CNEMC. Earth System Science Data, 13, 529–570. https://doi.org/10.5194/essd-13-529-2021.

Kushta, J., Kallos, G., Astitha, M., Solomos, S., Spyrou, C., Mitsakou, C., Lelieveld, J., (2014). Impact of natural aerosols on atmospheric radiation and consequent feedbacks with the meteorological and photochemical state of the atmosphere. Journal of Geophysical Research: Atmospheres, 119(3), 1463–1491. https://doi.org/10.1002/2013JD020714.

Lee, H.J., Jo, Y.J., Kim, S., Kim, D., Kim, J.M., Choi, D., Jo, H.Y., Bak, J., Park, S.Y.,

Jeon, W., Kim, C.H., (2022). Transboundary aerosol transport process and its impact on aerosol-radiation-cloud feedbacks in springtime over Northeast Asia. Scientific Reports, 12, 4870. https://doi.org/10.1038/s41598-022-08854-1.

Lee, K., Chandra, I., Seto, T., Inomata, Y., Hayashi, M., Takami, A., Yoshino, A., Otani, Y., (2019). Aerial observation of atmospheric nanoparticles on Fukue Island, Japan. Aerosol and Air Quality Research, 19, 981–994. https://doi.org/10.4209/aaqr.2018.03.0077.

Leung, G.R., van den Heever, S.C., (2023). Aerosol breezes drive cloud and precipitation increases. Nature Communications, 14(1), 1–8. https://doi.org/10.1038/s41467-023-37722-3.

Levy, R., Hsu, C., (2015). MODIS Atmosphere L2 Aerosol Product. NASA MODIS Adaptive Processing System, Goddard Space Flight Center, USA. Available at: http://dx.doi.org/10.5067/MODIS/MOD04_L2.006.

Levy, R.C., Mattoo, S., Munchak, L.A., Remer, L.A., Sayer, A.M., Patadia, F., Hsu, N.C., (2013). The Collection 6 MODIS aerosol products over land and ocean. Atmospheric Measurement Techniques, 6, 2989–3034. https://doi.org/10.5194/amt-6-2989-2013.

Levy, R.C., Remer, L.A., Dubovik, O., (2007). Global aerosol optical properties and application to Moderate Resolution Imaging Spectroradiometer aerosol retrieval over land. Journal of Geophysical Research - Atmospheres, 112, D13210. https://doi.org/10.1029/2006JD007815.

Levy, R.C., Remer, L.A., Tanré, D., Mattoo, S., Kaufman, Y.J., (2009). Algorithm for remote sensing of tropospheric aerosol over dark targets from MODIS: Collections 005 and 051: Revision 2. MODIS Algorithm Theoretical Basis Document.

Li, C., Chen, Z., Hu, Y., Cai, C., Zuo, X., Shang, G., Lin, H., (2023). The energy conservation and emission reduction co-benefits of China's emission trading system. Scientific Reports, 13, 13758. https://doi.org/10.1038/s41598-023-40811-4.

Li, J., Carlson, B.E., Yung, Y.L., Lv, D., Hansen, J., Penner, J.E., Liao, H., Ramaswamy, V., Kahn, R.A., Zhang, P., Dubovik, O., Ding, A., Lacis, A.A., Zhang, L., Dong, Y., (2022). Scattering and absorbing aerosols in the climate system. Nature Reviews Earth & Environment, 3, 363–379. https://doi.org/10.1038/s43017-022-00296-7.

Li, Z., Lau, W.K.-M., Ramanathan, V., Wu, G., Ding, Y., Manoj, M.G., Liu, J., Qian, Y.,

Li, J., Zhou, T., Fan, J., Rosenfeld, D., Ming, Y., Wang, Y., Huang, J., Wang, B., Xu, X., Lee, S.-S., Cribb, M., Zhang, F., Yang, X., Zhao, C., Takemura, T., Wang, K., Xia, X., Yin, Y., Zhang, H., Guo, J., Zhai, P.M., Sugimoto, N., Babu, S.S., Brasseur, G.P., (2016). Aerosol and monsoon climate interactions over Asia. Reviews of Geophysics, 54(4), 866–929. https://doi.org/10.1002/2015RG000500.

Liu, Y., Zhou, Y., Lu, J., (2020). Exploring the relationship between air pollution and meteorological conditions in China under environmental governance. Scientific Reports, 10, 14518. https://doi.org/10.1038/s41598-020-71338-7.

Lohmann, U., (2017). Anthropogenic Aerosol Influences on Mixed-Phase Clouds. Current Climate Change Reports, 3, 32–44. https://doi.org/10.1007/s40641-017-0059-9.

Lorenz, E.N., (1955). Available potential energy and the maintenance of the general circulation. Tellus, 7(2), 157–167. https://doi.org/10.3402/tellusa.v7i2.8796.

Louis, J., (1979). A parametric model of vertical eddy fluxes in the atmosphere. Boundary-Layer Meteorology, 17, 187–202.

Lu, Z., Zhang, Q., Streets, D.G., (2011). Sulfur dioxide and primary carbonaceous aerosol emissions in China and India, 1996–2010. Atmospheric Chemistry and Physics, 11, 9839–9864. https://doi.org/10.5194/acp-11-9839-2011.

Mamouei, M., Budidha, K., Baishya, N., et al., (2021). An empirical investigation of deviations from the Beer–Lambert law in optical estimation of lactate. Scientific Reports, 11, 13734. https://doi.org/10.1038/s41598-021-92850-4.

Manney, G.L., Hegglin, M.I., Daffer, W.H., Schwartz, M.J., Santee, M.L., Pawson, S., (2014). Climatology of upper tropospheric/lower stratospheric (UTLS) jets and tropopauses in MERRA. Journal of Climate, 27, 3248–3271. https://doi.org/10.1175/JCLI-D-13-00243.1.

Martins, J.V., Tanré, D., Remer, L., Kaufman, Y., Mattoo, S., Levy, R., (2002). MODIS Cloud screening for remote sensing of aerosols over oceans using spatial variability. Geophysical Research Letters, 29, 8009. https://doi.org/10.1029/2001GL013252.

Matthews, E., (1983). Global vegetation and land use: New high-resolution data bases for climate studies. Journal of Climate and Applied Meteorology, 22, 474–487.

McCarty, W., Coy, L., Gelaro, R., Huang, A., Merkova, D., Smith, E.B., Sienkiewicz, M., Wargan, K., (2016). MERRA-2 input observations: Summary and initial assessment. Technical Report Series on Global Modeling and Data Assimilation,

Vol. 46, NASA Tech. Rep. NASA/TM–2016–104606, 61 pp.

McGuffie, K., Henderson-Sellers, A., (2001). Forty years of numerical climate modeling. International Journal of Climatology, 21, 1067–1109. https://doi.org/10.1002/joc.632.

Momoi, M., Kudo, R., Aoki, K., Mori, T., Miura, K., Okamoto, H., Irie, H., Shoji, Y., Uchiyama, A., Ijima, O., Takano, M., Nakajima, T., (2020). Development of on-site self-calibration and retrieval methods for sky-radiometer observations of precipitable water vapor. Atmospheric Measurement Techniques, 13, 2635–2658. https://doi.org/10.5194/amt-13-2635-2020.

Mori, M., Kosaka, Y., Taguchi, B., et al., (2024). Northern Hemisphere winter atmospheric teleconnections are intensified by extratropical ocean-atmosphere coupling. Communications Earth & Environment, 5, 124. https://doi.org/10.1038/s43247-024-01282-1.

Mushtaq, Z., Sharma, M., Bangotra, P., et al., (2022). Atmospheric aerosols: Some highlights and highlighters, past to recent years. Aerosol Science and Engineering, 6, 135–145. https://doi.org/10.1007/s41810-022-00133-w.

Myhre, G., Myhre, C.E.L., Samset, B.H., Storelvmo, T., (2013). Aerosols and their relation to global climate and climate sensitivity. Nature Education Knowledge, 4(5), 7.

Nakajima, T., Tonna, G., Rao, R., Kaufman, Y., Holben, B., (1996). Use of sky brightness measurements from ground for remote sensing of particulate polydispersions. Applied Optics, 35, 2672–2686. https://doi.org/10.1364/AO.35.002672.

Nakajima, T., Yoon, S.C., Ramanathan, V., Shi, G.Y., Takemura, T., Higurashi, A., Takamura, T., Aoki, K., Sohn, B.J., Kim, S.W., Tsuruta, H., Sugimoto, N., Shimizu, A., Tanimoto, H., Sawa, Y., Lin, N.H., Lee, C.T., Goto, D., Schutgens, N., (2007). Overview of the atmospheric brown cloud east Asia regional experiment 2005 and a study of the aerosol direct radiative forcing in east Asia. Journal of Geophysical Research, 112, D24S91. https://doi.org/10.1029/2007JD009009.

Narita, D., Oanh, N.T.K., Sato, K., Huo, M., Permadi, D.A., Chi, N.N.H., Ratanajaratroj, T., Pawarmart, I., (2019). Pollution characteristics and policy actions on fine particulate matter in a growing Asian economy: The case of Bangkok Metropolitan Region. Atmosphere, 10(5), 227. https://doi.org/10.3390/atmos10050227.

Nguyen, G.T.H., Shimadera, H., Sekiguchi, A., Matsuo, T., Kondo, A., (2019). Investigation of aerosol direct effects on meteorology and air quality in East Asia by using an online coupled modeling system. Atmospheric Environment, 207, 182–196. https://doi.org/10.1016/j.atmosenv.2019.03.017.

Nica, A., Popescu, A., Ibanescu, D.C., (2019). Human influence on the climate system. Current Trends in Natural Sciences, 8(15), 209–215. ISSN: 2284-953X (Online), 2284-9521 (CD-ROM), ISSN-L: 2284-9521.

Oanh, N.T.K., Permadi, D.A., Phuc, N.H., Zhuang, Y., (2012). Air quality status and management practices in Asian developing countries. In: Integrated Air Quality Management (1st ed., pp. 62). CRC Press. https://doi.org/10.1201/b12235.

Pandis, S.N., Paulson, S.E., Seinfeld, J.H., Flagan, R.C., (1991). Aerosol formation in the photooxidation of isoprene and β-pinene. Atmospheric Environment, Series A, 25, 997–1008.

Park, J., Jung, J., Choi, Y., Lim, H., Kim, M.-S., Lee, K., Lee, Y., Kim, J., (2023). Satellite-based, top-down approach for the adjustment of aerosol precursor emissions over East Asia: The Tropospheric Monitoring Instrument (TROPOMI) NO_2 product and the Geostationary Environment Monitoring Spectrometer (GEMS) aerosol optical depth (AOD) data fusion product and its proxy. Atmospheric Measurement Techniques, 16, 3039–3058. https://doi.org/10.5194/amt-16-3039-2023.

Patz, J.A., Grabow, M.L., Limaye, V.S., (2014). When it rains, it pours: Future climate extremes and health. Annals of Global Health, 80(4), 332–344. https://doi.org/10.1016/j.aogh.2014.09.007.

Pereira, P., Inácio, M., Karnauskaitė, D., Bogdzevič, K., Gomes, E., Kalinauskas, M., Barcelo, D., (2021). Nature-based solutions impact on urban environment chemistry: Air, soil, and water. In: Ferreira, C.S.S., Kalantari, Z., Hartmann, T., Pereira, P. (eds), Nature-Based Solutions for Flood Mitigation. The Handbook of Environmental Chemistry, vol. 107. Springer, Cham. https://doi.org/10.1007/698_2021_760.

Ramanathan, V., Carmichael, G., (2008). Global and regional climate changes due to black carbon. Nature Geoscience, 1, 221–227. https://doi.org/10.1038/ngeo156.

Randerson, J.T., van der Werf, G.R., Collatz, G.J., Giglio, L., Still, C.J., Kasibhatla, P., Miller, J.B., White, J.W.C., DeFries, R.S., Kasischke, E.S., (2005). Fire emissions from C_3 and C_4 vegetation and their influence on interannual variability of

atmospheric CO_2 and $\delta^{13}CO_2$. Global Biogeochemical Cycles, 19, GB2019. https://doi.org/10.1029/2004GB002366.

Randles, C.A., da Silva, A.M., Buchard, V., Colarco, P.R., Darmenov, A., Aquila, V., Bian, H., Nowottnick, E.P., Pan, X., Smirnov, A., Yu, H., Govindaraju, R., (2016). The MERRA-2 aerosol assimilation. NASA Technical Report Series on Global Modeling and Data Assimilation, NASA/TM-2016-104606, Vol. 45, 143 pp.

Randles, C.A., da Silva, A.M., Buchard, V., Colarco, P.R., Darmenov, A., Aquila, V., Bian, H., Nowottnick, E.P., Pan, X., Smirnov, A., Yu, H., Govindaraju, R., (2017). The MERRA-2 aerosol assimilation. Journal of Climate, 30(17), 6823–6850. https://doi.org/10.1175/JCLI-D-16-0609.1.

Ratnam, M.V., Prasad, P., Raj, S.T.A., Raman, M.R., Basha, G., (2021). Changing patterns in aerosol vertical distribution over South and East Asia. Scientific Reports, 11, 308. https://doi.org/10.1038/s41598-020-79361-4.

Remer, L.A., Kaufman, Y.J., Tanré, D., Mattoo, S., Chu, D.A., Martins, J.V., Li, R.R., Ichoku, C., Levy, R.C., Kleidman, R.G., Eck, T.F., Vermote, E., Holben, B.N., (2005). The MODIS aerosol algorithm, products, and validation. Journal of Atmospheric Sciences, 62, 947–973. https://doi.org/10.1175/JAS3385.1.

Remer, L.A., Kleidman, R.G., Levy, R.C., Kaufman, Y.J., Tanré, D., Mattoo, S., Martins, J.V., Ichoku, C., Koren, I., Yu, H., Holben, B.N., (2008). Global aerosol climatology from the MODIS satellite sensors. Journal of Geophysical Research - Atmospheres, 113, D14S07. https://doi.org/10.1029/2007JD009661.

Remer, L.A., Mattoo, S., Levy, R.C., Heidinger, A., Pierce, R.B., Chin, M., (2012). Retrieving aerosol in a cloudy environment: aerosol product availability as a function of spatial resolution. Atmospheric Measurement Techniques, 5, 1823–1840. https://doi.org/10.5194/amt-5-1823-2012.

Rosenfeld, D., Sherwood, S., Wood, R., Donner, L., (2014). Climate effects of aerosol-cloud interactions. Science, 343(6169), 379–380. https://doi.org/10.1126/science.1247490.

Ryu, Y.H., Min, S.K., (2024). Anthropogenic warming degrades spring air quality in Northeast Asia by enhancing atmospheric stability and transboundary transport. npj Climate and Atmospheric Science, 7, 50. https://doi.org/10.1038/s41612-024-00603-7.

Samset, B.H., Sand, M., Smith, C.J., Bauer, S.E., Forster, P.M., Fuglestvedt, J.S.,

Osprey, S., Schleussner, C.-F., (2018). Climate impacts from a removal of anthropogenic aerosol emissions. Geophysical Research Letters, 45, 1020–1029. https://doi.org/10.1002/2017GL076079.

Santer, B. D., Thorne, P. W., Haimberger, L., Taylor, K. E., Wigley, T. M. L., Lanzante, J. R., Solomon, S., Free, M., Gleckler, P. J., Jones, P. D., Karl, T. R., Klein, S. A., Mears, C., Nychka, D., Schmidt, G. A., Sherwood, S. C., & Wentz, F. J. (2008). Consistency of modelled and observed temperature trends in the tropical troposphere. International Journal of Climatology, 28(13), 1703–1722. https://doi.org/10.1002/joc.1756.

Satheesh, S., Krishnamoorthy, K., (2005). Radiative effects of natural aerosols: A review. Atmospheric Environment, 39(11), 2089–2110. https://doi.org/10.1016/j.atmosenv.2004.12.029.

Schumacher, V., Setzer, A., Martins, V., Victorino, P., (2024). Evaluation and comparison of MODIS and MISR aerosol products with ground-based monitoring stations in the Amazon Basin. Atmospheric Environment, 331, 120597. https://doi.org/10.1016/j.atmosenv.2024.120597.

Seinfeld, J.H., Pandis, S.N., (2016). Atmospheric Chemistry and Physics: From Air Pollution to Climate Change, 3rd ed. John Wiley & Sons. ISBN: 978-1-118-94740-1.

Shaw, T., Baldwin, M., Barnes, E., et al., (2016). Storm track processes and the opposing influences of climate change. Nature Geoscience, 9, 656–664. https://doi.org/10.1038/ngeo2783.

Shi, Q., Zheng, B., Zheng, Y., et al., (2022). Co-benefits of CO_2 emission reduction from China's clean air actions between 2013–2020. Nature Communications, 13, 5061. https://doi.org/10.1038/s41467-022-32656-8.

Shindell, D.T., (2014). Inhomogeneous forcing and transient climate sensitivity. Nature Climate Change, 4(4), 274–277. https://doi.org/10.1038/Nclimate2136.

Sogacheva, L., de Leeuw, G., Rodriguez, E., Kolmonen, P., Georgoulias, A.K., Alexandri, G., Kourtidis, K., Proestakis, E., Marinou, E., Amiridis, V., Xue, Y., van der A, R.J., (2018). Spatial and seasonal variations of aerosols over China from two decades of multi-satellite observations – Part 1: ATSR (1995–2011) and MODIS C6.1 (2000–2017). Atmospheric Chemistry and Physics, 18, 11389–11407. https://doi.org/10.5194/acp-18-11389-2018.

Spiro, P.A., Jacob, D.J., Logan, J.A., (1992). Global inventory of sulfur emissions with 1×1 resolution. Journal of Geophysical Research, 97, 6023–6036.

Subba, T., Pathak, B., Gogoi, M.M., Ajay, P., Dahutia, P., Chakraborty, A., Bhuyan, P.K., (2023). Observations on the decadal variability of aerosol in eastern Himalayan foothills: Evidence of an anthropologically induced positive shift. Atmospheric Environment, 299, 119638. https://doi.org/10.1016/j.atmosenv.2023.119638.

Sutton, M., Raghuram, N., Adhya, T.K., Baron, J., Cox, C., de Vries, W., Hicks, K., Howard, C., Ju, X., Kanter, D., Masso, C., Ometto, J.P., Ramachandran, R., van Grinsven, H., Winiwarter, W., (2019). Nitrogen and its environmental impact. In: Frontiers 2018/2019: Emerging Issues of Environmental Concern (UNEP). https://wedocs.unep.org/handle/20.500.11822/27543.

Takemura, T., Egashira, M., Matsuzawa, K., Ichijo, H., O'ishi, R., Abe-Ouchi, A., (2009). A simulation of the global distribution and radiative forcing of soil dust aerosols at the Last Glacial Maximum. Atmospheric Chemistry and Physics, 9, 3061–3073. https://doi.org/10.5194/acp-9-3061-2009.

Takemura, T., Nakajima, T., Dubovik, O., Holben, B.N., Kinne, S., (2002). Single-scattering albedo and radiative forcing of various aerosol species with a global three-dimensional model. Journal of Climate, 15, 333–352.

Takemura, T., Nozawa, T., Emori, S., Nakajima, T.Y., Nakajima, T., (2005). Simulation of climate response to aerosol direct and indirect effects with aerosol transport-radiation model. Journal of Geophysical Research, 110, D02202. https://doi.org/10.1029/2004JD005029.

Takemura, T., Okamoto, H., Maruyama, Y., Numaguti, A., Higurashi, A., Nakajima, T., (2000). Global three-dimensional simulation of aerosol optical thickness distribution of various origins. Journal of Geophysical Research, 105, 17853–17873.

Trenberth, K.E., (2008). The impact of climate change and variability on heavy precipitation, floods, and droughts. Encyclopedia of Hydrological Sciences. https://doi.org/10.1002/0470848944.hsa211.

Vennemo, H., Aunan, K., Lindhjem, H., Seip, H., (2009). Environmental pollution in China: Status and trends. Review of Environmental Economics and Policy, 3, 209–230. https://doi.org/10.1093/reep/rep009.

Wang, J., Christopher, S.A., (2003). Intercomparison between satellite-derived aerosol optical thickness and $PM_{2.5}$ mass: Implications for air quality studies. Geophysical

Research Letters, 30, 2095. https://doi.org/10.1029/2003GL018174.

Williamson, C.J., Kupc, A., Axisa, D., Bilsback, K.R., Bui, T., Campuzano-Jost, P., Dollner, M., Froyd, K.D., Hodshire, A.L., Jimenez, J.L., Kodros, J.K., Luo, G., Murphy, D.M., Nault, B.A., Ray, E.A., Weinzierl, B., Wilson, J.C., Yu, F., Yu, P., Pierce, J.R., Brock, C.A., (2019). A large source of cloud condensation nuclei from new particle formation in the tropics. Nature, 574(7778), 399–403. https://doi.org/10.1038/s41586-019-1638-9.

Woodcock, N., Schneider, S.H., Boston, P.J., (1992). Scientists on Gaia. Cambridge (Mass.), London: Massachusetts Institute of Technology Press. ISBN: 0 262 19310 8. Geological Magazine, 130(6), 858–858. https://doi.org/10.1017/S0016756800023268.

Wu, J., Guo, J., Zhao, D., (2013). Characteristics of aerosol transport and distribution in East Asia. Atmospheric Research, 132–133, 185–198. https://doi.org/10.1016/j.atmosres.2013.05.018.

Wu, T., Zhang, F., Zhang, J., Jie, W., Zhang, Y., Wu, F., Li, L., Yan, J., Liu, X., Lu, X., Tan, H., Zhang, L., Wang, J., Hu, A., (2020). Beijing Climate Center Earth System Model version 1 (BCC-ESM1): Model description and evaluation of aerosol simulations. Geoscientific Model Development, 13, 977–1005. https://doi.org/10.5194/gmd-13-977-2020.

Wu, Y., Zhang, S., Hao, J., Liu, H., Wu, X., Hu, J., Walsh, M.P., Wallington, T.J., Zhang, K.M., Stevanovic, S., (2017). On-road vehicle emissions and their control in China: A review and outlook. Science of the Total Environment, 574, 332–349. https://doi.org/10.1016/j.scitotenv.2016.09.040.

Xia, X., Zhang, T., Wang, L., Gong, W., Zhu, Z., Wang, W., Gu, Y., Lin, Y., Zhou, X., Dong, J., Fan, S., Xu, W., (2023). Spatial–temporal fusion of 10-min aerosol optical depth products with the GEO–LEO satellite joint observations. Remote Sensing, 15(8), 2038. https://doi.org/10.3390/rs15082038.

Xu, F., Huang, Q., Yue, H., Feng, X., Xu, H., He, C., Yin, P., Bryan, B.A., (2023). The challenge of population aging for mitigating deaths from $PM_{2.5}$ air pollution in China. Nature Communications, 14, 5222. https://doi.org/10.1038/s41467-023-40908-4.

Yamashita, K., Honda, Y., (2017). Climate change and air pollution in East Asia: Taking transboundary air pollution into account. In: Springer Climate, pp. 309–326. https://doi.org/10.1007/978-3-319-61346-8_19.

Yang, X., Zhao, C., Yang, Y., Fan, H., (2021). Long-term multi-source data analysis about the characteristics of aerosol optical properties and types over Australia. Atmospheric Chemistry and Physics, 21, 3803–3825. https://doi.org/10.5194/acp-21-3803-2021.

Yim, S.H.L., Gu, Y., Shapiro, M.A., Stephens, B., (2019). Air quality and acid deposition impacts of local emissions and transboundary air pollution in Japan and South Korea. Atmospheric Chemistry and Physics, 19, 13309–13323. https://doi.org/10.5194/acp-19-13309-2019.

Yoshino, A., Takami, A., Hara, K., Nishita-Hara, C., Hayashi, M., Kaneyasu, N., (2021). Contribution of local and transboundary air pollution to the urban air quality of Fukuoka, Japan. Atmosphere, 12(4), 431. https://doi.org/10.3390/atmos12040431.

Yu, F., Ma, X., Luo, G., (2013). Anthropogenic contribution to cloud condensation nuclei and the first aerosol indirect climate effect. Environmental Research Letters, 8(2), 024029. https://doi.org/10.1088/1748-9326/8/2/024029.

Zeng, J., Tohjima, Y., Fujinuma, Y., Mukai, H., Katsumoto, M., (2003). A study of trajectory quality using methane measurements from Hateruma Island. Atmospheric Environment, 37(14), 1911–1919. https://doi.org/10.1016/S1352-2310(03)00048-7.

Zeydan, Ö., Yıldırım, Y., (2024). Impact of dust transport events on PM_{10} concentrations on the western coasts of Turkey: A case of April 2022. Air Quality, Atmosphere & Health, 17, 799–811. https://doi.org/10.1007/s11869-023-01481-3.

Zhang, Q., Zheng, Y., Tong, D., Shao, M., Wang, S., Zhang, Y., Xu, X., Wang, J., He, H., Liu, W., Ding, Y., Lei, Y., Li, J., Wang, Z., Zhang, X., Wang, Y., Cheng, J., Liu, Y., Shi, Q., Yan, L., Geng, G., Hong, C., Li, M., Liu, F., Zheng, B., Cao, J., Ding, A., Gao, J., Fu, Q., Huo, J., Liu, B., Liu, Z., Yang, F., He, K., Hao, J., (2019). Drivers of improved $PM_{2.5}$ air quality in China from 2013 to 2017. Proceedings of the National Academy of Sciences, 116(49), 24463–24469. https://doi.org/10.1073/pnas.1907956116.

Zheng, B., Tong, D., Li, M., Liu, F., Hong, C., Geng, G., Li, H., Li, X., Peng, L., Qi, J., Yan, L., Zhang, Y., Zhao, H., Zheng, Y., He, K., Zhang, Q., (2018). Trends in China's anthropogenic emissions since 2010 as the consequence of clean air actions. Atmospheric Chemistry and Physics, 18, 14095–14111. https://doi.org/10.5194/acp-18-14095-2018.

Zheng, C., Wu, Y., Ting, M., Orbe, C., (2024). Influence of atmospheric circulation on

the interannual variability of transport from global and regional emissions into the Arctic. Atmospheric Chemistry and Physics, 24, 6965–6985. https://doi.org/10.5194/acp-24-6965-2024.

Zhong, L., Louie, P.K., Zheng, J., Wai, K., Ho, J.W., Yuan, Z., Lau, A.K., Yue, D., Zhou, Y., (2013). The Pearl River Delta Regional Air Quality Monitoring Network – Regional collaborative efforts on joint air quality management. Aerosol and Air Quality Research, 13, 1582–1597. https://doi.org/10.4209/aaqr.2012.10.0276.

Zhou, Y., Zhang, X., Zhang, C., Chen, B., Gu, B., (2024). Mitigating air pollution benefits multiple sustainable development goals in China. Environmental Pollution, 349, 123992. https://doi.org/10.1016/j.envpol.2024.123992.

Zhu, Y., Huang, C., (2012). An improved median filtering algorithm for image noise reduction. Physics Procedia, 25, 609–616. https://doi.org/10.1016/j.phpro.2012.03.133.

Acknowledgements

I would like to express my deepest gratitude to Professor Irie for his invaluable guidance and support throughout this research. I am also sincerely thankful to the senior members of Irie Laboratory for their mentorship and encouragement, which have been instrumental in my academic growth. My heartfelt appreciation goes to my co-authors, Dr. Damiani, Dr. Itahashi, Professor Takemura, and Associate Professor Khatri, for their constructive feedback and collaborative support, which greatly contributed to the success of this study.

Lastly, I am profoundly grateful to my family and friends for their support and encouragement, which was a source of strength throughout my entire doctoral research career.

Publications, presentations, and award

Publications

Cai, Y., Irie, H., Damiani, A., Itahashi, S., Takemura, T., Khatri, P., (2024). Detectability of the potential climate change effect on transboundary air pollution pathways in the downwind area of China. Science of the Total Environment, 939, 173490. https://doi.org/10.1016/j.scitotenv.2024.173490.

Presentations

International conference:

(1) **Ying Cai**, Hitoshi Irie, Kodai Yamaguchi, Observational study on the response of aerosol optical depth over Japan to springtime transboundary air pollution in 2011-2019, The American Geophysical Union (AGU), Online, Dec 12, 2020 (poster).

(2) **Ying Cai**, Hitoshi Irie, Alessandro Damiani, Syuichi Itahashi, Toshihiko Takemura, Pradeep Khatri, Detectability of the potential climate change effect on transboundary air pollution pathways in the downwind area of China, Asian Conference on Meteorology (ACM),2024, Tsukuba, Nov 18, 2024 (oral).

Domestic conference:

(1) **YING CAI**, Hitoshi Irie, Kodai Yamaguchi, Observational study on the response of aerosol optical depth over Japan to springtime transboundary air pollution in 2011-2019, 日本地球惑星科学連合大会、Online、2020 年 7 月 14 日(oral).

(2) **YING CAI**, Hitoshi Irie, Alessandro Damiani, 東アジアの越境大気汚染エアロゾルに及ぼすモンスーンの影響に関する観測的研究, 日本気象学会、Online、2021 年 12 月 03 日(oral).

(3) 蔡穎、入江仁士、Alessandro Damiani,、板橋秀一、竹村俊彦、東アジアの越境大気汚染エアロゾルに及ぼす気候変動の影響に関する観測的研究、日本地球惑星科学連合、千葉幕張メッセ、2022 年 5 月 25 日(oral).

(4) 蔡穎、入江仁士、Alessandro Damiani,、板橋秀一、竹村俊彦、東アジアの越境大気汚染エアロゾルに及ぼす気候変動の影響に関する観測的研究、日本気象学会 2022 年度秋季大会、北海道札幌市、2022 年 11 月 27 日(oral).

(5) 蔡穎、入江仁士、Alessandro Damiani,、板橋秀一、竹村俊彦、気候変動が東アジアの越境大気汚染エアロゾルの経路に及ぼす影響の検出可能性、日本気象学会 2023 年度秋季大会、仙台市、2023 年 10 月 25 日(oral).

(6) 蔡穎、入江仁士、Alessandro Damiani,、板橋秀一、竹村俊彦、Pradeep Khatri、人為起源エアロゾルを用いた気候変動に伴う大気輸送場変動の検出可能性、第 29 回大気化学討論会（2024）、神戸市、2024 年 10 月 9 日(oral).

(7) 蔡穎、入江仁士、Alessandro Damiani,、板橋秀一、竹村俊彦、Pradeep Khatri、気候変動が中国からの越境大気汚染経路に及ぼす潜在的な影響の検出可能性、日本気象学会（2024）、つくば、2024 年 11 月 13 日(oral).

Award

学生優秀発表賞、人為起源エアロゾルを用いた気候変動に伴う大気輸送場変動の検出可能性、日本大気化学会 第 29 回大気化学討論会、神戸大学統合研究拠点コンベンションホール（神戸市）、2024 年 10 月